Cyclic Behavior of a Hybrid Light Gauge and HSS Mezzanine Structural System

Michael John Kren
Marquette University

CYCLIC BEHAVIOR OF A HYBRID LIGHT-GAUGE AND HSS MEZZANINE STRUCTURAL SYSTEM

By

Michael J. Kren, B.S.

A Thesis submitted to the Faculty of the Graduate School,
Marquette University,
in Partial Fulfillment of the Requirements for
the Degree of Masters of Science

Milwaukee, Wisconsin

May 2016

ABSTRACT
CYCLIC BEHAVIOR OF A HYBRID LIGHT-GAUGE
AND HSS MEZZANINE STRUCTURAL SYSTEM

Michael Kren, B.S.

Marquette University, 2016

Cold-formed steel is emerging as an alternative material in the building industry to hot-rolled steel for smaller buildings and indoor structures also called mezzanines. Cyclic testing of a full-scale mezzanine structures composed of cold-formed structural channel beams connected to hollow structural steel (HSS) columns cap plates using wedge expansion anchors at the base plate to generate rotation restraint, is performed in this research. The characteristics of the structure will be explained by displaying full experimental results of structural testing.

Unfortunately, limited experimental data outlining the behavior of these structures is available and design criteria is very limited. Thus, there is a need to conduct reliable experimental tests to understand fundamental behavioral mechanisms for migration into effective design criteria.

A full analysis to produce moment-rotation curves at the column base plate will be used to study their structural behavior. Loads are imposed using cyclic lateral displacements in accordance with AISC protocols. HSS base plate connection behavior is not fully understood and makes use of fixed base HSS columns in seismic regions difficult to quantify. Hysteretic models of the entire structure will be presented for further research of nonlinear response of frame structures.

ACKNOWLEDGEMENTS

Michael J. Kren, B.S.

This thesis is one of the most difficult tasks I have ever completed. It gives a large display of my knowledge and hard work. Along the way I have received immense support from a great deal of people including family and friends who I would like to recognize.

First of all I would like to thank my thesis advisor, Dr. Christopher Foley. You are instrumental in giving me the support. It is my privilege to call you my mentor and friend. I thank you for giving me this opportunity to grow.

I would also like to thank Dr. Baolin Wan and Dr. Stephan Heinrich for reading this thesis and for providing valuable input during its undertaking. I want to give a special thanks to Mr. David Newman, Mr. Joseph Packhem, and Mr. Joseph Tschida for the immense help setting up the testing phase of the experiment and for your help and support throughout my time at Marquette University. Thanks to Mr. Christopher Baumann and Mr. Sean Dailey for casting the concrete footings required for test setups. Thank you to Mr. Austin Anderson for the assistance with learning programming in MATLAB throughout my college career.

I also want to thank my parents Barbara and Leslie Kren, for the incredible support I have received throughout this process as well as during my entire life. I could never have gotten to where I am today without your care and support. Your lives have been the inspiration which I use to conduct my own. I could never repay you for everything you have given me.

To my sister, Amy Kren, thank you so much for setting a wonderful example completing your college degrees. I am so proud to call you my family and my friend. Thank you for being there for me.

Thank you to Cubic Designs, Incorporated of New Berlin, WI for the donation of the mezzanine structure to Marquette University Engineering Materials and Structures Testing Laboratory that served as a basis for experimental testing in this thesis.

TABLE OF CONTENTS

LIST OF TABLES

LIST OF FIGURES

CHAPTER 1 - INTRODUCTION AND LITERATURE REVIEW

1.1 Introduction

A general classification of steel connections includes two groups: simple-shear connections and moment-resisting connections used in moment frames. Engineering requirements determine the type required. Simple-shear connections are designed to resist only gravity loads. They have low rotational stiffness and allow for only transverse shear to be resisted in the connection. Moment-resisting connections generate rotational restraint at the beam ends and support both bending moment, shear, and axial forces. Moment-resisting connections are widely used to dissipate energy from earthquakes and to resist lateral wind loads in structural engineering systems.

The rigidity (stiffness) of a moment connection makes it possible to utilize member flexural stiffness for resistance to lateral loads. The AISC Seismic Design Manual, the current standard in the United States, specifies the required design for structural steel buildings in seismic zones. Buildings in seismic zones typically incorporate wide flange beams with moment-resisting connections such as an extended end plate or bolted flange plate (BFP) moment-resisting connection, incorporating reduced beam sections allowing for the creation of a plastic hinge removing large forces from the column face.

The use of hollow structural sections (HSS) moment-resisting connection in seismic zones is increasing, especially with emerging research displaying the cyclic behavior of HSS in moment-resisting frames.

There are generally two types of steel structural materials: hot rolled and cold-formed (Beshara and Schuster 2000). Hot rolled steel is most common for structural applications. With the development of heavier gauge manufacturing processes and a favorable strength-to-weight ratio, cold-formed steel structural elements are emerging as an alternative to hot rolled steel for many applications (Beshara and Schuster 2000).

Since most steel building systems traditionally incorporate mild steel components, structures incorporating cold formed steel are less familiar to structural designers (Beshara and Schuster 2000). Although cold-formed steel has advantages over typical mild steel, local and distortional buckling phenomena can lead to design procedures that are slightly more difficult than those used for hot rolled steel sections.

In addition, moment-resisting base plates need more research to improve design practice. Column bases transfer reactions from the structure to the foundation and can be exposed to a variety of forces including axial, shear, and bending moments with deformations occurring due to rotations (Vandegans and Jaspart 1998).

This report details the testing of a mezzanine structural system composed of cold-formed steel shapes and hollow structural shapes (HSS), shown in Figure 1.1. Structures such as this are common in the seismic zones. Cold-form steel channels and HSS shapes are commonly used as beams and columns. The HSS tubes used in this structure are composed of the American Society for Testing and Materials (ASTM) A500 Grade B steel. Figure 1.1, shows the overall layout of the mezzanine structure including the naming of the connection, the columns, and the channels as well as the spreader beam used for loading and the typical metal deck used to clad the structure.

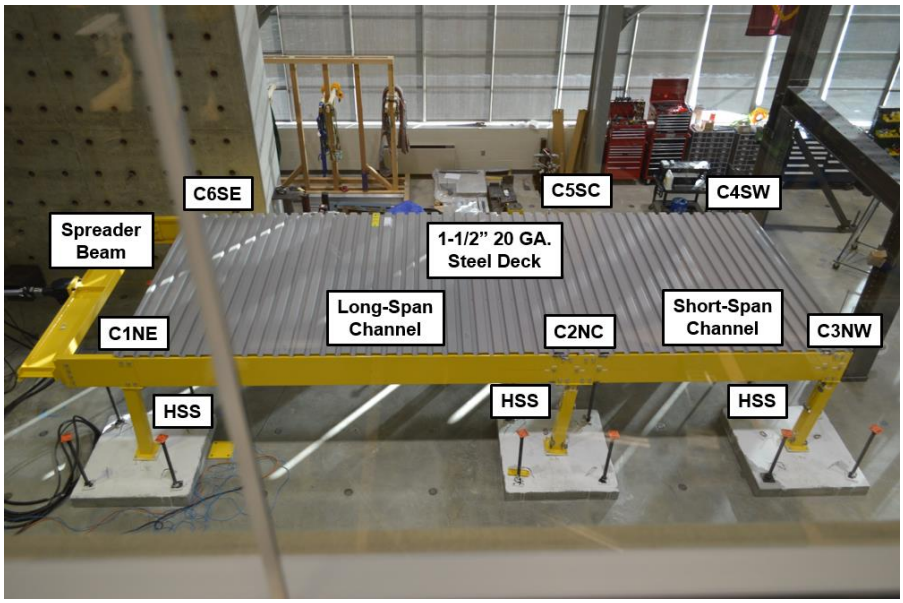

FIGURE 1.1: OVERVIEW OF MEZZANINE STRUCTURE

The moment-resisting connection in this structure are cold-formed steel channels connected to HSS tubes using single-sided bolted moment connections incorporating connecting plates as shown in Figure 1.2, which behaves differently than traditional moment-resisting connections. Structural bolts act in single shear and plates are connect to the vertical web of a cold-formed steel channel without restraint of the beam flanges. Mild steel base plates (Figure 1.3) are welded to the HSS to create moment-resisting connection to the structure's foundation using wedge type expansion bolts.

The main objective of this research is to quantify the behavior of the mezzanine structural system by presenting data from experimental testing. Strain, displacements, and load measurements that can be used to understand how a hybrid structural system reacts to imposed cyclic lateral displacements.

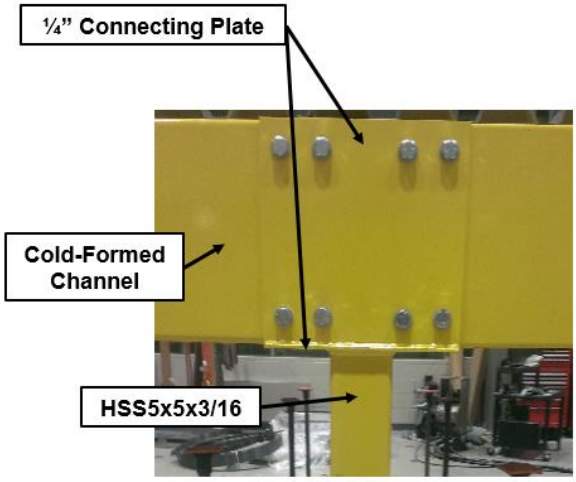

FIGURE 1.2: BEAM TO COLUMN CONNECTION (POST-TEST)

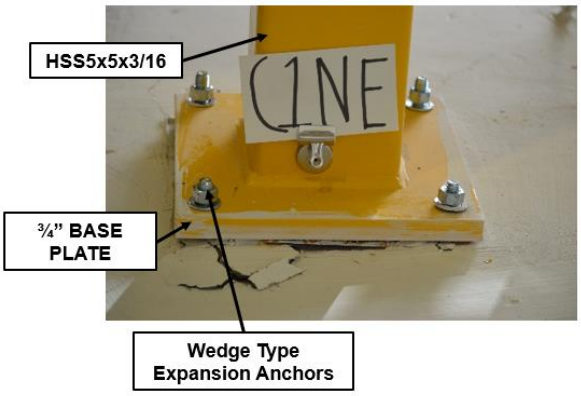

FIGURE 1.3: COLUMN TO BASE CONNECTION (POST-TEST)

1.2 Literature Review

The research incorporated into this thesis covers a broad range of topics currently studied in the structural engineering community. Typically, research is performed on a component basis rather than testing of a complete structure at full-scale as it is done here. A wide range of literature review will be presented to cover the topics addressed in the results and analysis.

The mezzanine structure tested in this thesis incorporates cold-formed steel channel beams, HSS tubes, expansion anchors exposed to repeated tension and shear loading, and base plates with flexural forces. All of these are commonly used by design engineers yet many lack available experimental results to understand behavior.

1.2.1 Experimental and Theoretical Testing of Cold-Formed Steel Moment Connections

Cold-formed steel is commonly used in structural building systems for components and cladding. Its use in a structure as the main lateral force resisting system is less common. With the new specifications including the AISI seismic design standard (AISI 2007) which includes specifications for cold-formed steel in use for moment-resisting frames, use of cold-form as the main lateral force-resisting system will become more common.

The seismic design philosophy of steel structures is based on the strong column weak beam concept developed by AISC. This concept involves making the columns stronger in flexural than the beams causing deformations from seismic forces to occur mainly in the beams. Use of the strong column-weak beam concept with compact sections facilitates seismic energy dissipation with a lower probability of collapse. Cold-Formed Steel Special Bolted Moment Frames (CFS-SBMF), however, cannot satisfy these criteria due to the difficulty in satisfying compact section requirements (Uang, et al. 2010). CFS-SBMF usually dissipate energy by, "…the basis that ductility capacity is provided through bolt slippage and bearing in bolted beam-to-column moment connections, and that beams and columns remaining elastic at the design story drift to resist the maximum force developed in the connections" (Uang and Sato 2009).

Typical early research performed on cold-formed steel moment-resisting connection used static unidirectional load testing rather than cyclic load tests. The loading protocol for seismic design of moment-resisting connections today simulates demand using a far-field earthquake (AISC 2010). The first research articles will be composed of mainly tests involving unidirectional static load. Later articles will involve the response of cold-form sections and moment connections to cyclic lateral displacement.

(Chung and Lau 1998)

This study included a wide variety of experimental tests on cold-formed steel moment-resisting connections. Figure 1.4 gives an example of a moment-resisting connection composed of back-to-back channels connected with bolts through the webs to plates, tested with an applied unidirectional static load to failure. The experimental results are used to define the capacity of the connection in relation to the strength of the connected member. Failure modes and mechanisms along with the moment capacity in the connected section was established in this article based on experimental results.

The failure modes seen in the test of cold-formed moment-resisting connections included the bearing failures in the section around the bolt holes at 50 percent of the plastic moment capacity, flexural failure of connected beams at 60 to 75 percent of the plastic moment capacity due to buckling and yielding, and columns at 80 percent of the plastic moment capacity due to buckling and yielding.

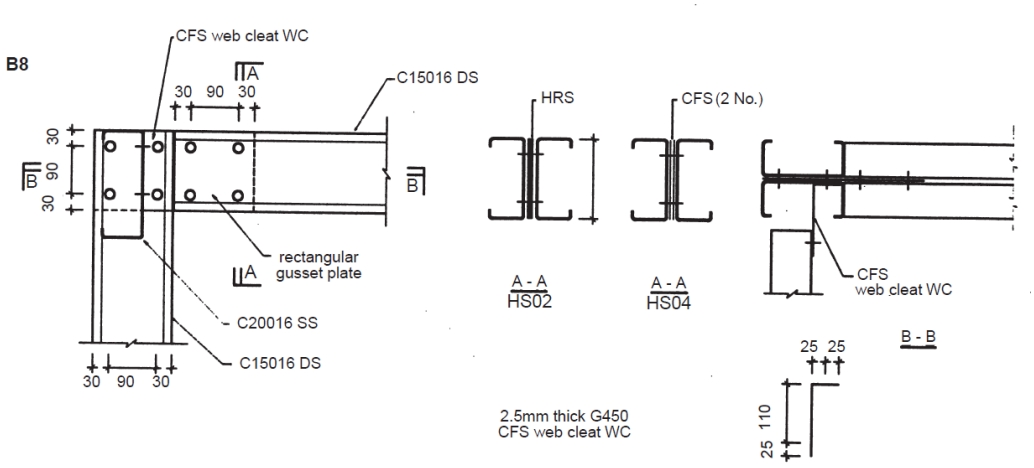

FIGURE 1.4: COLD-FORMED STEEL MOMENT CONNECTIONS (CHUNG AND LAU 1998)

(Uang, et al. 2010)

The results of experimental tests performed on nine full-scale beam-column connections of CFS-SBMF composed of two channel beams bolted directly to the square HSS member with bearing-type connection using high-strength bolts shown in Figure 1.5 is given in (Uang, et al. 2010). Typical connections in this study are commonly used in mezzanines and small buildings today.

The test results of (Uang, et al. 2010) showed that specimens had interstory drift capacity that significantly exceeded 0.04 radians required by (AISC 2010) with energy dissipation occurring due to bolt slip and bolt bearing from the absence of plastic hinges to dissipate energy. The results indicated that beam and column deformations provided little support to reaching high levels of interstory structural drift. It was recommended that local buckling of columns and beams be avoided due to the potential for strength degradation of the members.

Further research from (Uang and Sato 2008) utilizes the data of (Uang, et al. 2010) to create design provisions that can be used for CFS-SBMF. Bolting channel

beams directly to an HSS to provide moment-resistance involves design provisions that include calculating the maximum seismic force in beams and columns at design story drift based on instantaneous center of rotation of the bolt group (Uang and Sato 2008). This gives methods to determine the level of slip that will occur based on the column shear and bolt spacing, simplifying seismic design of the structure.

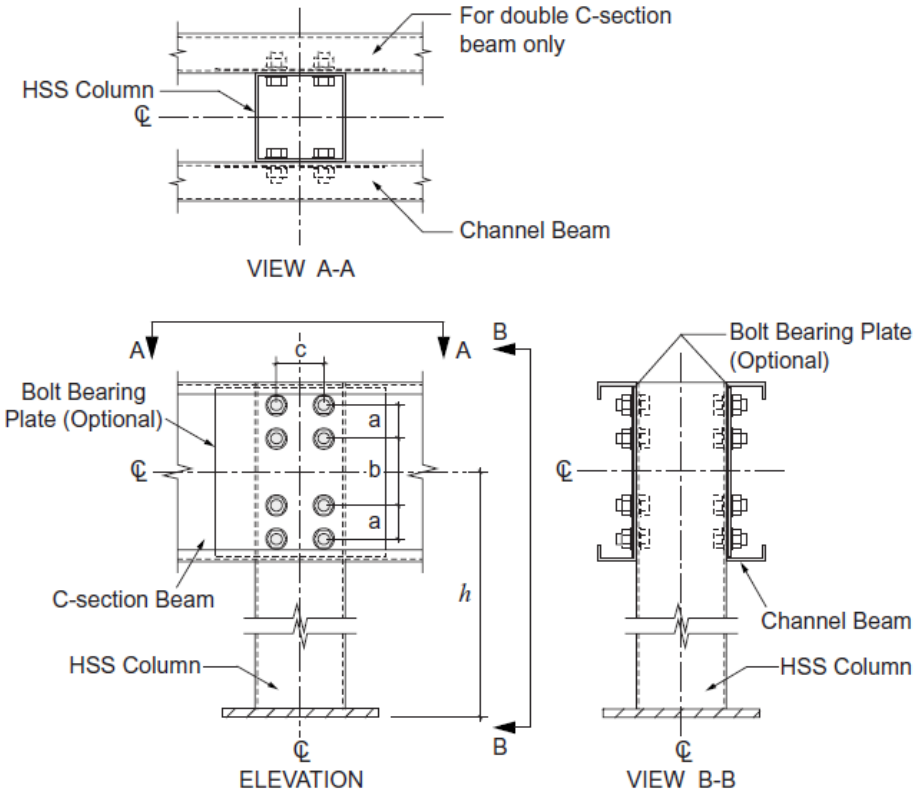

FIGURE 1.5: CONNECTION OF HSS COLUMNS AND DOUBLE CHANNEL BEAMS (UANG ET. AL, 2010)

The work of (Uang and Sato 2010) utilizes the experimental connection data of (Uang, et al. 2010) to verify seismic design standards of AISI 2007 to evaluate the use of values such as the deflection amplification factor, response modification coefficient, and system overstrength factor used by design engineers.

Nonlinear analysis is performed using the connection models of (Uang, et al. 2010). The result was design of cold-formed steel structural systems in which the designer is able to directly calculate the maximum seismic force in the moment connection at a design story drift level, eliminating the empirical overstrength factor for design of moment frames.

(Rasmussen and Gilbert 2010)

This research details the analysis of moment connections in drive-in and drive-through steel storage racks which rely on a moment connection and the stiffness of a base plate to resist lateral loading with extremely loose connections allowing excessive rotations. An example of this connection is given in Figure 1.6 showing the use of bolts to restrain portal beams resulting in a connection with relatively high levels of initial flexibility.

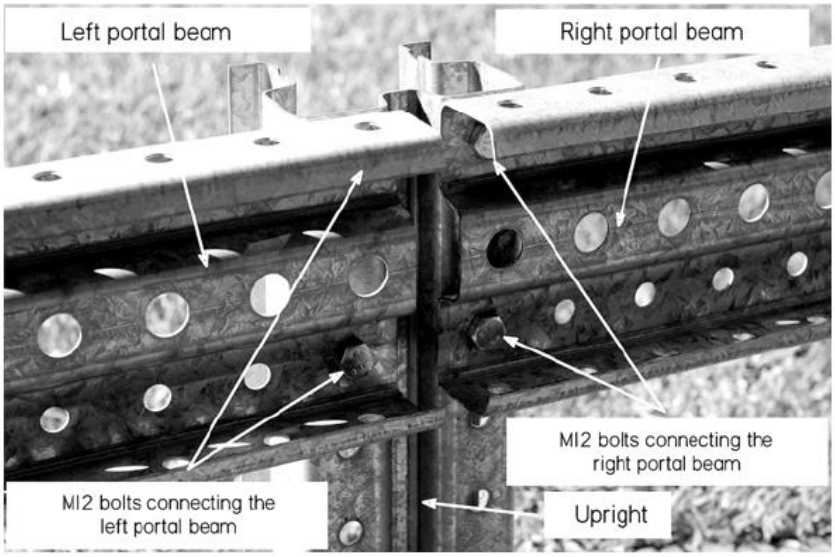

FIGURE 1.6: DRIVE-IN AND DRIVE-THROUGH STEEL STORAGE RACKS (RASMUSSEN AND GILBERT 2010)

A portal frame rather than a component of the connection typical of the structure in question was tested with cyclic displacement demand to determine the moment-

rotation behavior of typical connections used for this application. Due to the slenderness of the members used for this study an investigation of the P-Δ effect was undertaken.

The experimental hysteretic behavior of the structure allowed for a multi-linear moment-rotation behavior backbone curve of the portal frame to be determined using three separate structural stiffness from experimental moment-rotation curves. The behavior accounting for initial structural flexibility and bearing in the bolt holes developing similar behavior to the results of (Uang, et al, 2010).

1.2.2 Experimental Testing of Expansion Anchors

The mezzanine structure considered in this thesis uses wedge type expansion anchors. Wedge type expansion anchors develop tensile resistance from frictional forces in concrete and allow for installation after completion of concrete work due and to their ability to be post installed without a precise installation location. Moment-rotation curves created near the structure base plates display a significant amount of relevant data for the performance of expansion anchors to seismic activity.

(Ghobarah and Aziz 2004)

This paper details experimental testing of wedge type expansion anchors from a variety of manufacturers for their ability to withstand cyclic loading according to ASTM E488 (ASTM 2015) and Canadian CSA N287.2 (CSA 2008), using the test setup in Figure 1.7. To use expansion anchors in seismic zones, anchors must have sufficient strength to develop ductility. Since expansion anchors develop tensile capacity through concrete friction, anchors must maintaining their load carrying capacity beyond the design basis earthquake when the proper install torque is used. Tests in this paper are performed for

failures of the anchor statically and dynamically in both tension and shear. Interestingly, this research found that some wedge type expansion anchors actually provide more resistance to dynamic forces than static forces because dynamic forces can help set the anchors expansion mechanism to increase friction with the surrounding concrete cone. The performance of the expansion anchors proved that their use for seismic applications yields load carrying capacities sufficient of equivalent static loads further increasing their ability for use.

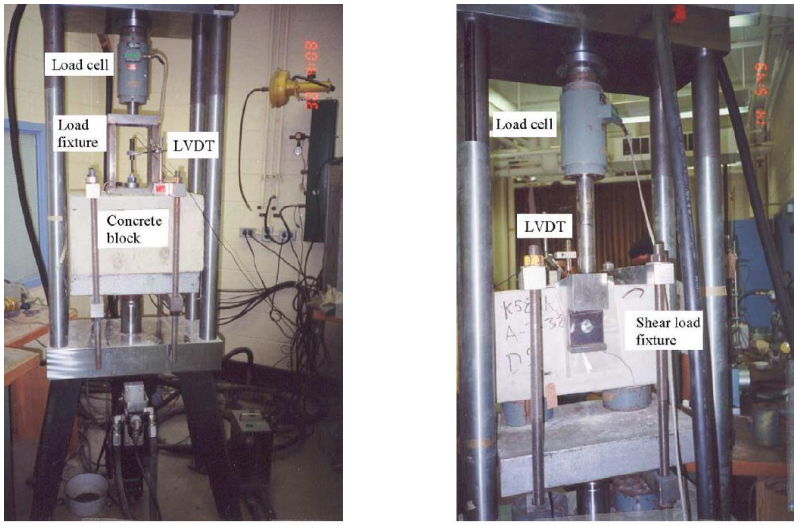

FIGURE 1.7: CYCLIC TENSION AND SHEAR TESTING OF WEDGE TYPE EXPANSION ANCHORS (GHOBARAH AND AZIZ 2004)

(Štrba and Karmazínová 2012)

Similar, more recent, research detail cyclic loading applied to wedge type expansion anchors presenting results for both steel-bolt failures and concrete-cone failures. The main focus of this paper was expansion anchors under repeated (cyclic) tensile loading. It also compared the results of static and cyclic loading allowing for a better understanding of expansion anchor behavior. Similar results to (Ghobarah and Aziz 2004) were found.

1.2.3 Experimental and Theoretical Behavior of HSS Members

HSS are useful to practicing structural engineers due to their high strength-to-weight ratio and their efficient compression, torsion, and bending behaviors. They are used in a variety of seismic and non-seismic applications, including braces, columns, concrete-filled columns, truss members, and flexural members. Additionally, revisions to the AISC specifications (AISC 2005, AISC 2010) made HSS design in the United States more accessible. HSS are available in many sizes, allowing for varied applications and can be easily filled with concrete for increased efficiency as a column. Research concerning HSS includes the areas of fatigue, seismic applications, and connections.

Most of the earlier research concerning HSS is in braced frames rather than moment-resisting frames. A prime example of cyclic loading of an HSS braces frame is (Tremblay, et al. 2002).

(Wilkinson and Hancock 1998)

This article presents some of the earlier results of the bending behavior of HSS. Experimental results of a number of tests concludes that HSS cannot produce rotational capacity for plastic design, because the shape cannot resist buckling in the web and/or yielding in the flange. This article also concludes that the material strength of an HSS does not influence its ability to perform under cyclic loading.

(Guerrero, et al. 2007)

This paper outlines experimental testing and finite element modeling of HSS subject to cyclic and monotonic loading. They conclude that width-thickness and depth-thickness ratios were determined to affect the degradation of load capacity in HSS members.

(Fadden and McCormick 2013)

HSS in seismic moment-resisting applications has been limited due to the unknowns associated with their behavior leading to wide flange shapes as the predominant structural shape in use for moment-resisting frame systems.

Along with unknowns associated with HSS section behavior, material control of HSS is much lower due to the current standard being ASTM A500 Steel which specifies a minimum yield stress of 46 kip per square inch (ksi) but no maximum strength (ASTM 2013).

Material tests were performed on a variety of different HSS sections but also from a variety of different areas on the tubes including flats and corners of the tubes allowing for a better understanding of how the cold-working process used to create HSS affects the material strengths. Typically, the study found that the coupons taken from the flats had lower yield and ultimate strengths than the corner or seam weld specimens. The results displayed yield stresses far in excess of the ASTM A500 limit and ultimate strengths far in excess of a ratio suitable for efficient seismic implementation.

A parametric study of finite element models of many HSS shapes allowed for the calculation of the moment degradation at 0.04 radians and the rotational capacity at 80 percent of the moment capacity. Previous experimental results of (Fadden 2013) were compared to the parametric finite element studies to help validate the results. Both the finite element model and the experimental results support the ability of the HSS to sustain 80 percent of its plastic moment capacity at an interstory drift of 0.04 radians as required by AISC seismic specification (AISC 2010).

The paper also concluded that increasing width-thickness and depth-thickness ratios decreased the moment capacity while increasing the amount of rotation the section is able to sustain. Due to the levels of tested material strength used in the finite element models, most of the sections exceeded the nominal plastic moment capacity of the section.

(Fadden and McCormick 2012)

This paper outlined experiments results conducted to quantify the behavior of HSS in an effort to develop moment-rotation behavior of HSS shapes based on cyclic displacement loading, using the test setup in Figure 1.8.

The main conclusion of this article is its quantification of rotational capacity at different levels of the plastic moment capacity with respect to width-thickness and depth-thickness ratios and the ability of all HSS to produce stable hysteretic behavior. This in turn led to the conclusion that HSS are capable of use in cyclic bending applications provided the width-thickness and depth-thickness ratios are at levels able to limit local buckling at small rotation levels.

(Fadden 2013)

The most important result of this research effort being, HSS moment-resisting connection design parameters, was not contained in the two previously mentioned articles of (Fadden and McCormick 2012) and (Fadden and McCormick 2013). These design parameters are base off finite element models of HSS connections, tested using cyclic loading protocols of the AISC seismic specification.

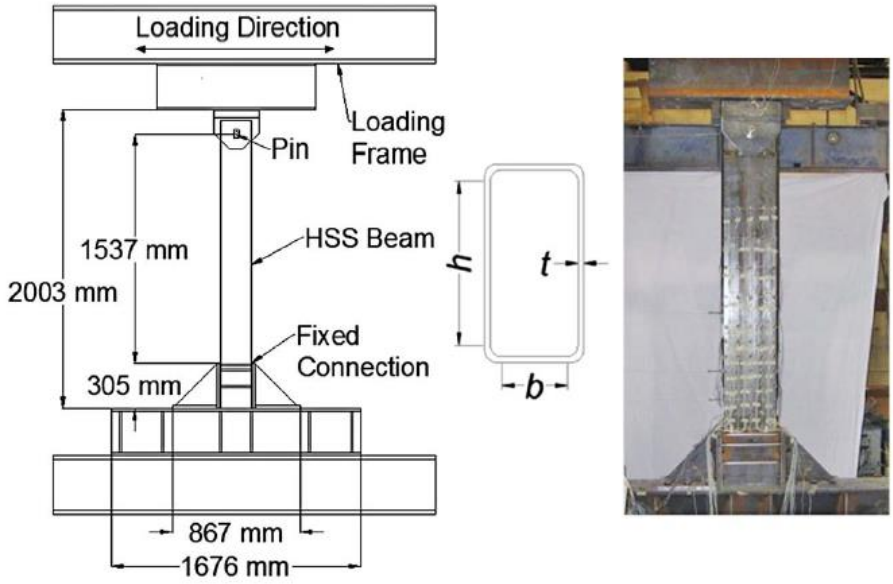

FIGURE 1.8: HSS TEST SETUP (FADDEN AND MCCORMICK 2012)

HSS members have some characteristics that are better in moment-resisting frames due to the ability to reduce the seismic mass of the structure. Unreinforced HSS moment-resisting connections are useful due to the reduced cost from not having to add stiffener plates. Reinforced HSS-to-HSS moment-resisting connections have applications in seismic moment frames. The main issue is that most of the inelastic behavior occurs at the column face. It is also determined that energy dissipation through hysteric behavior for these connection increased as the beam member depth increased.

1.2.4 Extended End Plate and Base Plate Connections

Column base plates are a complicated component which is often overly simplified in the design world of structural engineering. Column base connections transfer gravity, wind, and seismic loads from a structure into the foundation. Moment-resisting base plates often include a variety of force on the structure's base including bending, shear, and axial

which can have a variety of effects especially when oversized holes are used making contact with only a few of the anchor rods rather than all the anchor rods once friction forces are overcome. The extended end-plate moment-resisting connection has many similarities with moment-resisting base plates but moment-resisting base plates must also take crushing of concrete and usually large axial loads into account. General design practices for base plates and anchor rods used in the United States were formulated based on strength parameters with little emphasis on flexibility.

(Murray and Meng 1995)

The 1994 Northridge earthquake caused a change in thought about steel buildings. Different types of connections and different ways of performing structural analysis were created to allow for buildings that were safer for occupants and more resistant to damage. This article was written shortly after the Northridge earthquake and shows some of the early research about the effects of large seismic events.

A substantial portion of damage to steel structures following the Northridge Earthquake was due to fractured on-site welded moment connections. An alternative design proposed in this article is the extended end plate which eliminates beam flange-to-column welds and is able to dissipate energy due without a significant loss of strength. The results presented on extended end-plate moment connections in this article supported their current use in buildings in both seismic and non-seismic zones.

Preliminary methods for calculating extended end plate strength and cyclic behavior were created paving the way for future research to make improvements of both base plates and extended end plates.

(Wheeler, Clarke and Hancock 2000)

This article presents a large amount of data obtained from finite-element models created using ABAQUS software with 3D brick elements to determine modes of failure associated with the HSS extended end plate connections subjected to monotonic loading. The use of several different sections, shapes, bolt positions, and end-plate thicknesses are varied to gain a different understanding of the factors that affect HSS end-plate connections. The results indicate how the increase in end plate thickness and the distance from the bolts to the edge of the tubular member vary with resistance to applied load helping to increase current connection design models.

(Demonceau, Jaspart and Van-Long 2013)

Research performed in this article involves a presentation of experimental research involving the use of bolted flange joints subjected to tension loads. The research in this article however, included the use of cyclic loading of HSS connections allowing for a more comprehensive evaluation of the connection.

An instrumented connection was tested using comparison of both monotonic loading and cyclic loading. Interestingly however, some of the results indicate similarities between monotonic and cyclic loading.

Failure methods included cracking of the welds between the tube and the end plate, failure of the bolts making up the connection, and failure of the end plate.

(Kanvinde, Grilli and Zareian 2012)

Rotational behaviors of structural base plates is seldom accounted for in design. Interstory structural drift is typically calculated under the assumption of a fixed base. There are many methods available to model rotational strength and stiffness in structural

base plates. Most however are cumbersome and difficult to implement for the design of a typical building.

This article makes an effort to quantify the stiffness of a base plate using both experimental results and analytical models. One of the most difficult issues associated with base plates is flexibility. Not only can the grout, anchor rods, etc. deform, the base plate itself can bend causing an increase in flexibility. The outlined approach characterizes base flexibility in current design practice using the parameters commonly seen in AISC but including limit states of anchor rods, base plate bending, and deformations of concrete, allowing for the secant stiffness of the first yield moment to be determined. The development of analytical procedure in this paper are concluded based on a wealth of prior research from the authors.

(Cooke, Jordan and Kanvinde 2013)

Finite element models of base plates also allow for a way to determine how base connection can be used to resist bending. This research created finite element models in ABAQUS using 3D brick elements. The finite element models created in this study address some of the key concerns associated with base plates not associated with other parts of the steel structure including contact/gap. Rotation in the finite element models of the structural base plates was also quantified in this paper, confirming the results of (Kanvinde, Grilli and Zareian 2012).

A main focus of this article was to evaluate the accuracy of assuming a rectangular stress block of constant magnitude for bearing typical for AISC design criteria. The finite element study performed found that stress profiles rarely represent the rectangular stress block assumption with the thickness of the base plate typically

controlling the shape and size of the stress block. Findings also confirmed limitations for quantifying the requirements associated with anchor rods typically used in design. *(Wald, Jaspart and Sokol 2008)*

This paper focuses on the behavior of the anchor rod groups in the base plate and the strength of the plate itself. It focuses on tension and compression of cast-in-place anchor rods. The main focus is to define the stiffness and resistance of column bases loaded by axial force and bending moment. The stiffness of the base plate was found to be affected by several factors including the width of column flange. Stiffness was calculated in the models by assuming compression of a T-stub rather than a full wide flange section. The resulting stiffness presented as a function of the base plate thickness and distance from column flange allows for determination of base plate rotational deformation with applied loading.

1.2.5 Hysteretic Modeling of Frame Structures

Design engineers typically use a design response spectrum to estimate force and deformation demands of earthquakes. Inelastic design response spectra are created by reducing the elastic design spectra by a strength reduction factor or “R-value”. The accuracy of this method however, is in question. A possible alternative method is using hysteretic models. Hysteretic models of structures can be used to estimate the response of the structure during ground motion. Recorded or simulated ground motions can be defined and analysis can be undertaken using a program such as OpenSees (PEER and NSF) to predict the expected behavior of a structure.

(Oh, Han and Lee 2000)

This article argues that the strength reduction factor value used in structural engineering is dependent not only on the ground motions characteristic of the seismic zone but also the nonlinear characteristics of the structural system. Results showed that inelastic design spectra can differ significantly from the traditionally accepted method of determining loading on a building structure using a reduction of the linear-elastic design with increases in ductility. The authors argue that direct scaling of the elastic design spectra by using a single strength reduction factor results in significant error. The findings suggest the seismic response of a structure is strongly dependent on the hysteretic behavior, structural natural period and target ductility capacity.

(Medina and Krawinkler 2004)

This paper aims to determine the influence of hysteretic behavior on the nonlinear response of a regular frame structure over a wide range of stories and periods. The models used ignore the cyclic deterioration but include P-delta affects and are aimed at performance level damage.

The goal of the analysis is to evaluate the engineering demand parameters, mainly the roof and story drift percentages. This is evaluated using both the R-factor method and by incremental dynamic analysis.

The results indicate that, with the exception of structures very sensitive to P-delta effects, the bilinear and peak-oriented models exhibit similar peak roof and story drift demands regardless of inelastic behavior. When significant degradation of stiffness is present, hysteretic behavior incorporating pinching models drift can far exceed that of peak-orient models currently used by design engineers with increases in error for multi-degree of freedom systems signifying needed reform to seismic design specifications.

1.3 Synthesis of Literature Review

Typical testing of moment-resisting connections in the research field of structural engineering is performed on components, i.e. a single moment connection or moment-resisting base plate connection. Often moment-resisting connections will be tested as a portal frame containing moment-resisting connections (Rasmussen and Gilbert 2010). However, the structures usually contain pin/hinge base connections to effectively make them component tests.

The research performed for this thesis incorporates testing of a complete structure containing multiple components, including HSS column shapes, wedge-type expansion anchors, cold-formed connecting plates, and cold-formed channels, which would usually be tested separately as components making this research different. All of the literature reviewed in this paper contains component tests rather than a test of the complete structure. This makes comparison of results extremely difficult but uncovers a variety of issues. Forces are often enlarged or reduced depending on the way interaction between components occurs, often affecting interstory structural drift and moment-rotation behavior. The testing of the complete structure in this thesis allows determination of the contribution of different structural components to show overall structural response (e.g. interstory drift).

The use of cold-formed steel components in moment-resisting connections for resistance of lateral loads is less extensive than typical mild-steel sections. The monotonic behavior of cold-formed steel shape connections was performed with early research from (Chung and Lau 1998). Cyclic testing of cold-formed steel connections

(Uang, et al. 2010) and (Rasmussen and Gilbert 2010) illustrate connections that utilize cold-formed shapes with adequate ability to dissipate the energy of seismic forces.

Studies of HSS shapes used as columns or brace members have been completed (Tremblay, Archambault and Filiatrault 2002). However, HSS shapes in moment-resisting frames subject to bending forces have not been studied extensively. The ability of HSS to develop cyclic bending capacity needed for beam and beam-column applications has been demonstrated by (Wilkinson and Hancock 1998). The most extensive research of bending for HSS members was contained in (Fadden 2013). Incorporating HSS in the testing of this structure will allow for increased experimental results to validate its use when subject to displacement demands typically seen in seismic applications.

Base plates are a commonly overlooked part of structures. Moment-resisting base plates display an even further extensively complex structural system. (Kanvinde, Grilli and Zareian 2012) and (Cooke, Jordan and Kanvinde 2013) involves the most applicable evaluation of base plate connections related to this study. This research also made an effort to incorporate a design procedure for fixed column bases. Measuring strain and displacement at multiple points on the structure will allow for creation of moment-rotation behavior for comparison to component-based experimental research.

1.4 Objectives and Layout of Thesis

The main objective of this research is to quantify and interpret the behavior of a hybrid mezzanine structural system by presenting data from experimental testing. Strain,

displacements, and load measurements will be used to understand how a hybrid structural system reacts when subject to cyclic lateral displacements.

Chapter 2 (Experimental Fixturing and Instrumentation Overview) outlines the test set-up used to collect data during the experimental testing portion of this thesis. The characteristics of the mezzanine structure itself including details such as bolt sizes allow the reader to grasp the full extent of experimental testing. The location of each instrument used, and the manner by which it was installed, is included to allow the reader to understand the basis for experimental data used to reach conclusions.

Chapter 3 (Material Testing) contains the results of all the material tests performed during this thesis. The mezzanine structure outlined in Chapter 2 contains multiple steels. This chapter outlines the stress-strain behavior of each steel used in this system and gives the ASTM specifications of each piece assumed for design.

Chapter 4 (Experimental Results and Discussion) presents results recorded from the instrumentation outlined in Chapter 2. The results presented in this chapter of the report support conclusions with regard to the overall behavior of the structure when subject to cyclic loading.

Chapter 5 (HSS Base Plate Moment-Rotation Curves) takes the experimental results of Chapter 4 to develop further conclusions about the behavior of the base-plate connections in the mezzanine structure. Moment-rotation curves at the base-plate connection of the mezzanine structure at the two instrumented locations are synthesized and discussed.

Chapter 6 (Hysteretic Analysis of Mezzanine) outlines the procedure used to create a hysteretic model for the mezzanine structure based on structural testing outlined

in Chapter 2. The hysteretic model can serve for nonlinear time history analysis of this mezzanine subjected to ground motions generated by seismic activity.

Chapter 7 (Summary and Conclusions) summarizes the results and conclusions and makes recommendations for future research.

CHAPTER 2 - EXPERIMENTAL FIXTURING AND INSTRUMENTATION OVERVIEW

2.1 General Overview

A full-scale mezzanine structure was constructed in the Marquette University Engineering Materials and Structural Testing Laboratory as shown in Figure 1.1 with the framing in Figure 2.1. This structure contains HSS columns and channel beams composed of cold-formed steel erected using the sequence shown in Figure 2.2.

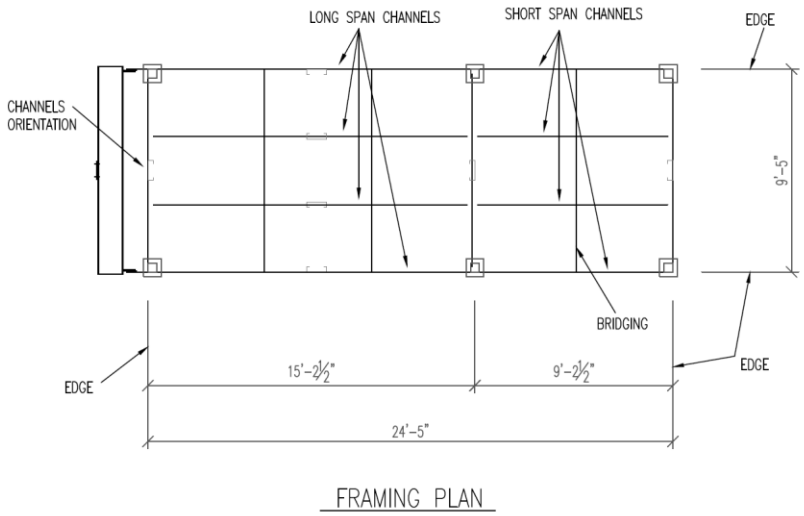

FIGURE 2.1: MEZZANINE FRAMING PLAN

The baseplates of the structure are anchored using wedge-type expansion anchors to cast-in-place reinforced concrete pads secured to the strong floor using threaded rod. Chapter 3 outlines the strength of these anchoring concrete pads which contained #4 rebar spaced at 6 inches on center with a total thickness of 6 inches.

The 1-1/2 inch 20 GA. steel deck was attached using TEK screws attached every 6 inches perpendicular to the deck flutes and every 36 inches parallel to the flutes.

This structure was designed for a 125 pound per square foot live load and 8 pound per square foot dead load. The supporting columns are HSS5X5X3/16, ASTM A500 Grade B steel. The ASTM A36 base plate specifications are given in Figure 2.6 and Figure 2.7. The base plates were anchored to the concrete pads using 1/2 inch diameter power-stud wedge-type expansion anchors with an ultimate strength of 10,190 pound in tension and 9,890 pound in shear with an embedment depth of 4 inch in 6,000 pounds-per-square inch concrete (Powers 2016). All bolts used in connections are 3/4-inch diameter Grade 5 bolts (ASTM A193 equivalent).

FIGURE 2.2: OVERVIEWS OF CONSTRUCTION AND ERECTION OF THE MEZZANINE STRUCTURE

The mezzanine structure was attached to the strong wall in the Marquette University EMSTL using the test set-up shown in Figure 2.3, Figure 2.4, and Figure 2.5, utilizing a connecting plate mounted to a W14x22 beam welded to the extensions of the channel beam members.

Schematics for column C2NC and C3NW are shown in Figure 2.6 and Figure 2.7, respectively. These columns represent typical columns present in this structure. Both of these contain HSS columns with cold-formed channel beams, connected to the columns by cap plates. Beams were connected using steel plates bolted to cold-formed channel webs.

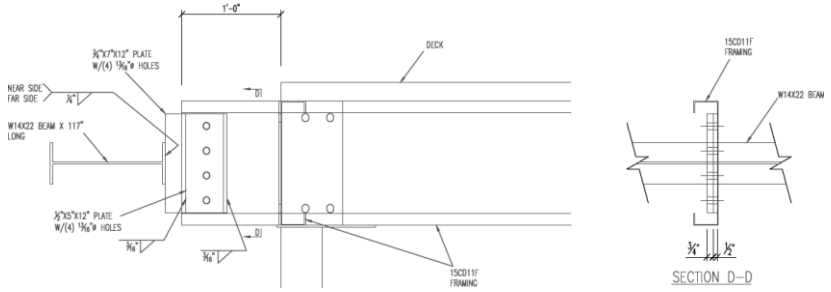

FIGURE 2.3: ACTUATOR ATTACHMENT TO MEZZANINE C-CHANNEL SECTIONS

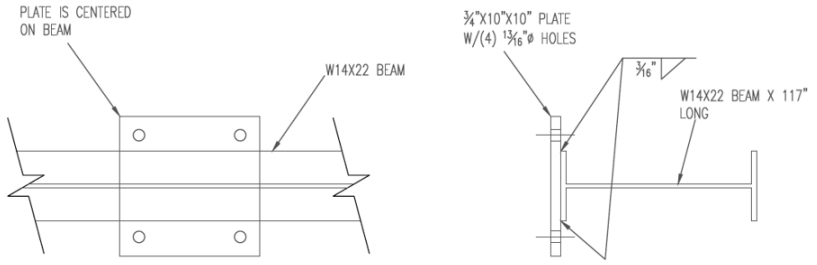

FIGURE 2.4: BEARING POINT OF ACTUATOR TO MEZZANINE STRUCTURE

A variety of systems were necessary to apply loading and collect data during the experiment. This includes an MTS controller which controls the hydraulic actuators and the data acquisition system. Strain, linear variable differential transformers (LVDT), draw wire transducers (DWT), and loading data were collected using LabVIEW software from National Instruments (NI 2014). The data aquistion system and control setup is shown in Figure 2.8.

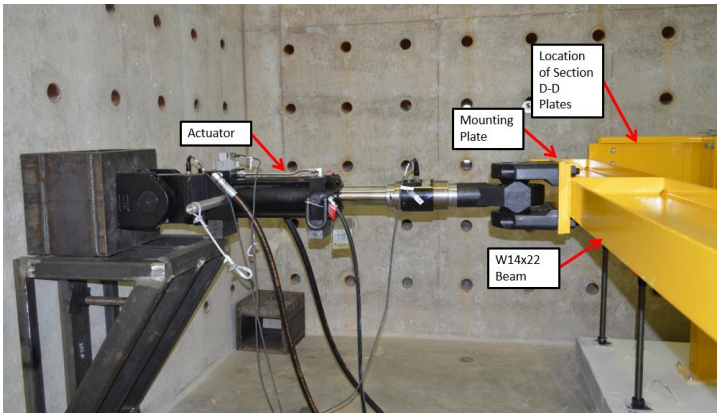

FIGURE 2.5: CONNECTION OF ACTUATOR TO STRONG WALL

DWTs used in this structural test are manufactured by Uni measure (Model No.: PA-30). They contain a maximum displacement range of 30 inches. The DWT average sensistivity (position) is: 32.32482 mV/inch/Ve +/- 0.05% (Ve = Excitation Voltage, mV = millivolts). LVDTs used in the structural testing are manufactured by Vishay Precision Group/Micro Measurements (model: HS100) with a maximum of 100 millimeter displacement. They have a resistance of 305 Ω (ohm) +/- 0.20% with a rate output of 5.227 mV/V (V = volts). Strain gauges used on the mezzanine structure were manufactured by Omega. They have a resistance of 305 Ω +/- 0.35 % and a gauge factor of 2.04 +/- 1.0 %.

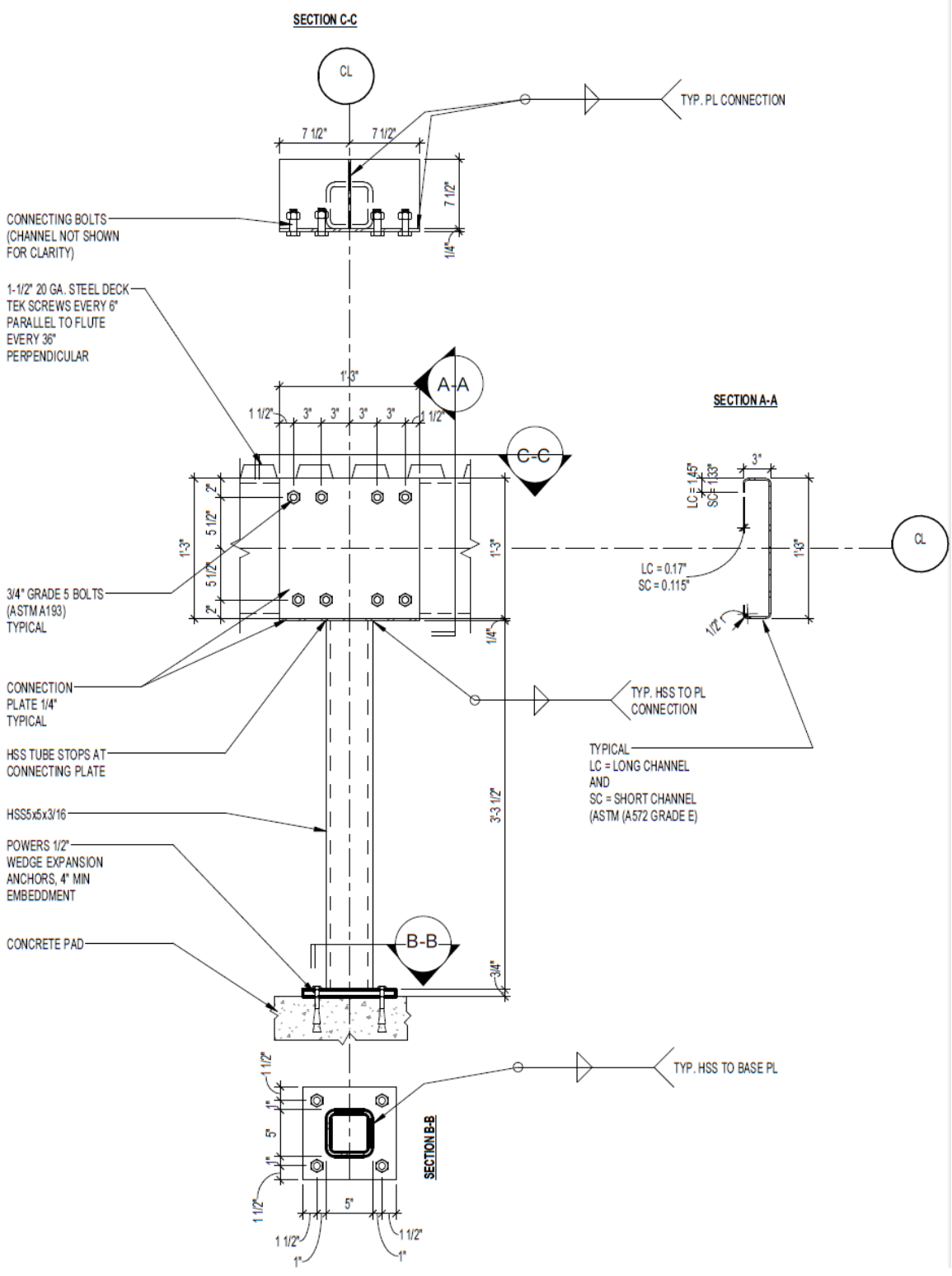

FIGURE 2.6: TYPICAL MID-SPAN MEZZANINE CONNECTION (COLUMN C2NC)

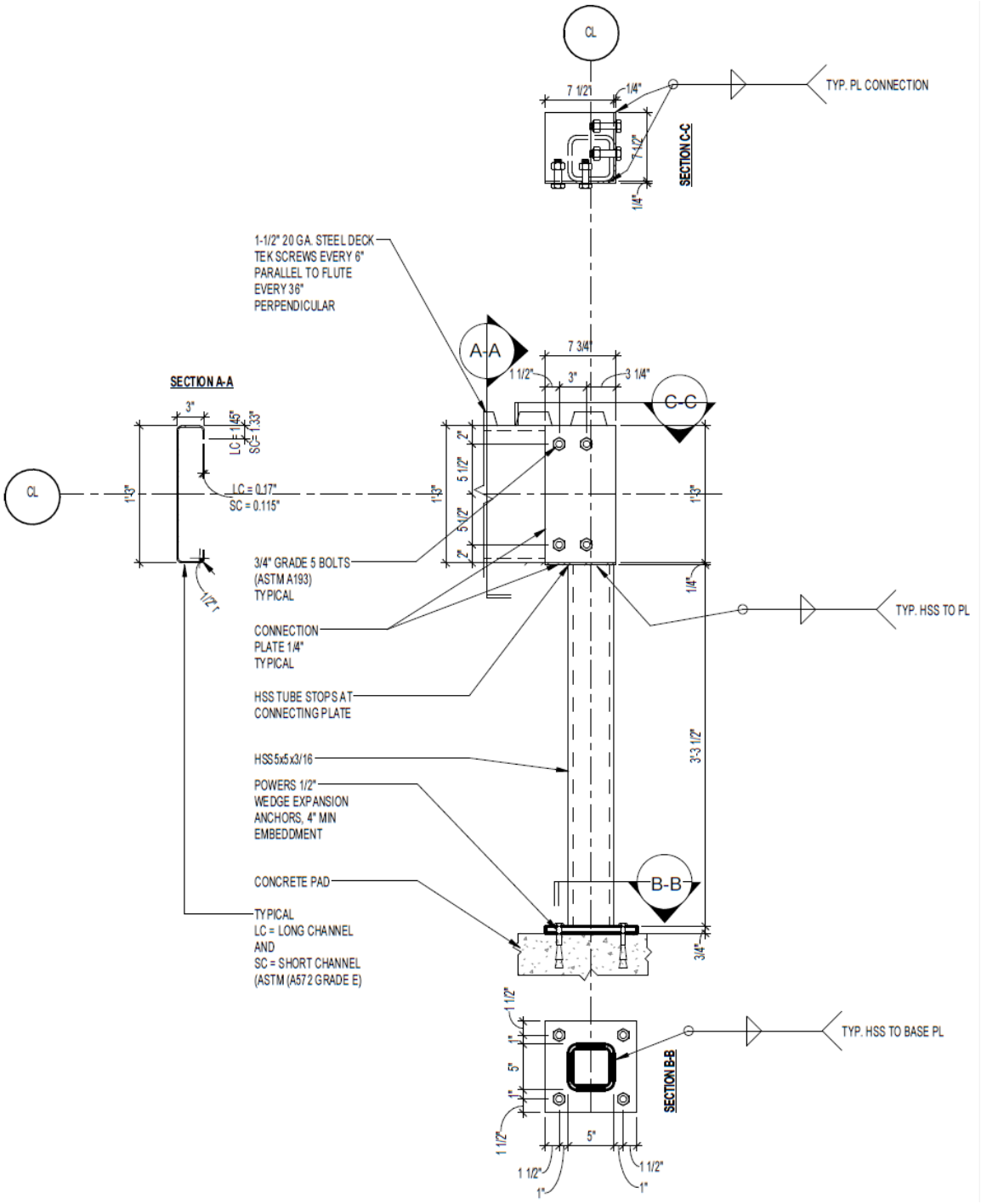

FIGURE 2.7: TYPICAL MEZZANINE END COLUMN (COLUMN C3NW)

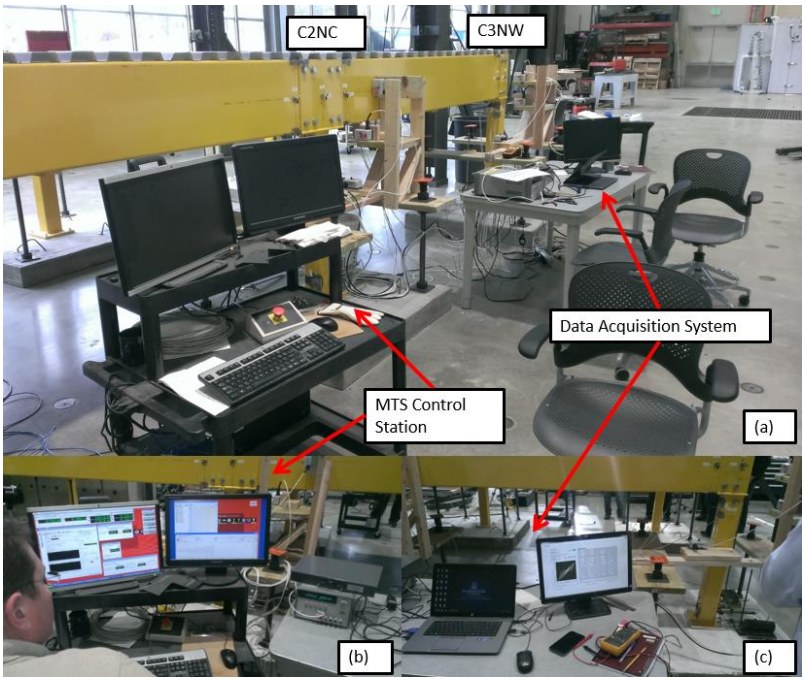

FIGURE 2.8: TEST SETUP: (A) OVERVIEW OF CONTROL SYSTEMS, (B) MTS CONTROL STATION, (C) DATA ACQUISITION SYSTEM.

The data acquisition system chasis used for the mezzanine structural test is the eight slot CompactRIO Reconfigurable Embedded Chasis (CRIO-9111/9114/9116/9118) manufactured by National Instruments. All input/ouput modules collecting strain and displacement data were connected to this chasis. The controller for this chasis is the CompactRIO CRIO-9024. The bridge input module for the strain gauges is the NI 9236 350 Ω, 8-ch, to accomodate all twenty-four strain gauges used during the test. Additional bridges placed in this chasis include NI 9205 32-Channel +/- 10V, 250 KS/s, 16-bit anolog input module for DWTs, LVDTs, and actuator load.

2.2 Column Instrumentation

All experimental testing of the mezzanine structure was completed in the Marquette University Engineering Materials and Structural Testing Laboratory (EMSTL). Sensors

used included draw wire transducers, strain gauges, and linear variable differential transformers. A view of typical strain gauge sensors on the HSS columns and channel beams is given in Figure 2.9 with a view of the overall structural test set-ups in Figure 2.10.

Figure 2.11 gives a view of the instrumentation on column C2NC. Photographic views of the DWT on the cap plate connection are given in Figure 2.12 and of the linear variable differential transformers at the column base in Figure 2.13.

Figure 2.14 gives a view of the instrumentation on column C3NW. Photographic views of the DWT on the cap plate connection are given in Figure 2.15 and of the linear variable differential transformers at the column base in Figure 2.16.

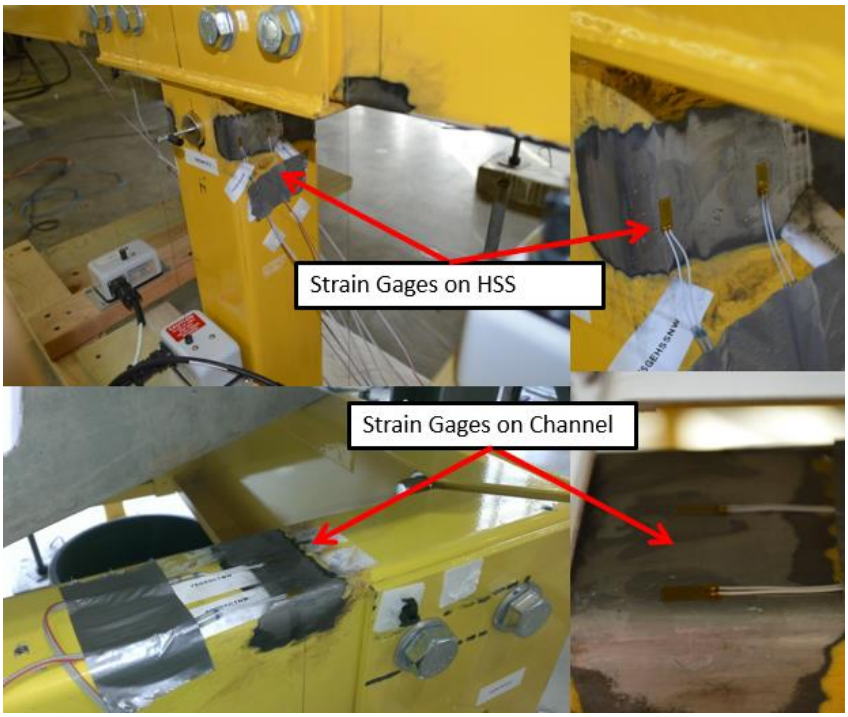

FIGURE 2.9: DISPLAY OF STRAIN GAUGES MOUNTED ON HSS COLUMNS AND CHANNEL BEAMS

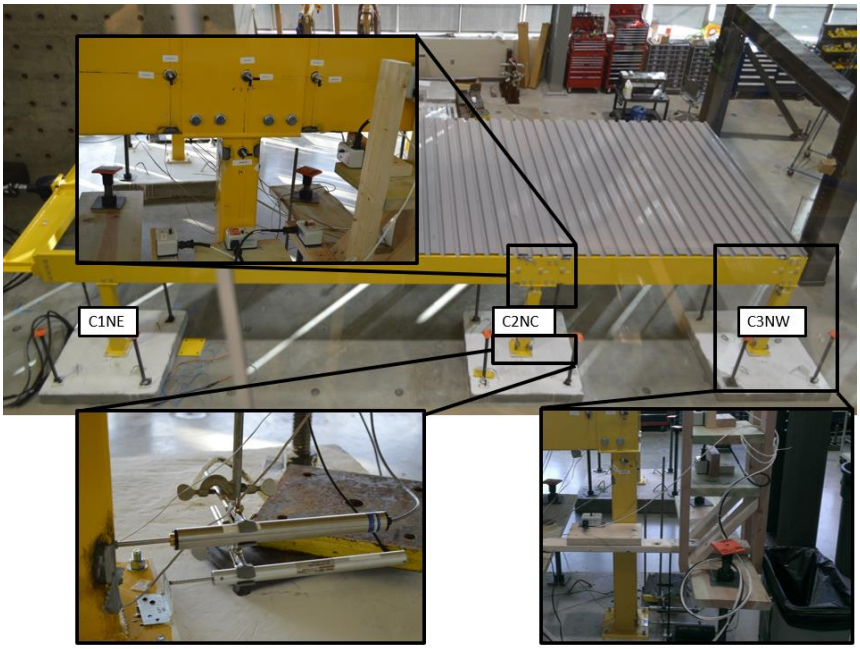

FIGURE 2.10: VIEW OF TYPICAL TEST SET-UPS

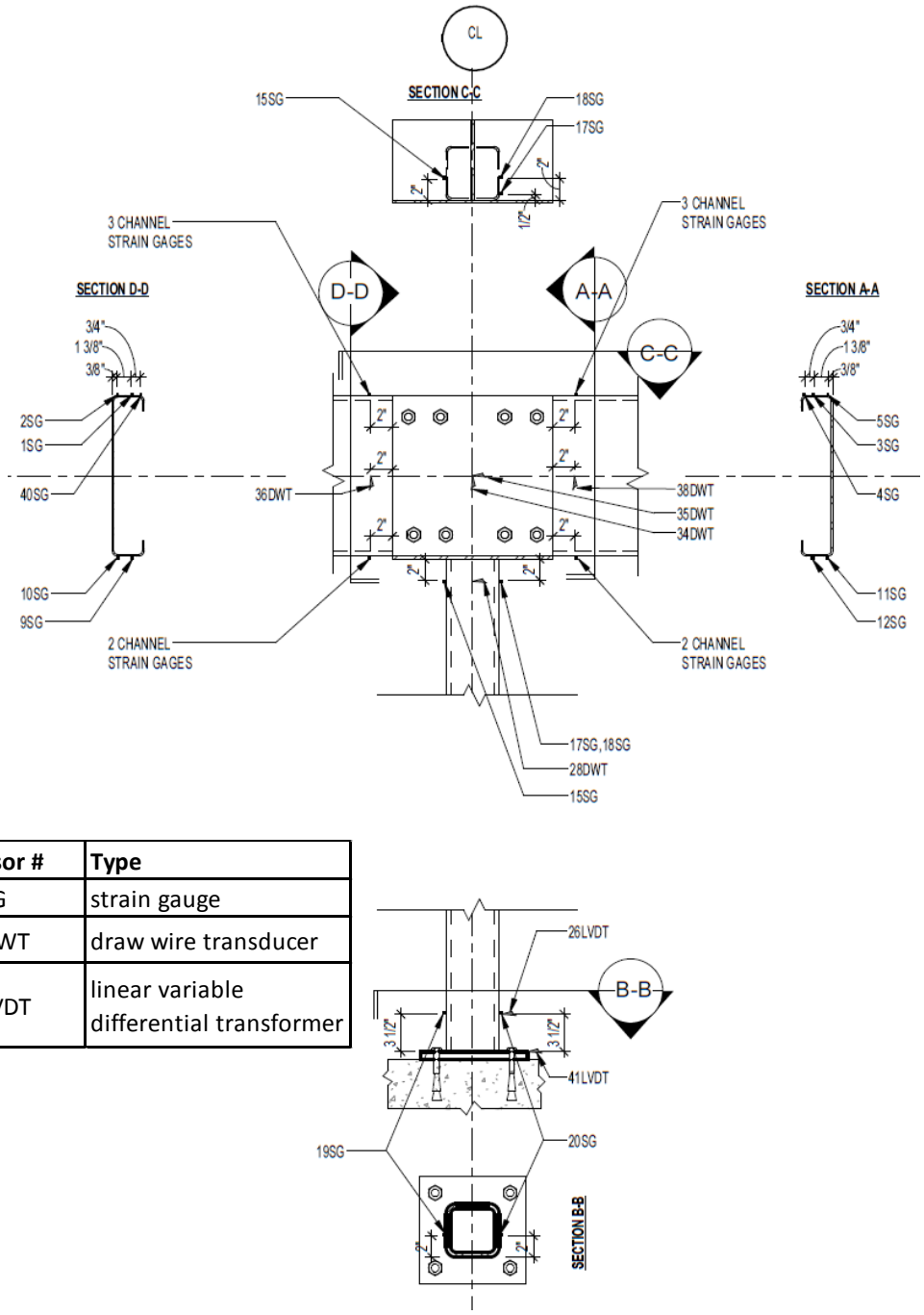

Sensor #	Type
XXSG	strain gauge
XXDWT	draw wire transducer
XXLVDT	linear variable differential transformer

FIGURE 2.11: COLUMN C2NC INSTRUMENTATION

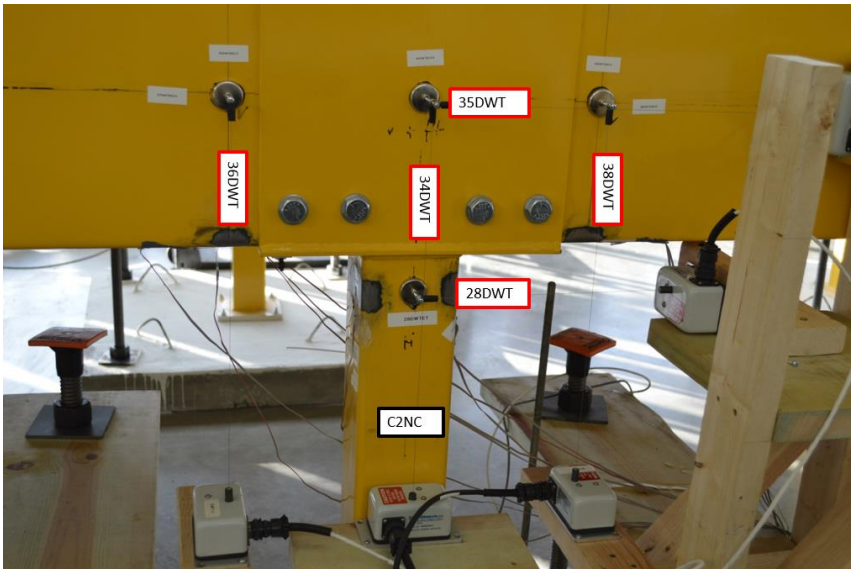

FIGURE 2.12: COLUMN C2NC DRAW WIRE TRANSDUCER (DWT) SENSORS AT TOP

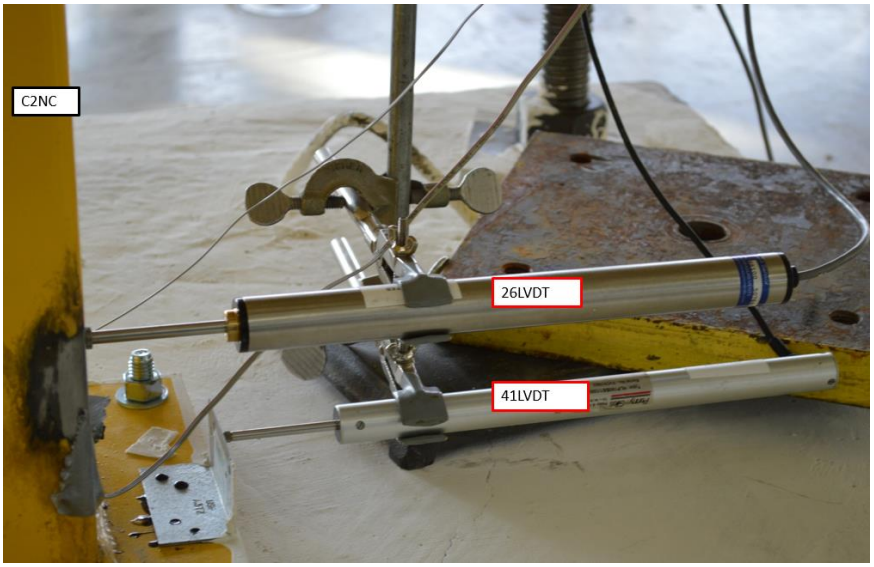

FIGURE 2.13: COLUMN C2NC LVDT SENSORS AT BASE

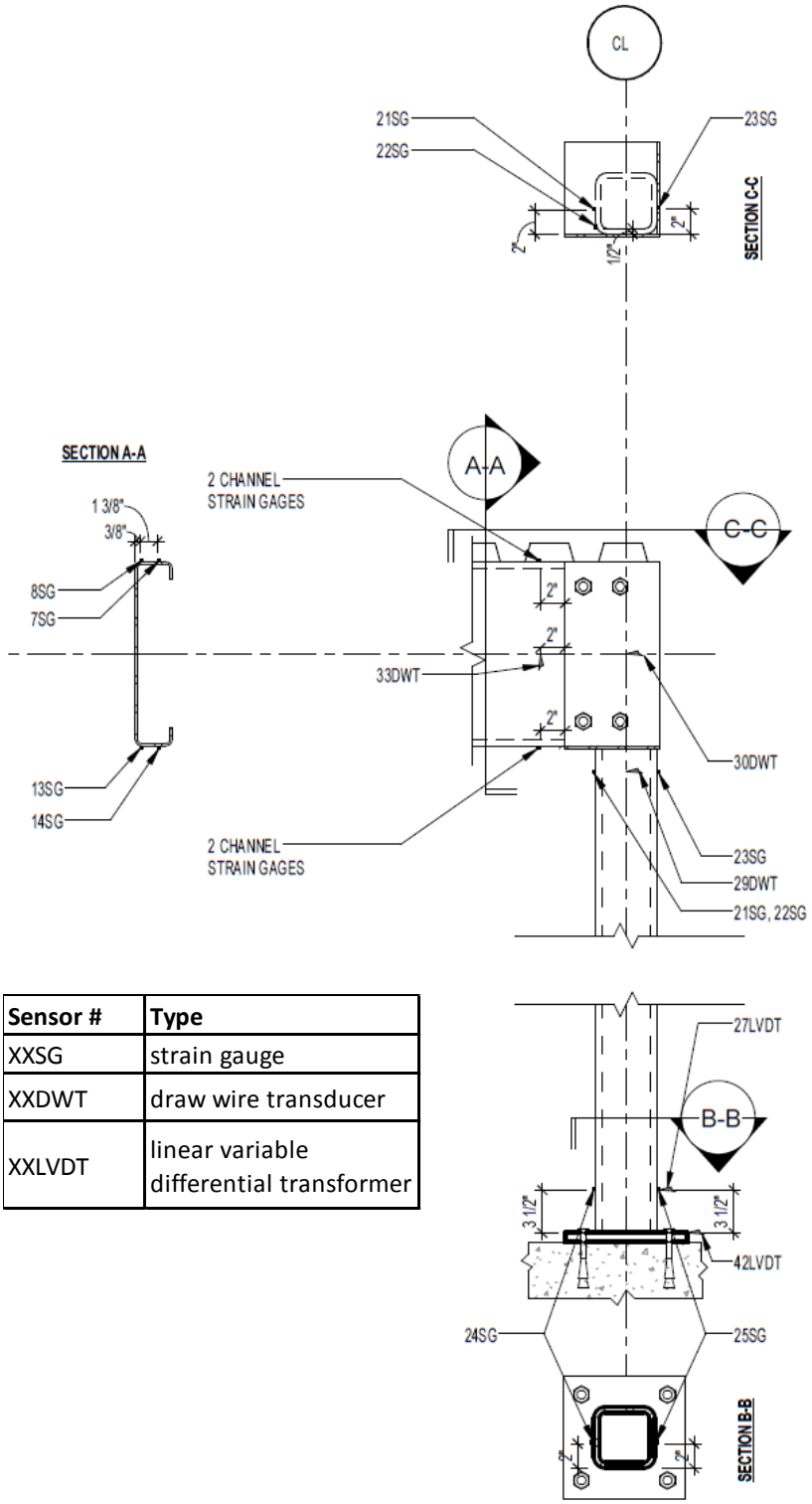

Sensor #	Type
XXSG	strain gauge
XXDWT	draw wire transducer
XXLVDT	linear variable differential transformer

FIGURE 2.14: COLUMN C3NW INSTRUMENTATION

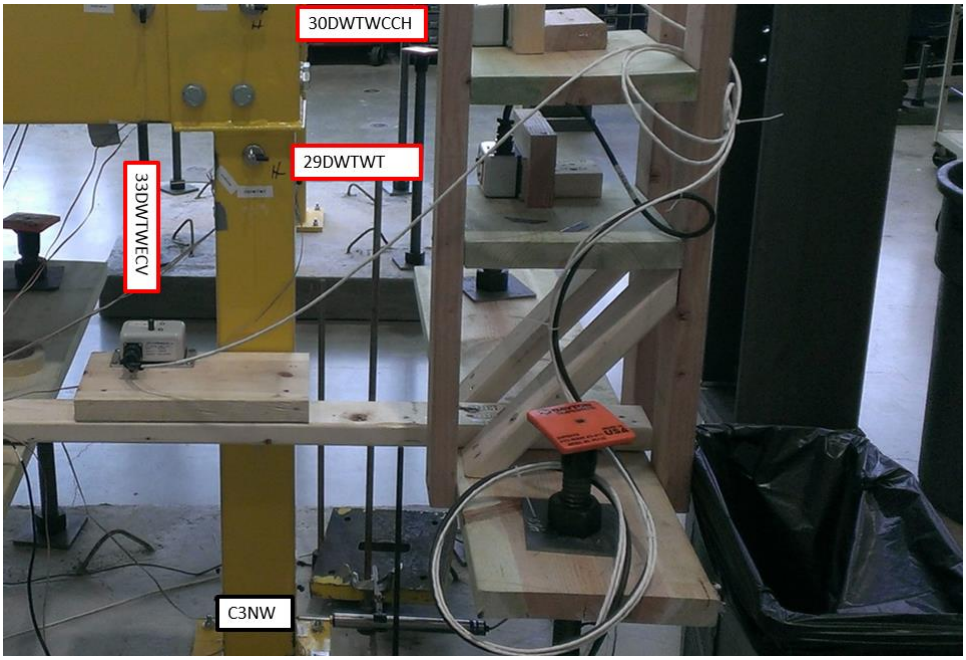

FIGURE 2.15: COLUMN C3NW DRAW WIRE TRANSDUCER (DWT) SENSORS

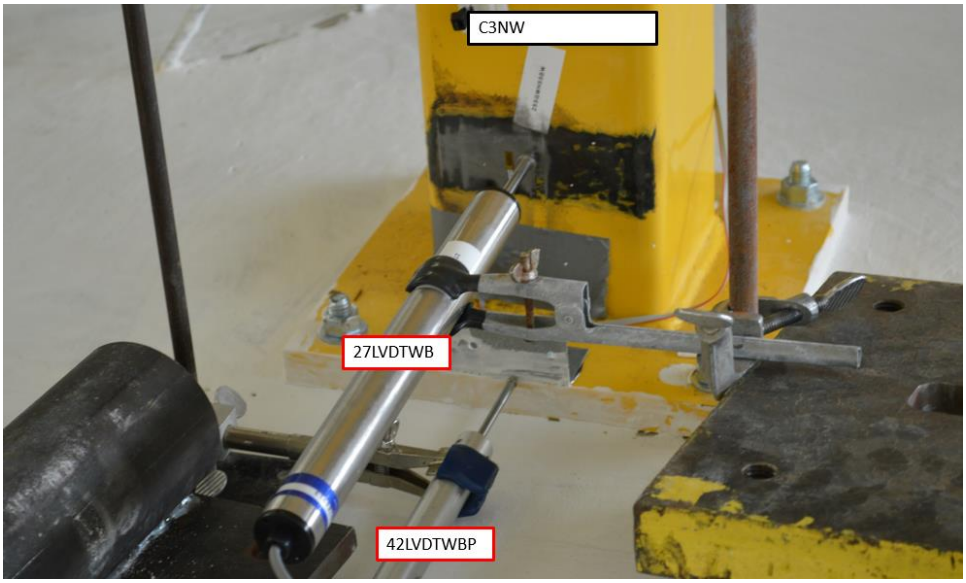

FIGURE 2.16: COLUMN C3NW LINEAR VARIABLE DIFFERENTIAL TRANSFORMER (LVDT) SENSORS

2.3 Displacement Demand Loading Protocol

Displacement demand applied to the mezzanine structure was done through the hydraulic actuator to simulate a far-field earthquake and is the displacement demand protocol required for moment-connection prequalification (AISC 2010). The experimental interstory drift demand protocol considering the height of the structure to be 48 inches is shown in Figure 2.17. Numerical values of the interstory drifts and corresponding cycle numbers are listed in Table 2.1.

This AISC protocol formally ends at 0.04 radians, load step 8 given in Table 2.1 but typically loading is increased 0.01 Radians for a duration of 2 load cycles until failure. In other words, load cycle 9 to load cycle 10 would extend past the required loading for AISC.

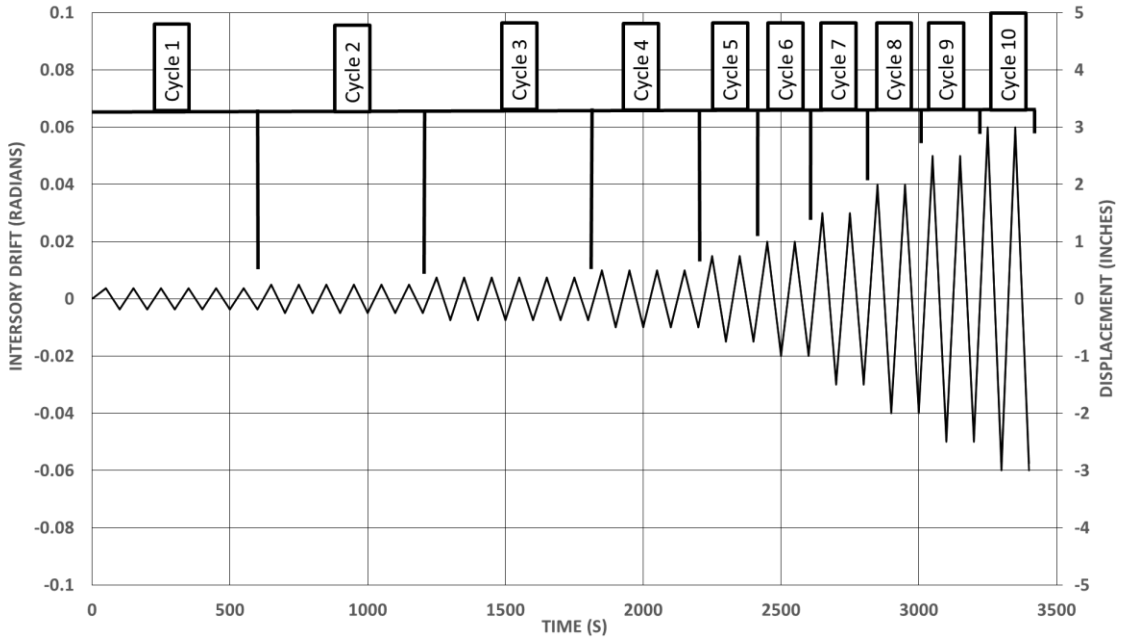

FIGURE 2.17: INTERSTORY DRIFT DEMAND PROTOCOL APPLIED TO MEZZANINE

TABLE 2.1: TABULATION OF APPLIED INTERSTORY DRIFT BY LOAD CYCLE NUMBER

Load Cycle Number	Number of Cycles	Horizontal Displacement (inch)	Interstory Drift Angle (Radians)
1	6	0.18	0.00375
2	6	0.24	0.005
3	6	0.36	0.0075
4	4	0.48	0.01
5	2	0.72	0.015
6	2	0.96	0.02
7	2	1.44	0.03
8	2	1.92	0.04
9	2	2.4	0.05
10	2	2.88	0.06

CHAPTER 3 - MATERIAL TESTING

3.1 Introduction

A suite of material tests were conducted to understand the structural engineering material properties of the components found in the mezzanine system and the cast-in-place foundation pads. The structural steel material tensile test coupons were taken from: the long span channels, the short span channels, the HSS columns, the top connecting plates, and the steel column base plates. Standard 4” by 8” concrete cylinders were cast when the foundation pads were cast.

Tensile testing of steel materials were conducted in accordance with specifications from ASTM A370 (ASTM 2014), and unconfined concrete compressive strength was determined using standard procedures (ACI 214 2011) and (ASTM 2015). The test frames used to perform the tension testing of the steel coupons and unconfined compression testing for concrete are shown in Figure 3.1.

FIGURE 3.1: MATERIAL TESTING EQUIPMENT: (A) STEEL MATERIAL TESTING SETUP USING MTS 100 KIP TEST FRAME, (B) CONCRETE MATERIAL TESTING SETUP USING FORNEY FX500 TEST FRAME.

3.2 Structural Steel

Displacement measurements on the steel tension tests were taken using an extensometer. The tensile testing specimens were fabricated in a dog-bone configuration using ASTM A370 compliant dimensions (ASTM 2014). Three tensile-test specimens were taken from each major component outlined earlier. A general description identifying the materials and testing notes from the uniaxial testing of the steel coupons is available in Table 3.1. Stress-strain curves are given for all of the steel materials in the mezzanine showing the response of the material to failure.

If well-defined yield plateaus were seen during material testing those values were used to determine the material properties in Table 3.2. If the stress-strain curves did not give well-defined yield points, yield in Table 3.2 was determined using the 0.2 percent offset method (ASTM 2014). It should be noted that the location where samples were taken off the cross-section of the steel members is unknown. The modulus of elasticity for each steel coupon was also calculated and displayed in Table 3.2. A typical modulus of elasticity for steel is between 28,000 kips per square inch (ksi) to 30,000 ksi. All of the steel coupons had at least one sample with a recorded value in this range. The material samples in Table 3.1 and Table 3.2 containing the label “extensometer lost during testing” denote tensile tests in which the extensometer used to measure material strain failed to collect measurements due to failure of the attachments used to secure the extensometer to the material sample.

TABLE 3.1: STEEL MATERIAL SAMPLE CONFIGURATION AND SPECIMEN DESIGNATIONS

Code	Cross-Section		Gauge Length (in.)	Method used to Determine Yield
	Thickness (in.)	Width (in.)		
LC-S1	0.170	1.000	2.000	0.2% offset
LC-S2	0.170	1.000	2.000	0.2% offset
LC-S3	0.170	1.000	2.000	0.2% offset
LC-S4	0.170	1.000	2.000	0.2% offset
HSS-S1	0.185	1.000	2.000	0.2% offset
HSS-S2	0.185	1.000	2.000	0.2% offset
HSS-S3	0.185	1.000	2.000	0.2% offset
HSS-S4	0.185	1.000	2.000	0.2% offset
SC-S1	0.115	1.000	2.000	Yield Plateau
SC-S2	0.115	1.000	2.000	Yield Plateau
SC-S3	Extensometer Lost During Testing			
SC-S4	0.115	1.000	2.000	Yield Plateau
CP-S1	Extensometer Lost During Testing			
CP-S2	0.243	1.000	2.000	0.2% offset
CP-S3	0.243	1.000	2.000	0.2% offset
CP-S4	0.243	1.000	2.000	0.2% offset
BP-S1	0.750	0.625	2.000	0.2% offset
BP-S2	0.750	0.625	2.000	0.2% offset
BP-S3	0.750	0.625	2.000	0.2% offset
BP-S4	0.750	0.625	2.000	0.2% offset

Notes:
LC Long Span Channel (ASTM A572 Grade E Steel)
HSS HSS Tube Columns (ASTM A500 Grade B Steel)
SC Short Span Channel (ASTM A572 Grade E Steel)
CP Connecting Plate (ASTM A572 Grade E Steel)
BP Base Plate (ASTM A36 Steel)
S# Specimen Number

TABLE 3.2: STEEL MATERIAL PROPERTIES

Code	σ_y (ksi)	ϵ_y (%)	σ_u (ksi)	σ_{rup} (ksi)	ϵ_{rup} (%)	σ_u / σ_y	ϵ_{rup} / ϵ_y	E (ksi)
LC-S1	57.7	0.41	72.1	59.1	39.71	1.2	96.85	27,695
LC-S2	69.4	0.43	81.3	68.7	39.53	1.2	91.93	28,462
LC-S3	65.0	0.42	80.1	67.7	37.60	1.2	89.52	30,489
LC-S4	72.2	0.44	85.9	72.2	40.35	1.2	91.70	30,295
Average	66.1	0.43	79.8	66.9	39.30	1.2	92.50	29,235
HSS-S1	79.1	0.47	100.7	82.1	30.54	1.3	64.98	29,770
HSS-S2	81.1	0.45	102.6	83.1	32.48	1.3	72.18	33,259
HSS-S3	79.7	0.44	100.9	79.9	32.56	1.3	74.00	29,878
HSS-S4	80.4	0.47	101.7	82.2	32.12	1.3	68.34	30,151
Average	80.1	0.46	101.5	81.8	31.93	1.3	69.87	30,764
SC-S1	90.2	0.37	102.2	84.3	27.81	1.1	75.16	31,523
SC-S2	74.6	0.32	86.4	71.5	26.22	1.2	81.94	30,479
SC-S3	Extensometer Lost During Testing							
SC-S4	97.5	0.39	109.4	93.4	30.52	1.1	77.46	30,863
Average	87.4	0.36	99.3	83.1	28.18	1.1	78.19	30,955
CP-S1	Extensometer Lost During Testing							
CP-S2	75.7	0.48	88.2	67.7	37.43	1.2	77.98	28,025
CP-S3	76.7	0.47	89.1	69.4	34.39	1.2	73.17	27,412
CP-S4	75.7	0.47	89.1	68.7	34.51	1.2	73.43	29,087
Average	76.0	0.47	88.8	68.6	35.44	1.2	74.86	28,175
BP-S1	76.4	0.46	86.4	41.7	33.33	1.1	72.46	29,754
BP-S2	92.6	0.49	104.2	58.8	34.28	1.1	69.96	32,613
BP-S3	90.8	0.50	98.7	52.8	33.28	1.1	66.56	34,194
BP-S4	91.3	0.48	103.6	59.0	34.67	1.1	72.23	35,045
Average	87.7	0.48	98.2	53.1	33.89	1.1	70.30	32,901

Table Abbreviations:

σ_y = Stress at Material Yield
σ_u = Ultimate Stress
σ_{rup} = Stress at Material Rupture
ϵ_y = Strain at Material Yield
ϵ_{rup} = Strain at Material Rupture
σ_u / σ_y = Ultimate Stress to Yield Stress Ratio
ϵ_{rup} / ϵ_y = Rupture Strain to Yield Strain Ratio
E = Modulus of Elasticity

3.2.1 HSS Stress-Strain Curves

Stress-strain curves of the HSS column are given in Figure 3.2. No well-defined upper and lower yield point was found for these sample therefore, the material yield was determined based on 0.2 percent offset method (ASTM 2014). These HSS samples had a very small amount of variability between samples. A large amount of work hardening in the material usually occurs when creating HSS. HSS shapes are usually created from flat sheets of steel and then cold-formed into the required shape. During this cold-forming process the steel material in the corner region of the HSS shape can develop different yield strengths due to the material being deformed plastically from forming of the square, rectangular, or circular shape. This is commonly called work hardening of the material. The extremely low variability in the tensile test results shown in Table 3.2 indicates that it is likely that all the HSS column tensile test samples came from a location on the flat portions of the tubular cross-section away from the corners.

The HSS tube tested was specified to be ASTM A500 Grade B Steel which has a specified minimum yield strength of 46 ksi and no maximum specified yield strength (ASTM 2013). The recorded average yield strength of 80 ksi is typically higher than the ultimate tensile strength of an E70 welds (70 ksi). Specifying ASTM A1085 steel would allow for a specified yield strength of 50 ksi with a maximum yield stress of 70 ksi promoting yielding in the section rather than the potential rupture of the weld material (ASTM 2015).

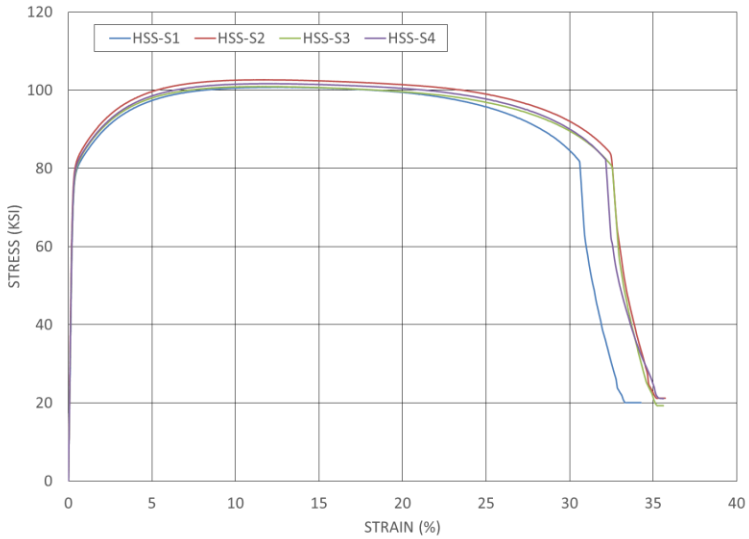

FIGURE 3.2: HSS MATERIAL STRESS-STRAIN CURVES

3.2.2 Long Span Channel Stress-Strain Curves

The long span channel is specified to be ASTM A572 Grade E steel with a minimum required yield stress of 50 ksi which is a high strength low-alloy (HSLA) steel. Stress-strain curves of the long span channel material shown in Figure 3.3 however do not display an extremely well define upper and lower yield plateau. The material yield was determined based on 0.2 percent offset method (ASTM 2014). The absence of the upper and lower yield plateau indicate a significant amount of cold-working has occurred in this coupon. Conversely, a well-defined yield plateau usually indicates minor to no cold-working.

Cold-formed channels are usually created from flat plate (gauge thickness) steel and bent into a required shape. During this cold-working process the corners of the channel develop different strengths due to work hardening. Given the large amount of variability between the material strengths of the long span channel, differing amounts of work hardening must be present in the tested samples (*i.e.* channel flange will have

potential for greater work hardening than a location at the middle of the web). The range of yield stresses and ultimate stresses recorded from this material indicate that work hardening through shape creation likely exists.

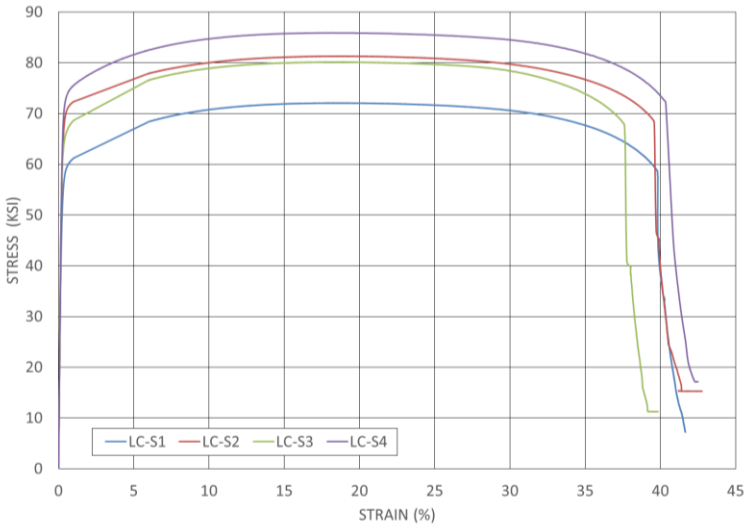

FIGURE 3.3: LC MATERIAL STRESS-STRAIN CURVES

3.2.3 Short Span Channel Stress-Strain Curves

Stress-strain curves of the short span channel material in Figure 3.4 exhibited behavior typical of ASTM A572 Grade E steel, without work hardening. A well define upper and lower yield point is present for determination of material yield. The yield strength however, far exceeds the specified yield of 50 ksi.

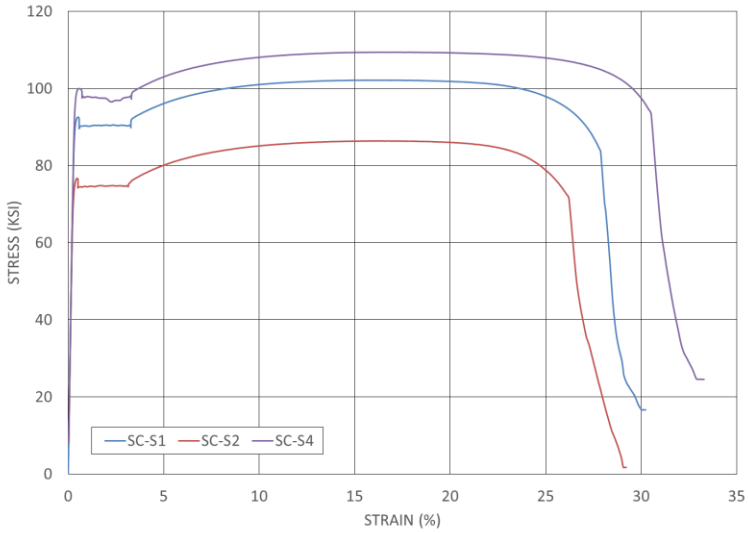

FIGURE 3.4: SC MATERIAL STRESS-STRAIN CURVES

Given the large amount of variability between the material strengths of the short span channels, a certain amount of work hardening through shape formation appears to be present in the tested samples. However, the work hardening did not eliminate the upper and lower yield points. The range of yield stresses and ultimate stress recorded from this material support the idea that work hardening exists in these samples. The long span channel and the short span channel in Figure 3.3 and Figure 3.4 contain the same material specification and meet the required yield stress of 50 ksi however, the behavior of the material is drastically different.

3.2.4 Connecting Plate Stress-Strain Curves

The connecting plates at the top of the HSS columns are specified to be ASTM A572 Grade E steel with a minimum required yield stress of 50 ksi, which is a high strength low-alloy (HSLA) steel. Stress-strain curves of the connecting plate material shown in Figure 3.5 however, do not display enough yield behavior to define yield, therefore the

material yield was determined based on 0.2 percent offset method (ASTM 2014). The reduction in the length of the yield plateau indicates a minor amount of cold-working has occurred in this coupon.

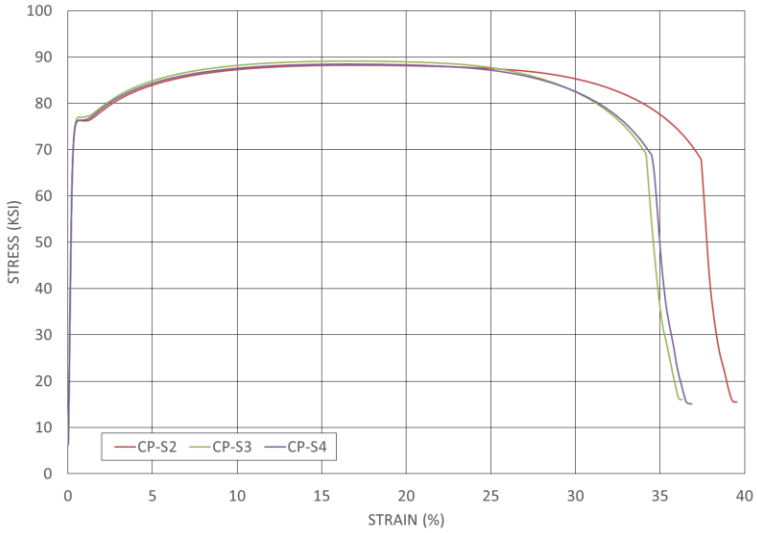

FIGURE 3.5: CP MATERIAL STRESS-STRAIN CURVES

3.2.5 Base Plate Stress-Strain Curves

The stress-strain curves of the base plate material shown in in Figure 3.6 exhibits a large variability between samples with yield strengths ranging from 76.4 to 92.6 ksi. ASTM A36 steel which, prior to the 1994 Northridge Earthquake was commonly used for wide flange steel shapes, is known to have well-defined upper and lower yield points. This sample, however, does not exhibit any yield behavior suggesting significant work hardening in its creation.

A large amount of stress degradation is present after the ultimate strength of the material is reached. The percentage of strain at which the ultimate stress is reached is less

than 10 percent indicating the material has an extremely low ductility. This suggests that the base plate material is cold-worked.

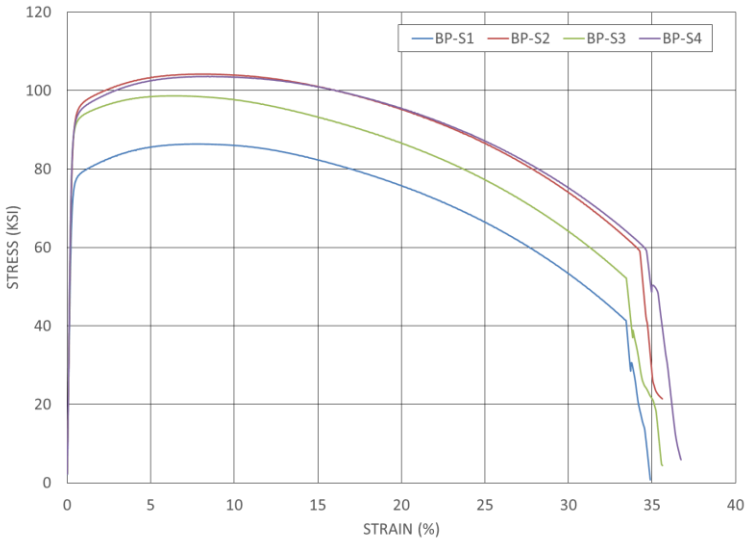

FIGURE 3.6: BP MATERIAL STRESS-STRAIN CURVES

3.3 Cast-in-Place Concrete

The material testing included 28-day unconfined compression tests of cylinders cast at the time the concrete footings for the mezzanine were cast in the laboratory. The results of the compression test used for the concrete pads is contained in Table 3.3. The concrete cylinders were cast on February 12, 2015 and tested on April 3, 2015 a period slightly longer than 28 days.

TABLE 3.3: STRENGTH OF CONCRETE ANCHORING PADS

	Load (lbf)	Stress (psi)
Cylinder 1	89,790	7,145
Cylinder 2	82,575	6,571
Cylinder 3	99,165	7,891
Average	90,510	7,203

Notes:

1.) Tested according to (ASTM 2015) and (ACI 214 2011)
2.) Testing completed using Forney FX500 (Figure 3.1)
3.) Standard ASTM 4" by 8" cylinders were used with elastomeric pads.
4.) lbf = pound force
5.) psi = pound per square inch

3.4 Material Test Summary

Most of the behavior of the steel materials tested in this chapter did not display the classic behavior that is usually associated with the specified material. Rather the cold-working process changed the stress-strain properties of the material to obtain different yield and ductility characteristics. In particular, the long span channel, short span channel, and connecting plate all of which are specified to be ASTM A572 Grade E steel, a typical HSLA steel, exhibited yield stresses far in excess of the specified 50 ksi. The long span channel and the connecting plate do not exhibit well-defined upper and lower yield points however, the short span channel did. The absence of upper and lower yield points indicates a significant amount of cold-working occurred. Unfortunately, the location where the samples were taken from the cross-section is unknown making it difficult to gauge the level of cold-working that occurred to make the shape. An additional anomaly of the ASTM A572 samples is the short span channel which exhibits upper and lower

yield points but has a much higher yield than the long span channel or the connecting plate.

The levels of strain at which rupture occurs for all five test samples is also much different owing to the different levels of cold-working that occurred in the material. The base plate achieves its ultimate stress at less than 10 percent strain indicating a material with very low levels of ductility (uncommon for ASTM A36 material) and has a large amount of degradation after the ultimate stress is reached. The HSS achieves its ultimate stress at around 12 percent strain. The ASTM A572 Grade E test have strains of around 15 to 20 percent at the ultimate strength exhibiting much higher levels of ductility.

CHAPTER 4 - EXPERIMENTAL RESULTS AND DISCUSSION

4.1 Introduction

The mezzanine structural test was performed on complete structure rather than a single connection or component of a structure such as a base plate or moment-connection. Due to this, the numerical results of the entire structure needs to be explained. The cyclic loading applied to the structure is defined previously in Figure 2.17. The explanation of the results will be divided into three sections: the displacements and strains at the moment connections or column tops, the displacements and strains at the bases of the column, and the different measurements of interstory drift in the overall structure.

4.2 Experimental Results at the Moment-Resisting Connections

The tops of both column C2NC and C3NW contain instrumentation in the form of DWTs and strain sensors. The displacement sensor locations are indicated in Figure 4.1. The strain gauges at the top of column C2NC are 15SG, 17SG, and 18SG indicated in Figure 2.11. The strain gauges at the top of column C3NW are 21SG, 22SG and 23SG indicated in Figure 2.14.

4.2.1 Horizontal Displacements at the Moment-Resisting Connections

Horizontal deflections at the tops of the columns are taken from DWT sensors 28DWT and 35DWT on column C2NC and DWT sensors 29DWT and 30DWT on column C3NW. The placement of DWT is given in Figure 4.1 which allows for a reference between the displacement readings from the actuator and the displacements recorded by

the DWT sensors. Results of the DWT deflections measured during the test are presented in Figure 4.2, Figure 4.3, and Figure 4.4.

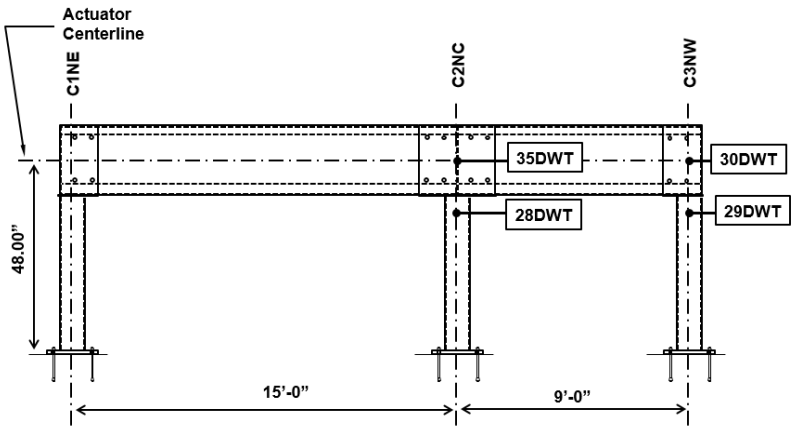

FIGURE 4.1: HORIZONTAL DISPLACEMENT SENSORS AT THE COLUMN TOPS

Figure 4.2 indicates the displacement at the center of the connecting plates measured with draw-wire transducers (sensors 35DWT and 30DWT) and the elongation and contraction of the actuator. The extent of axial shortening of the cold-formed channel beams at these locations can be quantified with this plot. At the peak of each push stroke (negative displacement) the displacement of the actuator is larger than the displacement of 35DWT supporting the idea that the channel beams are compressing and becoming shorter. Similarly on the pull stroke of the actuator (positive displacement) the displacement of the actuator is larger than 35DWT indicating an elongation of the channel beams.

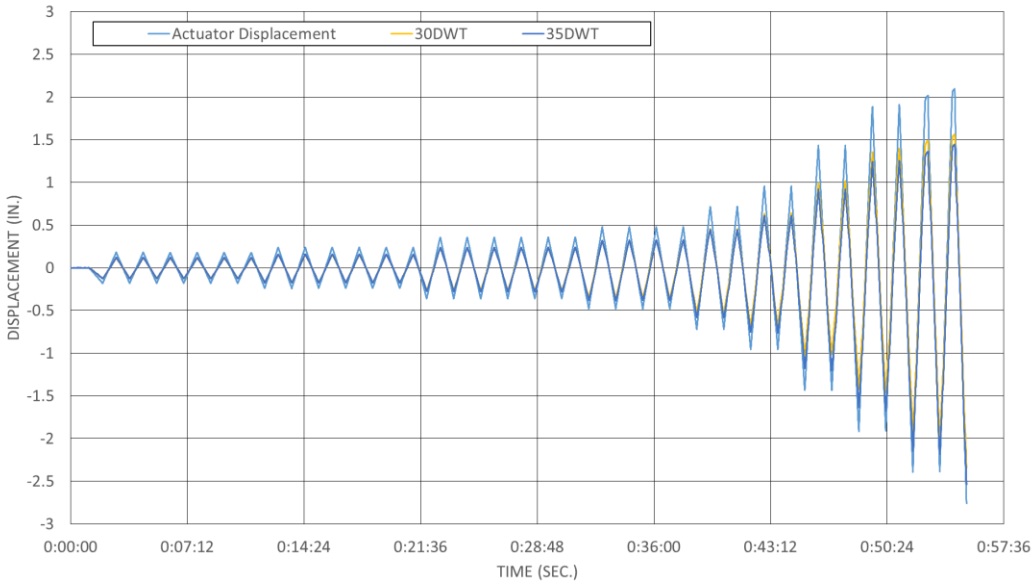

FIGURE 4.2: HORIZONTAL DISPLACEMENTS AT CONNECTION CENTERS AND THAT IN THE ACTUATOR

Figure 4.3 and Figure 4.4 indicate the displacement at columns C2NC and C3NW. The difference between 28DWT and 35DWT, and 29DWT and 30DWT arises from the slip in the bolt holes and rotation in the connection at columns C2NC and C3NW, respectively during structural testing. As the mezzanine displaces, the deformed shape of the columns due to the applied moments causes locations at higher elevations on the column to have larger amounts of displacement. This is indicated in Figure 4.3 during peak actuator pull strokes (positive displacement) at column C2NC, which shows smaller displacements from 28DWT than 35DWT. Column C3NW also indicates this in Figure 4.4 with smaller displacements at 29DWT than 30DWT.

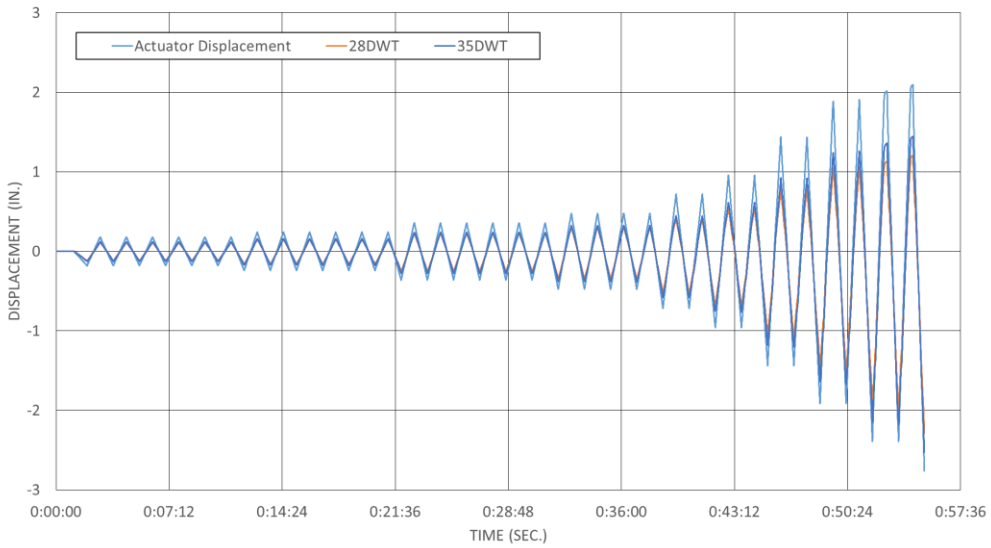

FIGURE 4.3: DISPLACEMENTS AT COLUMN C2NC

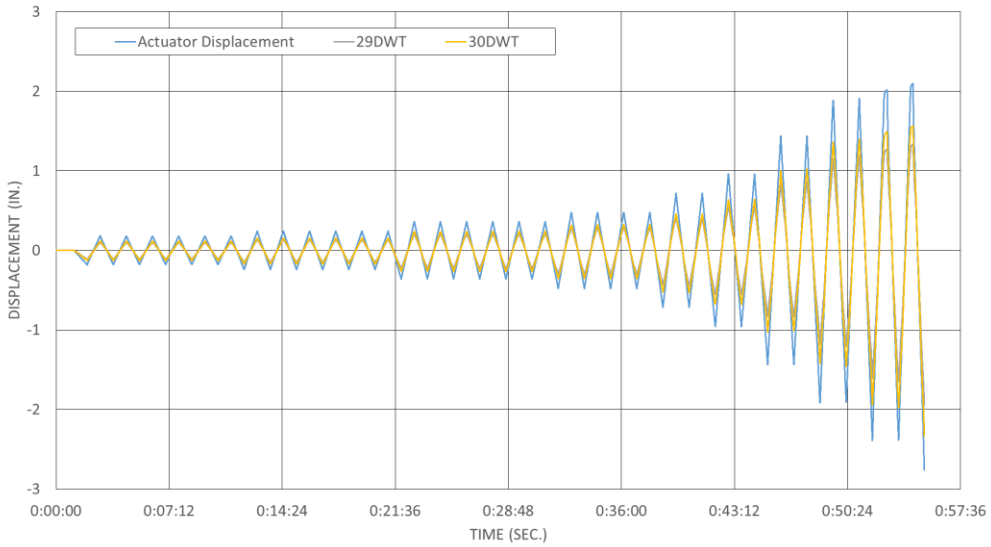

FIGURE 4.4: DISPLACEMENTS AT COLUMN C3NW

The DWT displacements at the top of columns C2NC and C3NW can be used to define the rotation in the connection at the top of the HSS column members. The connection rotations are calculated using Equation 4.1 and Equation 4.2.

$$\boldsymbol{\theta}_{C2NC} = \frac{\Delta_{35DWT} - \Delta_{28DWT}}{9.5\ inches} \qquad 4.1$$

$$\theta_{C3NW} = \frac{\Delta_{30DWT} - \Delta_{29DWT}}{9.5\ inches} \quad 4.2$$

Note that positive rotations correspond to actuator push strokes. The rotation is defined relative to the center of the bolted joint at the top of the HSS column and the length between DWT sensors is defined as 9.5 inches given in Chapter 2. Rotation at the top of columns C2NC and C3NW is calculated based on sensors 35DWT and 28DWT, and 30DWT and 29DWT, respectively. The rotation at the top of the HSS columns is displayed in Figure 4.5.

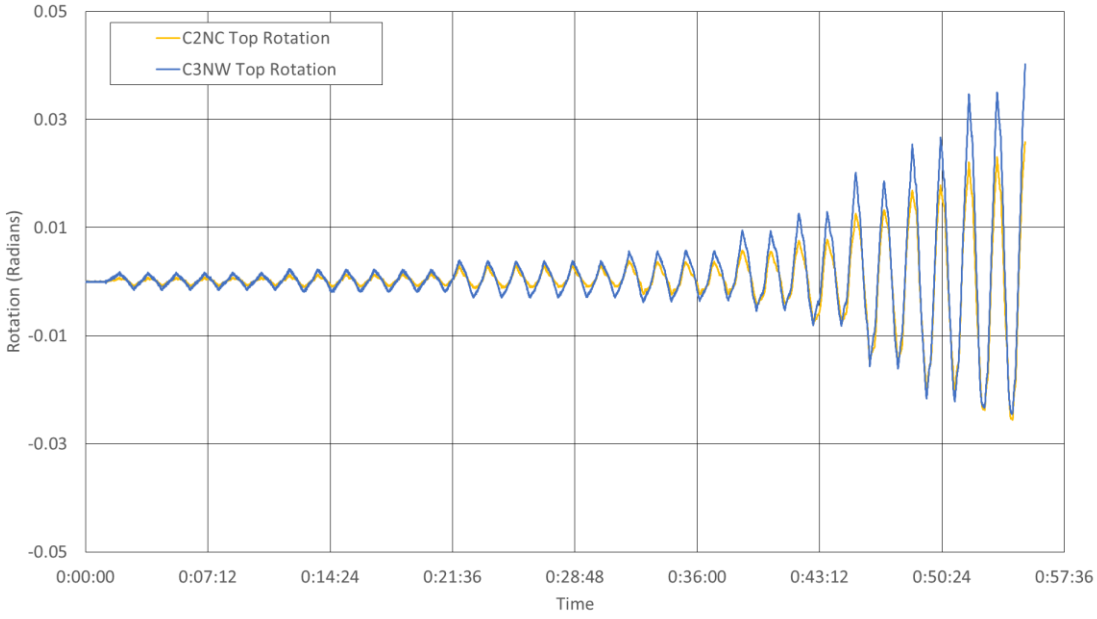

FIGURE 4.5: TOP CONNECTION ROTATIONS OF HSS VS. ACTUATOR LOAD

The increased amount of positive rotation from column C3NW over C2NC occurs due to the absence of a second beam framing into the column. When a positive rotation occurs, the short channel rotates off the cap plate of column C3NW. Unlike column C2NC, which has two channels framing into the column, C3NW does not have another

beam framing into the top of the column to resist the increased positive rotation. During negative rotation, however, the short channel presses down on the cap plate decreasing the amount of rotation in the connection. This causes positive rotation in C3NW to have greater magnitude and emphasizes the conclusion that bearing on the cap plate does more to limit rotation than the eccentrically loaded bolt group.

Column C2NC which has channel beams framing into the top of both sides will have a channel pressing down on the cap plate during both positive and negative rotations causing them to be relatively equal in magnitude. The unequal stiffness of the two channel beams due to their difference in material thickness and span length accounts for the slight difference in magnitude as well.

4.2.2 Experimental Strain at the Moment-Resisting Connections

Strain data was collected from both C2NC (15SG, 17SG, and 18SG) and C3NW (21SG, 22SG and 23SG) at the column tops with sensor specification details indicated in Figure 2.11 and Figure 2.14. Note that all HSS in this structure are standard HSS5x5x3/16.

The strains on the top of column C2NC are presented in Figure 4.6. The strains at the top of this column exceed the material yield strength. Strain gauge 17SG indicates much higher strain magnitudes, which is consistent with the resulting weld fracture at the column tops (see later sections of the chapter). The sub-figure of Figure 4.6 indicates the orientation of the column cap plate relative to the strain sensors. Reference chapter 2 for further dimensions. Strain gauges 15SG and 18SG have consistent levels of strain until the last three load cycles.

Typically in an HSS tube, the strain is higher at the corners of the tube than on the flat sidewall, partially causing the increase in strain of 17SG relative to 18SG. The cap plate connection has a vertical plate directly over 17SG which accounts for the increased levels of strain. During the push stroke of the actuator, the side of the tube containing 17SG is in compression producing positive strain and causing the vertical cap plate to funnel strain into the corner of the tube containing 17SG.

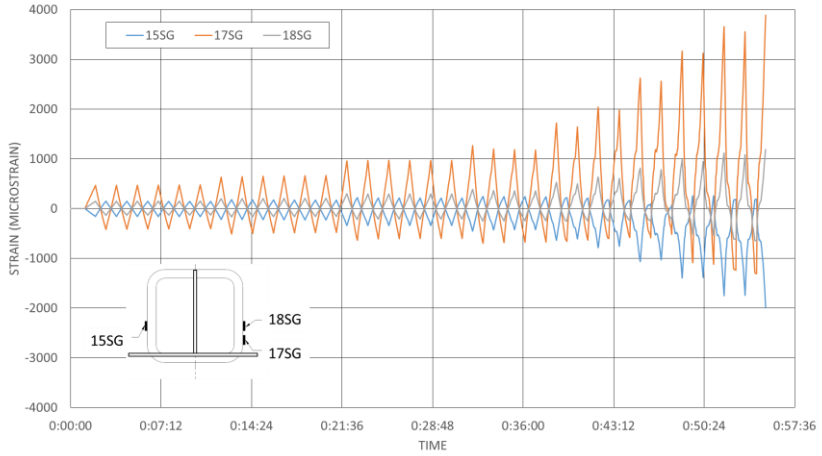

FIGURE 4.6: STRAIN DATA OF COLUMN C2NC TOP SENSORS

The strains on top of column C3NW are presented in Figure 4.7. The strain on the top of column C3NW do not exceed material yield. 22SG indicates much higher concentrations of stress than other gauges on the top of this HSS due to its proximity to the cap plate of the HSS column indicated in the sub-figure of Figure 4.7. During a push stroke of the actuator the side of the tube containing 22SG is in tension producing a negative strain. During a compressive force from the actuator, the cap plate funnels strain into the corner of the HSS, similar to column C2NC. The connecting plate above the sidewall of the tube containing 23SG stiffens the sidewall of the tube, accounting for some of the inconsistent strains observed between 21SG and 23SG.

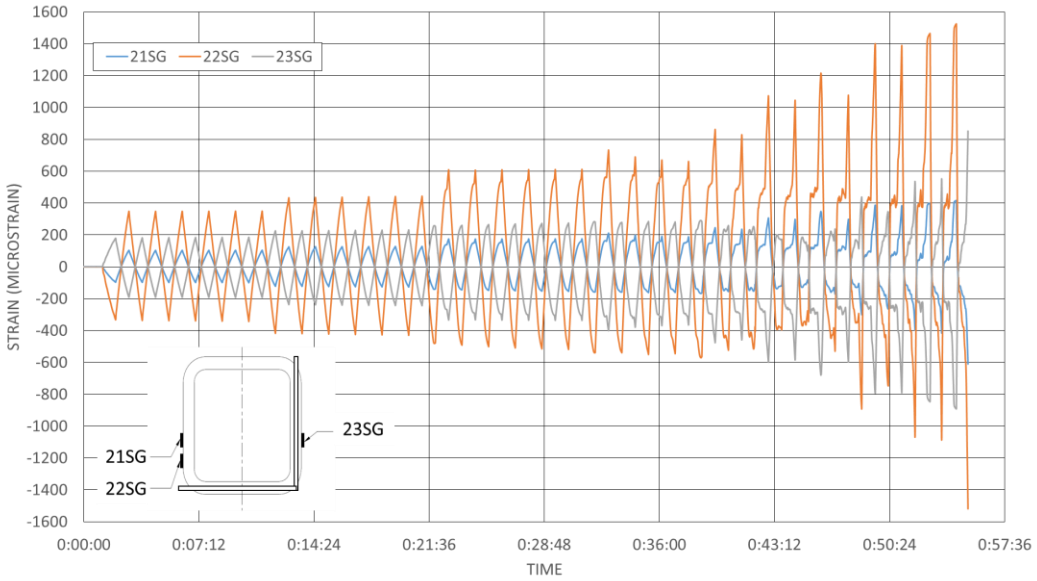

FIGURE 4.7: STRAIN DATA OF C3NW TOP SENSORS

4.3 Experimental Results at the Column Bases

The base of both column C2NC and C3NW contain instrumentation in the form of LVDTs and strain sensors. The displacement sensors are indicated in Figure 4.8. The strain gauges at the base of column C2NC are 19SG and 20SG indicated in Figure 2.11. The strain gauges at the base of C3NW are 24SG and 25SG indicated in Figure 2.14.

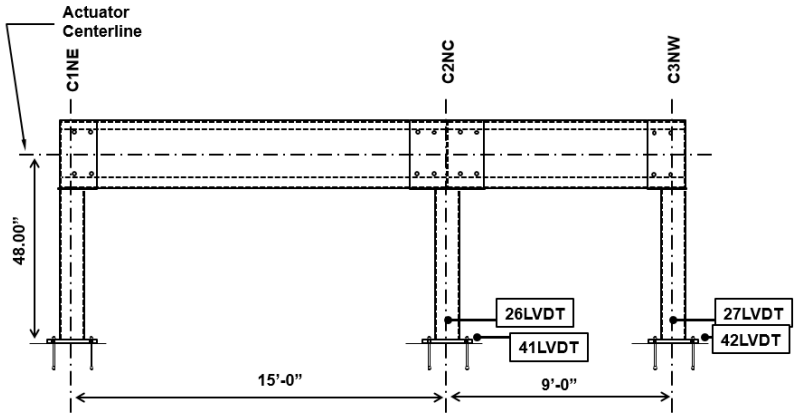

FIGURE 4.8: HORIZONTAL DISPLACEMENT SENSORS AT THE COLUMN BASES

4.3.1 Displacement Results at Column Bases

Displacements at the base of the column structure are taken using LVDTs and displayed for column C2NC in Figure 4.9 and C3NW in Figure 4.10. These measurements help quantify how the structure interacts with its foundation. Figure 4.9 includes deformation measured by 41LVDT beyond the bolt hole clearance dimension indicated by horizontal black lines in both Figure 4.9 and Figure 4.10. The displacement in 41LVDT is roughly double that of 42LVDT, in Figure 4.10, indicating twice as much slip. Both columns indicate slip below the base plate of column immediately from the start of structural testing in the figure sub-plots. It is clear from Figure 4.9 and Figure 4.10 that there is base plate sliding and anchor bending at the base of columns C2NC and C3NW, demonstrated by the displacements measured in 41LVDT and 42LVDT greatly exceeding the bolt hole clearance dimensions. The bolt hole clearance in the base plate is 1/16 inch (0.0625 inch) or 1/32 inch on each side of the anchor if it is perfectly centered in the bolt hole. Any deformations beyond this point at 41LVDT and 42LVDT indicate anchor bending or deformation of the base plate holes. Flat segments at the peaks of 41LVDT and 42LVDT indicate deformation when the base plate stops due to the anchor rods coming into bearing.

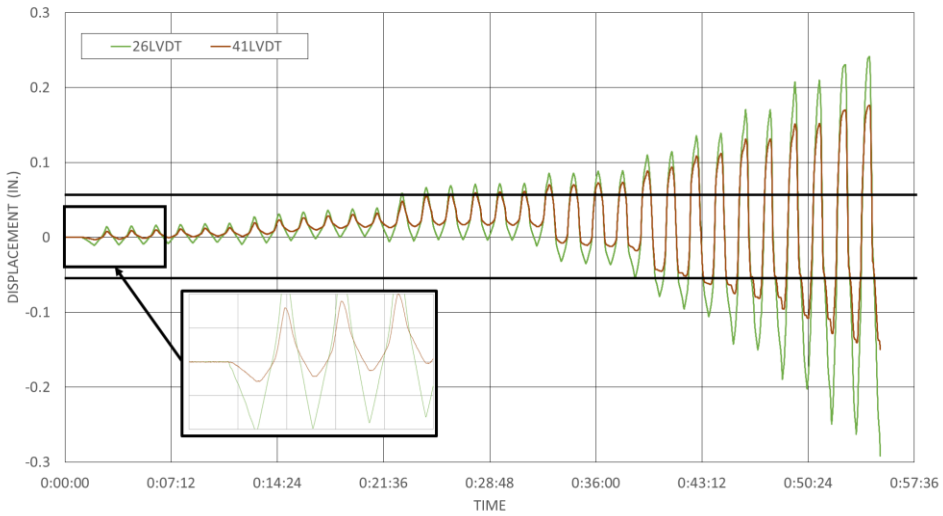

FIGURE 4.9: DISPLACEMENT AT COLUMN C2NC BASE

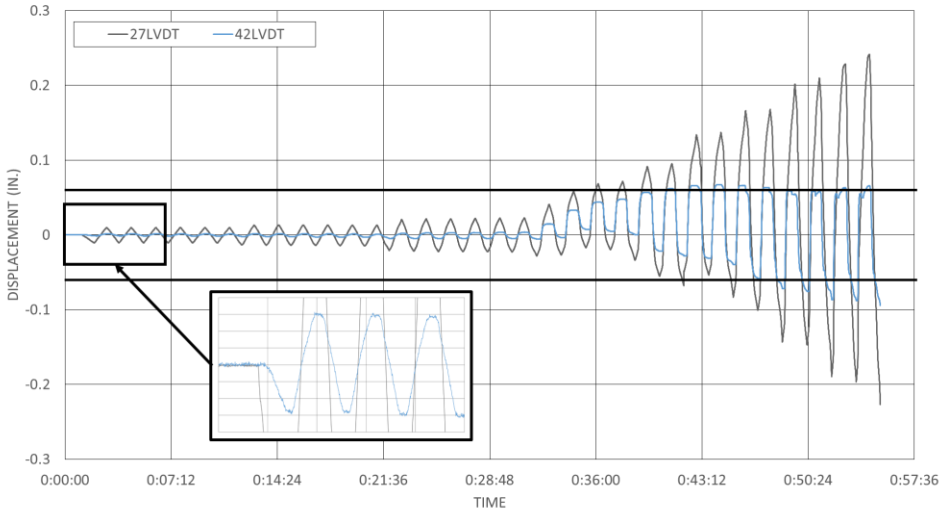

FIGURE 4.10: DISPLACEMENT AT COLUMN C3NW BASE

The LVDT displacements at the base of the structure facilitate measuring of the rotation at the base plate connection. The lengths between the sensors in Figure 2.11 and Figure 2.14 can be used to compute connection rotation using Equation 4.3 and Equation 4.4.

$$\boldsymbol{\theta}_{C2NC} = \frac{\Delta_{41LVDT} - \Delta_{26LVDT}}{3.5\ inches} \qquad 4.3$$

$$\boldsymbol{\theta}_{C3NW} = \frac{\Delta_{42LVDT} - \Delta_{27LVDT}}{3.5\ inches} \quad 4.4$$

Note that positive rotations correspond to push strokes of the actuator. Rotations at the base of the column bases is shown in Figure 4.11. Figure 4.11 shows a large difference in rotational demand at the column bases. This is consistent with the LVDT measurements in Figure 4.9 and Figure 4.10, which show symmetric base translation about the x-axis. This column base shown in Figure 4.11 is consistent with base plate sliding, bending of the expansion anchors, and crushing and cracking of the concrete at the base plate connection.

When comparing the plots of rotation at the top of the columns given previously in Figure 4.5, column C3NW has greater positive rotations at the top and greater negative rotation at the bottom. The previous discussion regarding a singular beam framing into the top of column C3NW explains this behavior. During positive rotations at the base of column C3NW the short span channel beam at the moment-resisting connection lifts off the cap plate decreasing the rotational demand at the base plate. When the channel beam bears on the column cap plate it causes increased rotational demand at the column base plate. Column C2NC has unbalanced rotational demand at the bottom and top. The imbalance is much greater at the bottom.

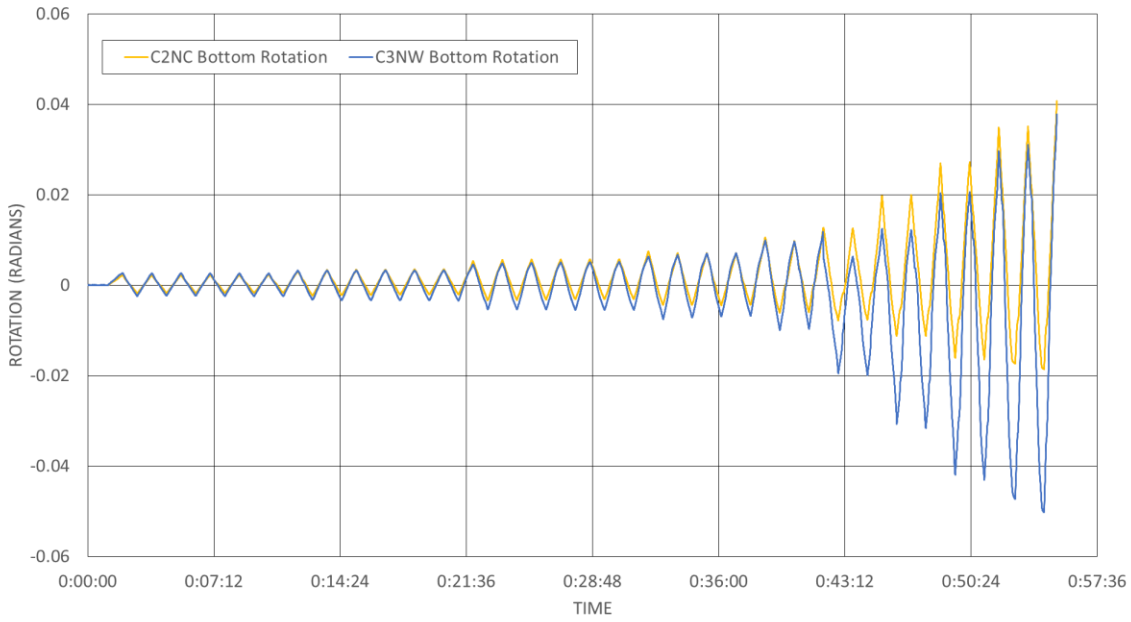

FIGURE 4.11: BASE PLATE ROTATION OF HSS VS. ACTUATOR LOAD

4.3.2 Experimental Strain Results at Column Bases

Strain data was collected at the column bottoms from both C2NC (19SG and 20SG) and C3NW (24SG and 25SG) with sensor specification details indicated in Figure 2.11 and Figure 2.14. Note that all HSS in this structure are HSS5x5x3/16.

Strains measured at the bottom of column C2NC are presented in Figure 4.12. The magnitudes of strain are significantly different on push versus pull actuator strokes. There is limited axial load applied to the HSS column (structure self-weight). Isolating the uniform strain due to axial compression from bending strain will help to assess the magnitude of axial loads in the columns. The average of 19SG and 20SG is calculated using Equation 4.5, Equation 4.6 and Equation 4.7 then provide the pure bending strain of 19SG and 20SG. Average and bending strain are shown in Figure 4.13 and Figure 4.14, respectively. Figure 4.14 illustrates that before the completion of the first load cycle, symmetry does not occur between the push and pull load cycles. Load cycles are defined

in Figure 2.17. Note also, strains at the base of the columns did not exceed material yield at either column.

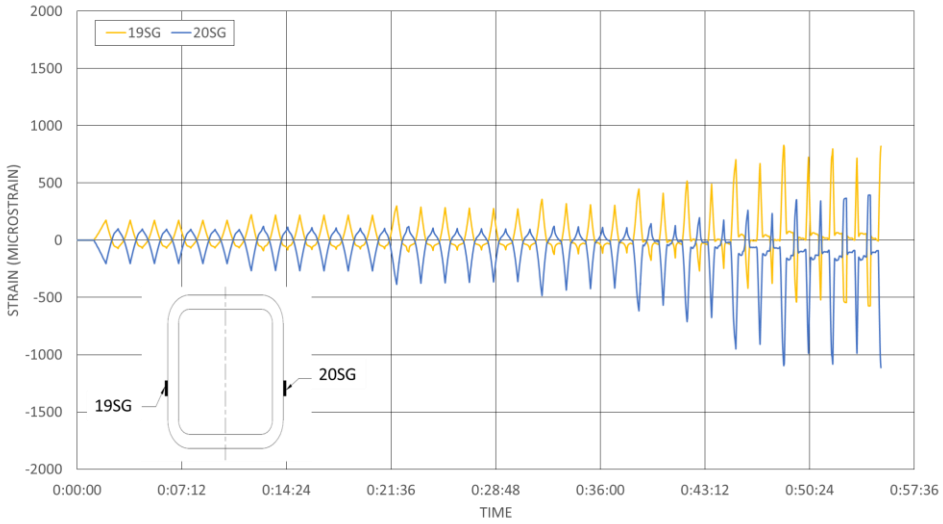

FIGURE 4.12: STRAIN DATA OF COLUMN C2NC BOTTOM SENSORS

$$Average = (1/2)(19SG + 20SG) \quad 4.5$$

$$19SG\ Pure\ Bending = (19SG) - Average \quad 4.6$$

$$20SG\ Pure\ Bending = (20SG) - Average \quad 4.7$$

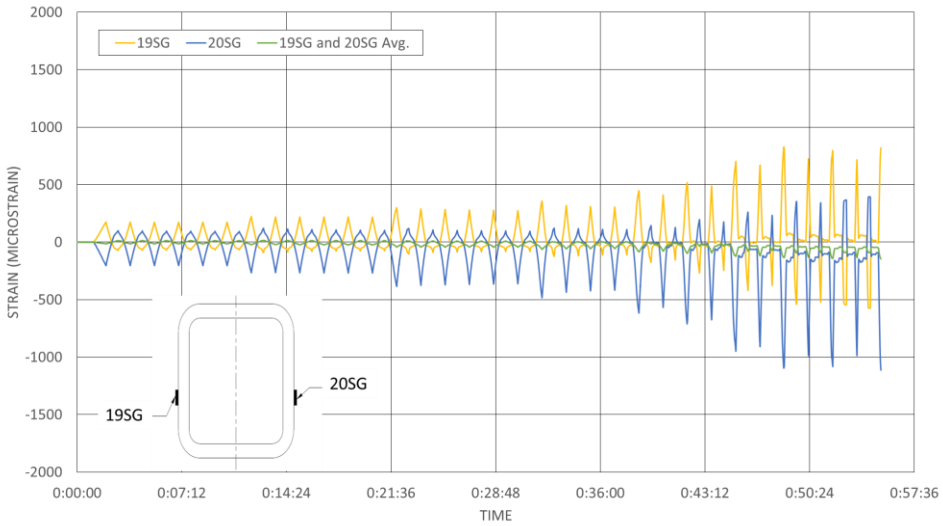

FIGURE 4.13: STRAIN DATA FROM 19SG, 20SG, AND AVERAGE STRAIN (C2NC)

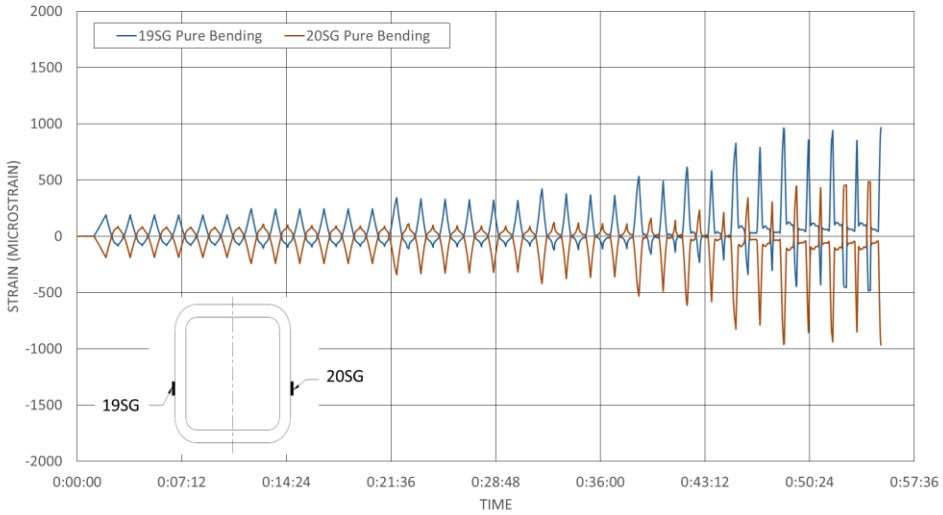

FIGURE 4.14: PURE BENDING STRAIN OF 19SG AND 20SG STRAIN SENSORS (C2NC)

The magnitude of axial strain at the base of C2NC is very small (Figure 4.13) so axial loads resulting from lateral displacement demands are small (as expected). The bending stiffness of column C2NC is greater on the push stroke when compared to the pull stroke. Therefore, strain magnitudes at the base are greater on push strokes. Measurements of strains at the bottom of column C3NW are shown in Figure 4.15. The uniform strain due to axial loads in the column is calculated using Equation 4.8. Equation

4.9 and Equation 4.10 then provide the pure bending strain for 24SG and 25SG. Figure 4.17 illustrates that before the completion of the first load cycle, symmetry does not occur between the push and pull load cycles. Figure 4.16 illustrates that the average (axial) strain components are small relative to the total measured strains (as expected for the MRF system). Figure 4.17 illustrates the pure bending strains measured at the base of column C3NW.

$$Average = (1/2)(24SG + 25SG) \quad 4.8$$

$$24SG\ Pure\ Bending = (24SG) - Average \quad 4.9$$

$$25SG\ Pure\ Bending = (25SG) - Average \quad 4.10$$

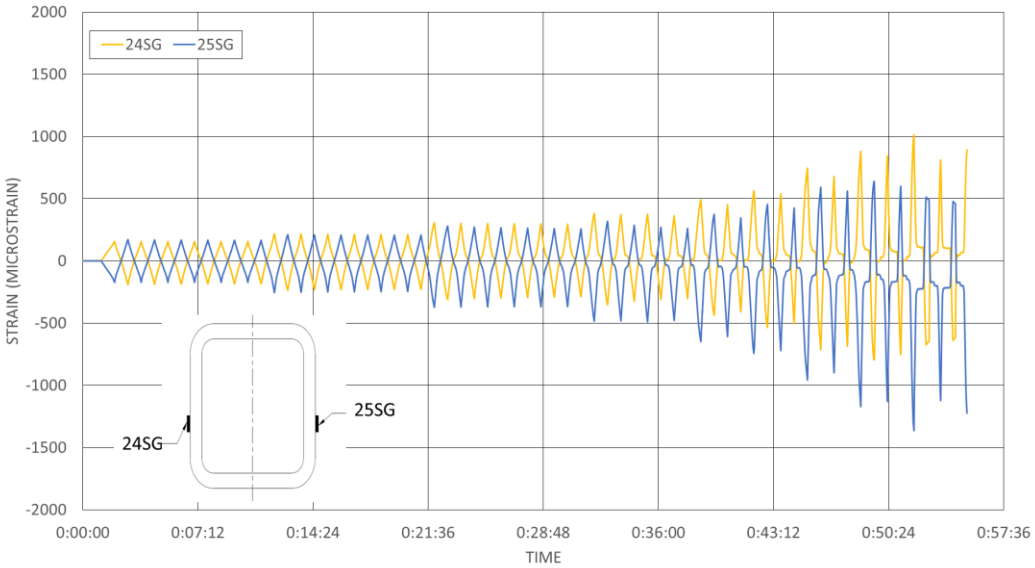

FIGURE 4.15: STRAIN DATA OF C3NW BOTTOM SENSORS (C3NW)

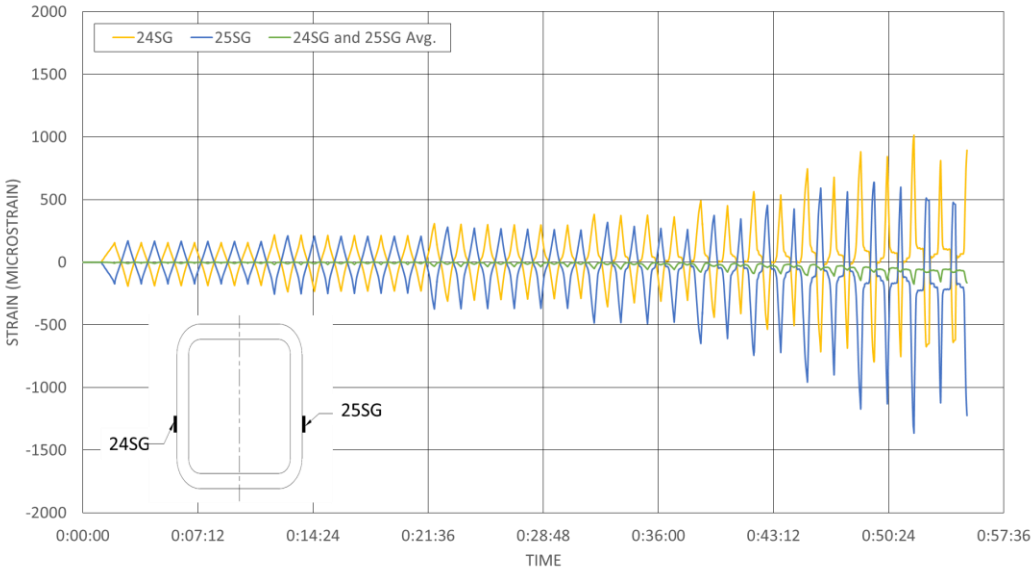

FIGURE 4.16: STRAIN DATA FROM 24SG, 25SG, AND AVERAGE STRAIN (C3NW)

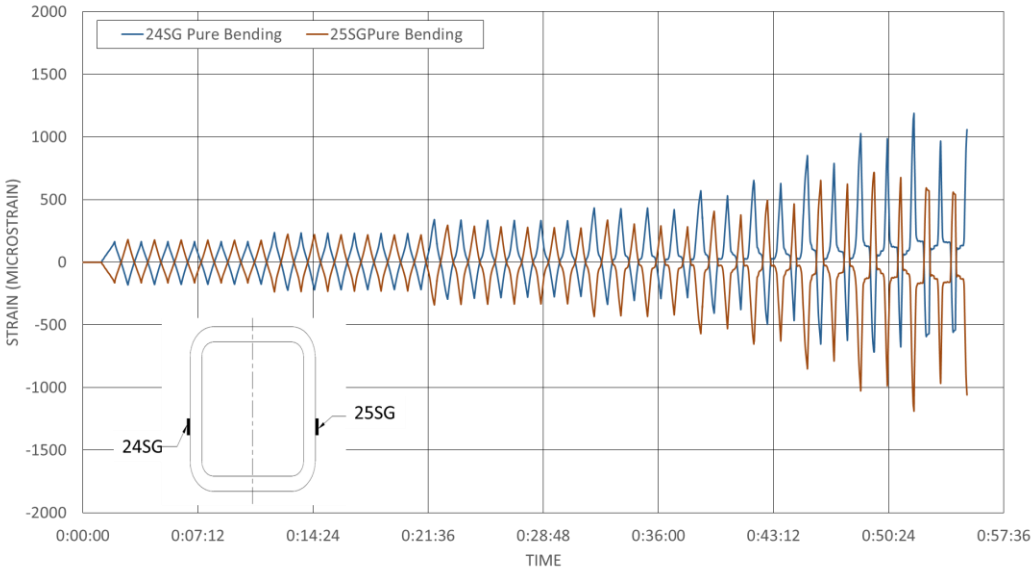

FIGURE 4.17: PURE BENDING STRAIN OF 24SG AND 25SG STRAIN SENSORS

4.4 Interstory Structural Drift

The displacement demands applied to the mezzanine structure are outline in Table 2.1 and Figure 2.17. Experimental testing was done with a specimen that was a complete

structure, therefore different levels of interstory structural drift can be defined using the measured displacements.

The lengths used to define interstory drift are given in Figure 4.18. The 48 inch dimension is from the bottom of the base plate to the actuator centerline. Full is based on the length from the actuator centerline to the level of 41LVDT and 42LVDT. Partial is defined by the length between sensors 28DWT and 26LVDT, and 29DWT and 27DWT. Equation 4.11 through Equation 4.15 illustrate the computation of interstory drift.

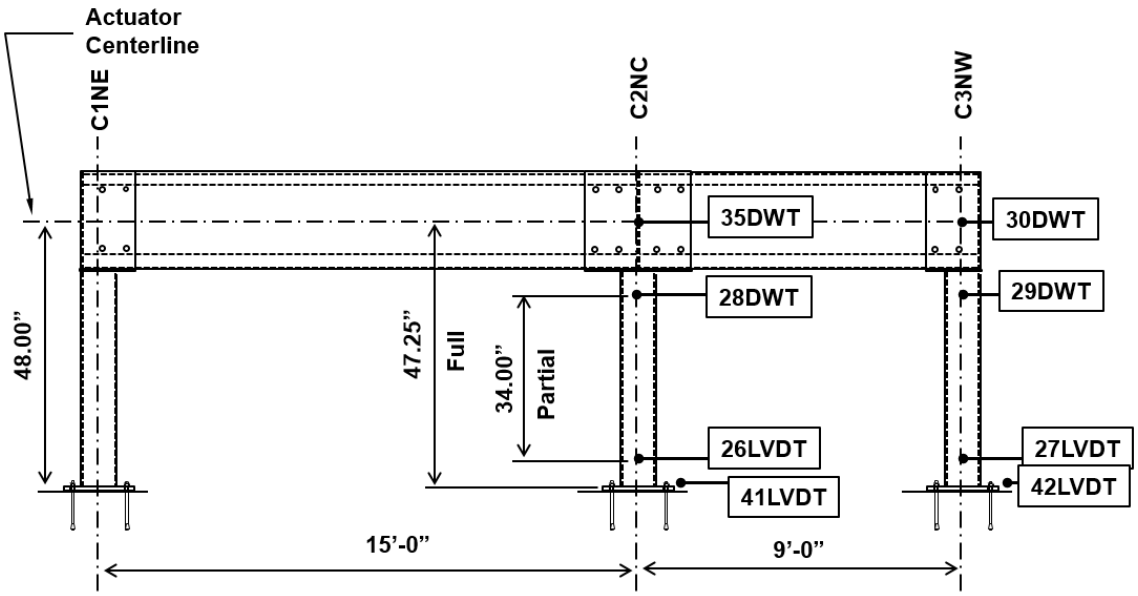

FIGURE 4.18: LENGTHS USED TO DEFINE LEVELS OF INTERSTORY DRIFT

$$\Delta_{Actuator} = \frac{\Delta_{Actuator\ (inches)}}{48\ inches} \quad 4.11$$

$$\Delta_{Full\ (C2NC)} = \frac{\Delta_{35DWT} - \Delta_{41LVDT}}{47.25\ inches} \quad 4.12$$

$$\Delta_{Partial\ (C2NC)} = \frac{\Delta_{28DWT} - \Delta_{26LVDT}}{34\ inches} \quad 4.13$$

$$\Delta_{Full\ (C3NW)} = \frac{\Delta_{30DWT} - \Delta_{42LVDT}}{47.25\ inches} \quad 4.14$$

$$\Delta_{Partial\ (C3NW)} = \frac{\Delta_{29DWT} - \Delta_{27LVDT}}{34\ inches} \quad 4.15$$

The hysteretic response of the mezzanine structure is shown in Figure 4.19. The interstory drift in this figure is defined using the 48 inch length and Equation 4.11. The limitation of the actuator pull capacity can also be seen on Figure 4.19. It should be noted that negative rotations correspond to actuator push strokes. The hysteretic response includes interstory drift demands in the range of 4 to 5 percent.

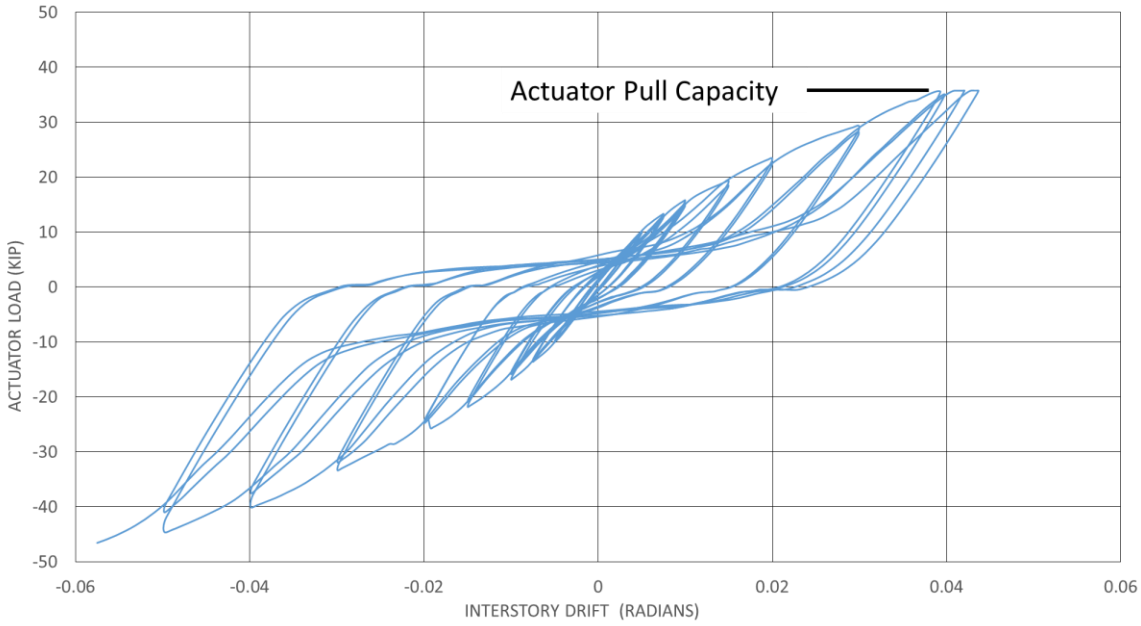

FIGURE 4.19: LOAD DISPLACEMENT CURVE OF MEZZANINE STRUCTURE

The presence of base plate slip demand forces the alternate definition of interstory drift using Equation 4.12 through Equation 4.15. Figure 4.20 illustrates the difference in drift for column C2NC using the "full" and "partial" lengths. Figure 4.21 illustrates the drift demands for column C3NW using the three potential definitions of interstory drift.

Figure 4.20 and Figure 4.21 indicate that base plate slip is significant and does affect the interstory drift demand on the columns. They also indicate that the expected interstory drift demand defined using the actuator displacement alone will yield incorrect estimates of interstory drift. The interstory drift demand defined as “full” and “partial” are similar to one another and include base plate slip.

The hysteretic response of column C2NC and C3NW are shown in Figure 4.22 and Figure 4.23, repectively. The hysteretic response is plotted with respect to the actuator load. The column shear is a function of the actuator load but was not computed here. The hysteretic behavior shown in Figure 4.22 and Figure 4.23 indicates that the target interstory drift demands were not met due to the base plate slip. The pinched shape seen in the hysteretic response is indicative of slip or sliding occurring in the test.

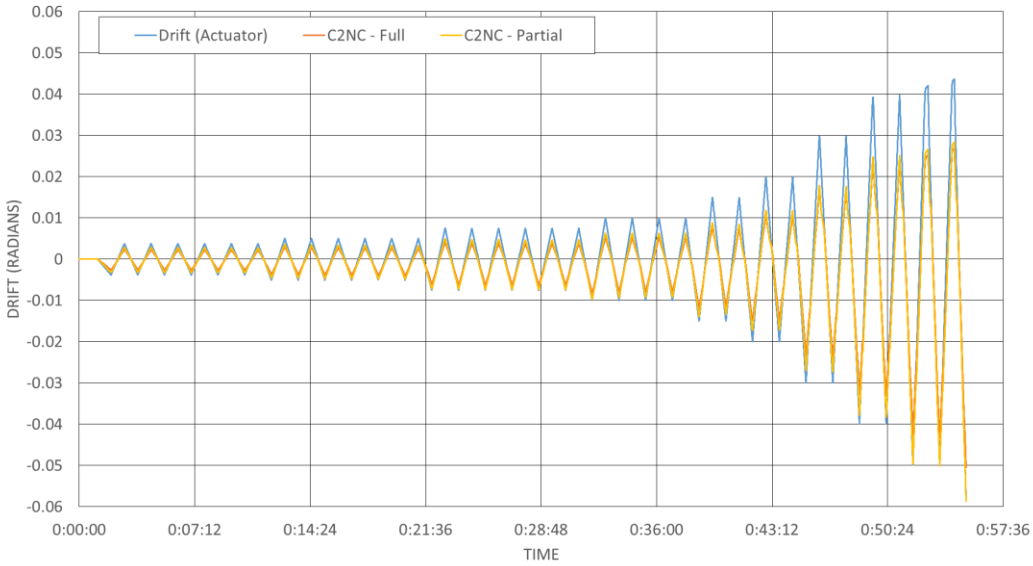

FIGURE 4.20: INTERSTORY DRIFT FOR COLUMN C2NC

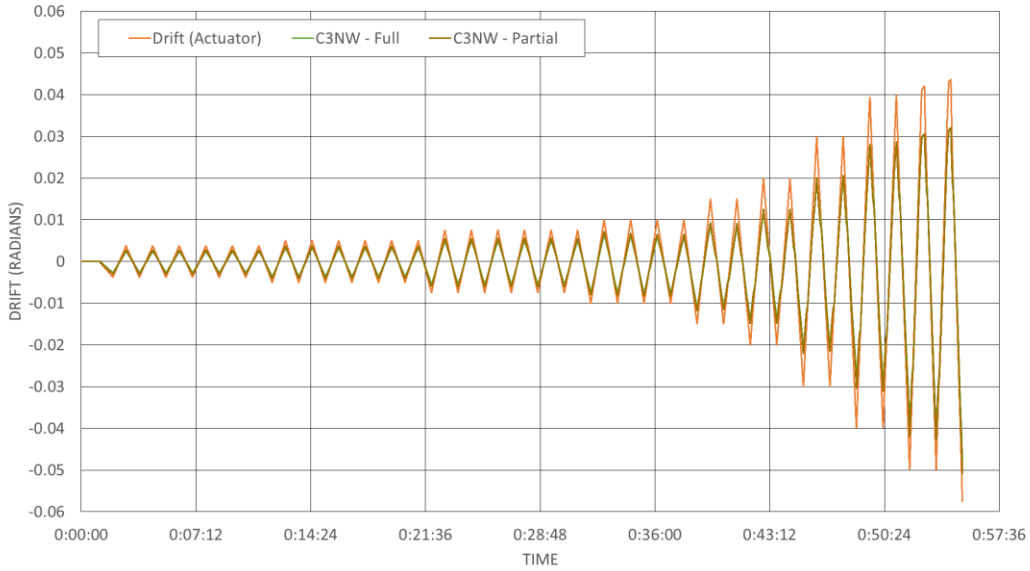

FIGURE 4.21: INTERSTORY DRIFT FOR COLUMN C3NW

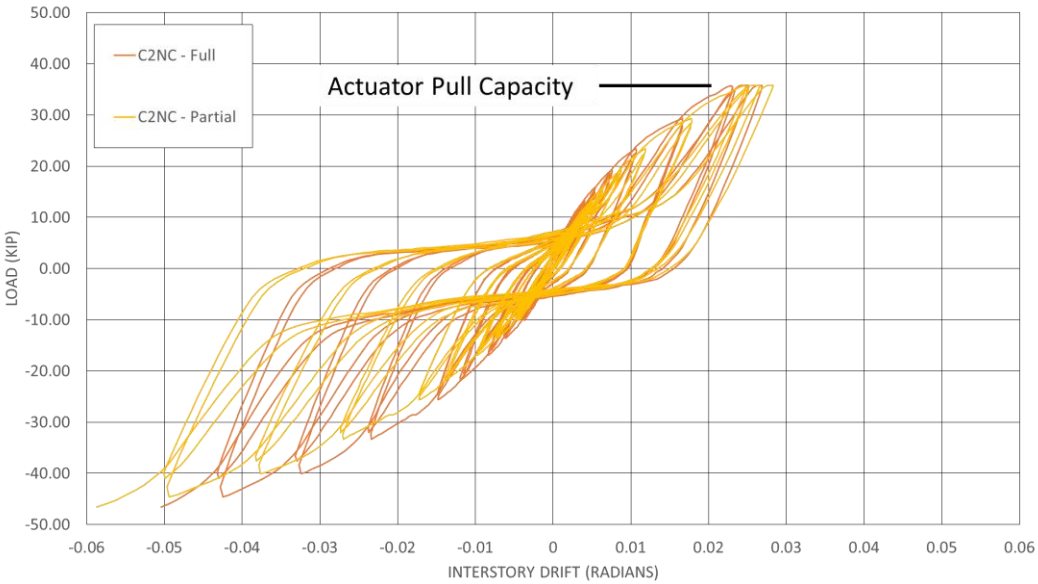

FIGURE 4.22: INTERSTORY DRIFT VS. ACTUATOR LOAD FOR COLUMN C2NC

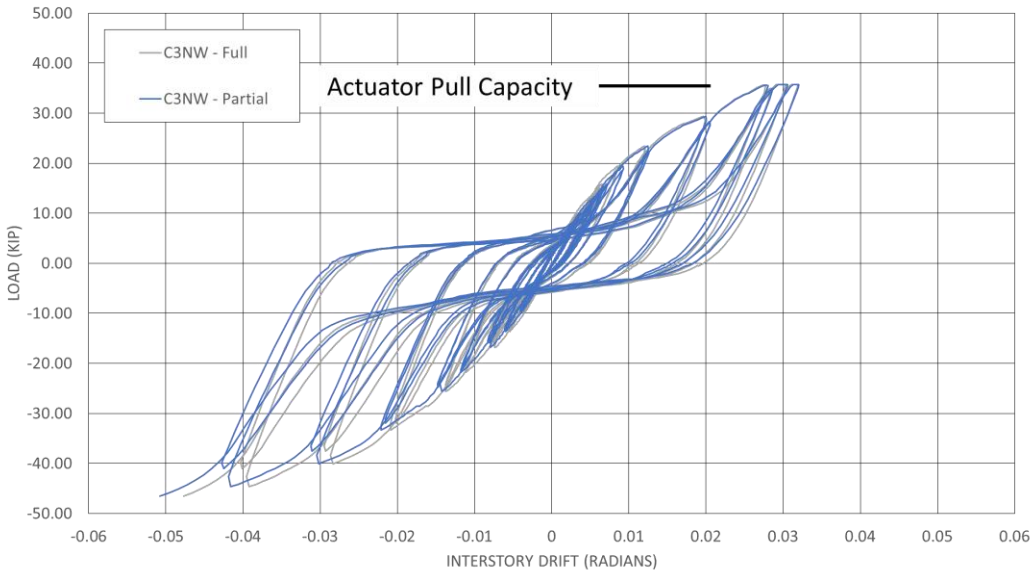

FIGURE 4.23: INTERSTORY DRIFT VS. ACTUATOR LOAD FOR COLUMN C3NW

4.5 General Observations of Mezzanine Structural Test

This section highlights the post-test damage assessment. Figure 4.24 through Figure 4.29 indicate the damaged state of each of the structural columns and their components following testing.

From the top of the structure, the main damage noticed in the following photos is deformation around the bolt holes connecting the channel beams to the HSS column cap plates indicated in Figure 4.28 (A and B). Deformation at bolt holes is a large problem for cold-formed steel structures due to thinness of the connected material. Also at the tops of the columns and moment connections a large amount of bending of the column cap plates was observed noted in Figure 4.25 (F) and Figure 4.28 (H). The column top plate did not contain any strain measuring equipment during structural testing but it is clear that plastic deformation of the cap plates did occur. Thickening the connection plate or mounting the channels directly to the HSS tubes may increase the capacity of this connection but could

also reduce the amount of available interstory drift of the connection. Other damage at the column top included weld fracturing of the welds connecting the column cap plate to the HSS column. Fracture of the welds on the column tops is of particular interest for this type of moment-resisting connection. Typical moment-resisting connections try to avoid fracturing welds if possible and create yielding in the connecting members or ductility in the bolts. This is indicated in Figure 4.24 (F), Figure 4.25 (A and G), Figure 4.27 (B), Figure 4.28 (G), and Figure 4.29 (E and F). Although the welds at the top of the columns had fracturing, the HSS column as a whole had no observable damage. The base of the columns also had a significant amount of damage upon the conclusion of structual testing. Although yielding was very small and difficult to observe in the photographs, bending of the structural base plates did occur. Other damage at the base of the columns included yielding of the anchor rods causing movement of the base plates Figure 4.24 (B and D), Figure 4.25 (B and C), Figure 4.26 (B and C), Figure 4.27 (C and D), Figure 4.28 (C, D, and E), and Figure 4.29 (B and C). Concrete cone failure around the anchor rods also occurred at almost all of the columns indicated in Figure 4.24 (C), Figure 4.25 (D), Figure 4.27 (E), and Figure 4.28 (F), and Figure 4.29 (D). Damage to the anchor rods and the bearing concrete under the base plates of the structure is of particular concern for this structure. A complete failure of two of the anchor rods at Figure 4.27(C, D, and E) was also observed.

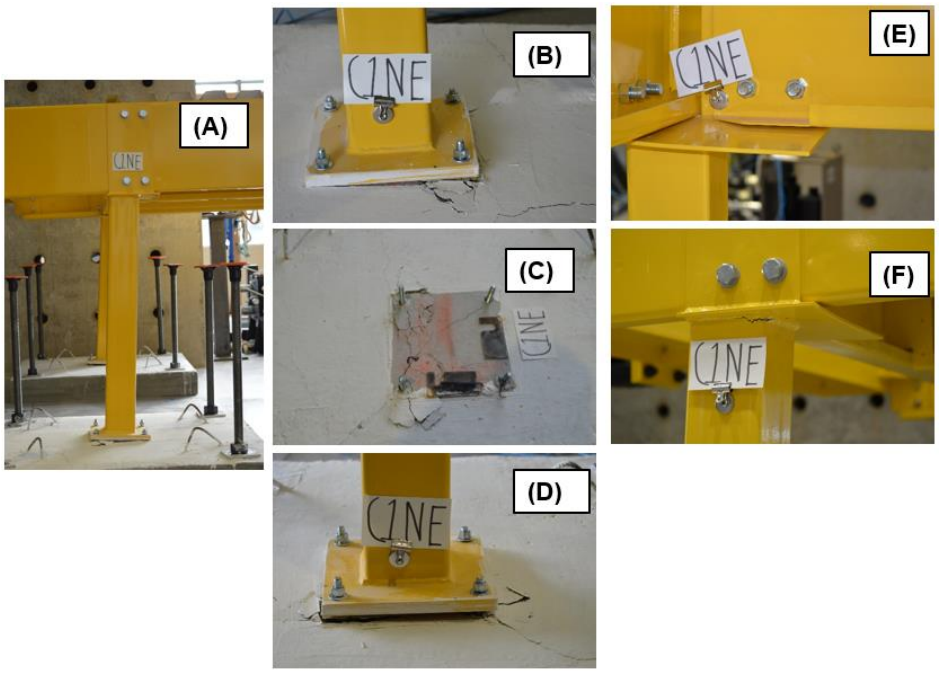

FIGURE 4.24: POST-TEST VIEWS OF COLUMN C1NE

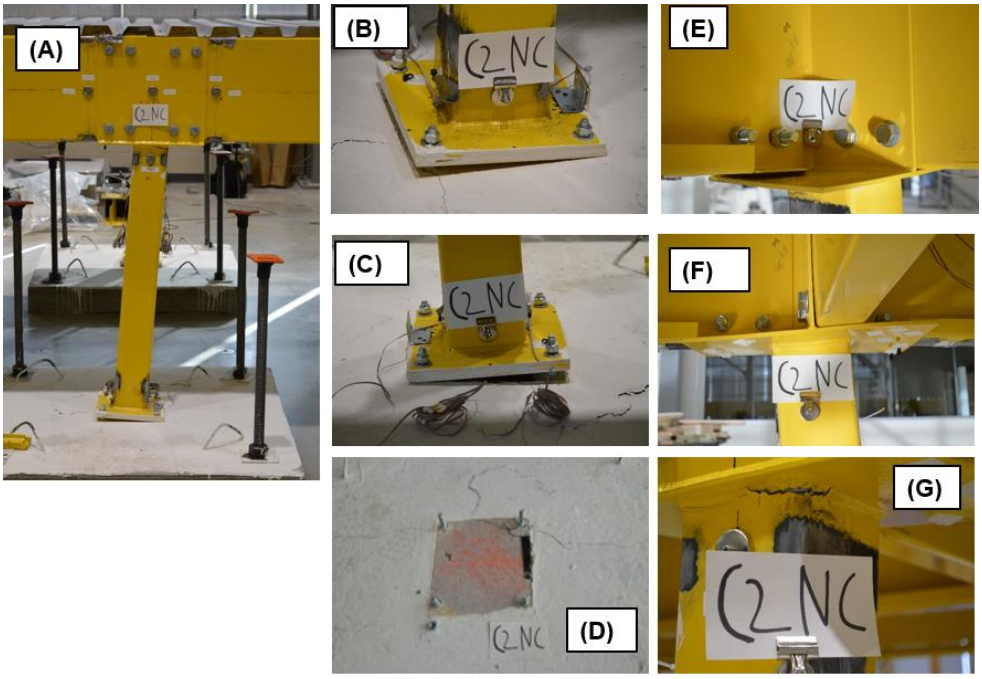

FIGURE 4.25: POST-TEST VIEWS OF COLUMN C2NC

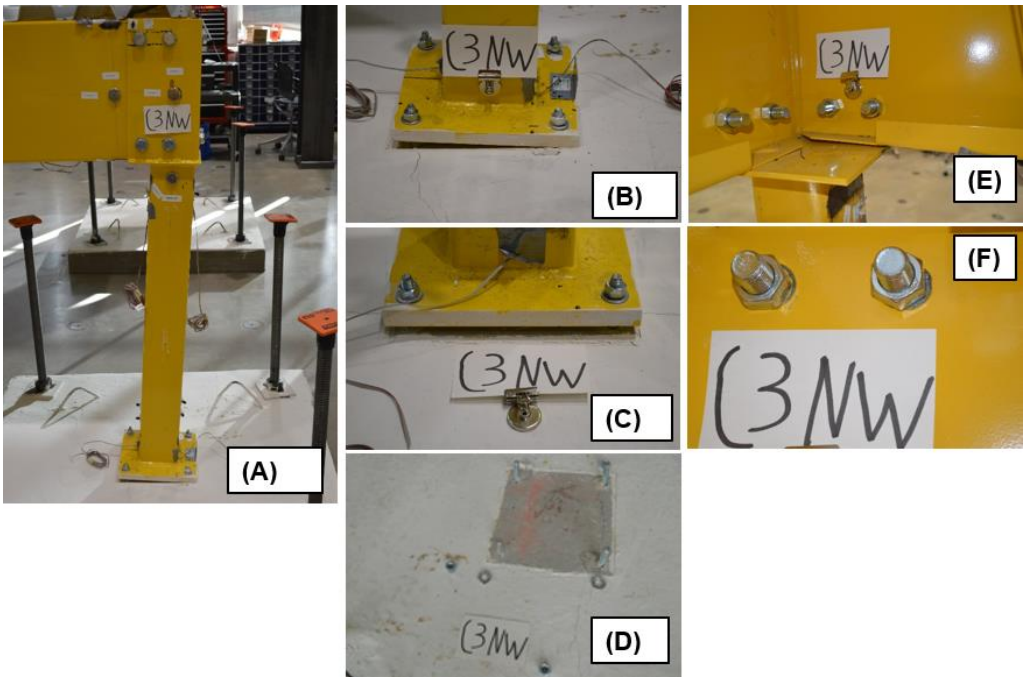

FIGURE 4.26: POST-TEST VIEWS OF COLUMN C3NW

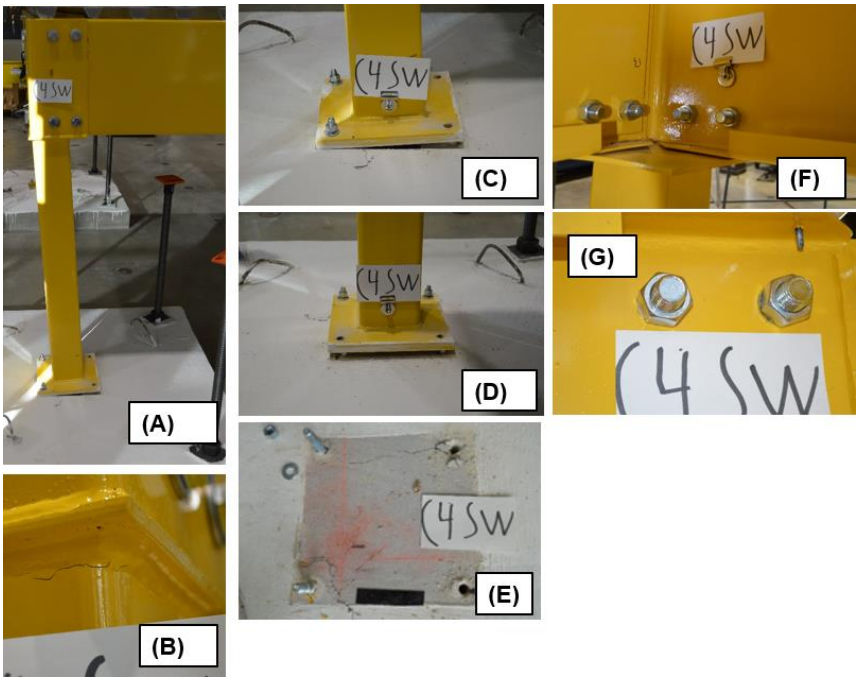

FIGURE 4.27: POST-TEST VIEWS OF COLUMN C4SW

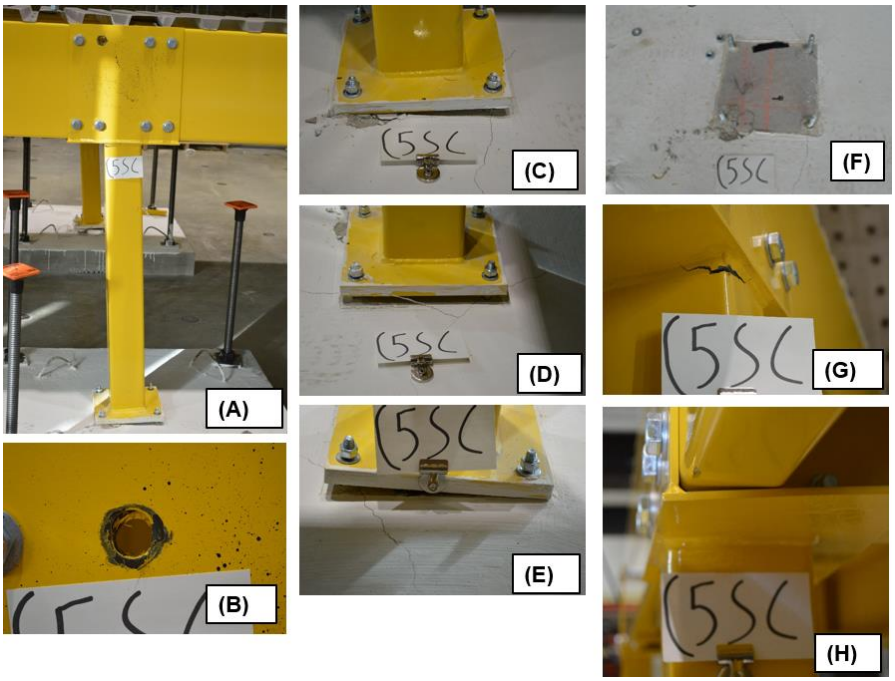

FIGURE 4.28: POST-TEST VIEWS OF COLUMN C5SC

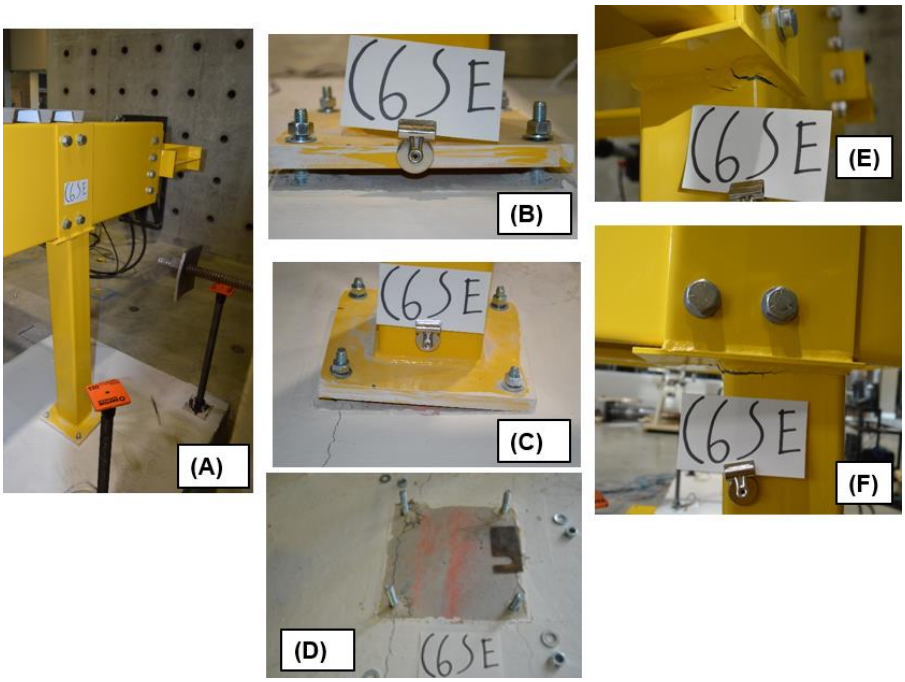

FIGURE 4.29: POST-TEST VIEWS OF COLUMN C6SE

CHAPTER 5 - HSS BASE PLATE MOMENT-ROTATION CURVES

5.1 Introduction

Experimental moment-rotation curves allow for the strength and stiffness of a moment-resisting connection to be modeled. Hysteretic moment-rotation response indicates a measure of energy dissipation capacity for a moment-resisting connection. This chapter uses the strains along with the LVDT displacement measured at the base of the HSS to determine moment and rotation behavior of the connection.

The base plate moment connections at C2NC and C3NW shown in Figure 5.1 were studied in detail. The nominal section properties of plastic section modulus (Z_x) and the plastic moment capacity (M_p) of the HSS column are given in Table 5.1. The material specified was ASTM A500 Grade B Steel for the HSS column. This material has a specified yield stress of 46 ksi. It should be noted that the material strain of the HSS was not exceeded during the extent of structural testing at the column base strain sensors. The modulus of elasticity assumed to convert measured strain to stress is 29,000 ksi.

As defined in Figure 2.6 and Figure 2.7 the base plates are 3/4 inch thickness and 10 inch by 10 inch in length and width respectively. They contain 1/2 inch diameter wedge expansion anchors 1-1/2 inches from the edges of the plate.

TABLE 5.1: NOMINAL SECTION PROPERTIES OF HSS SHAPE (COLUMN)

	Z_X (inches^3)	M_p (kip-feet), F_y = 46 ksi
HSS5X5X3/16	5.89	22.58

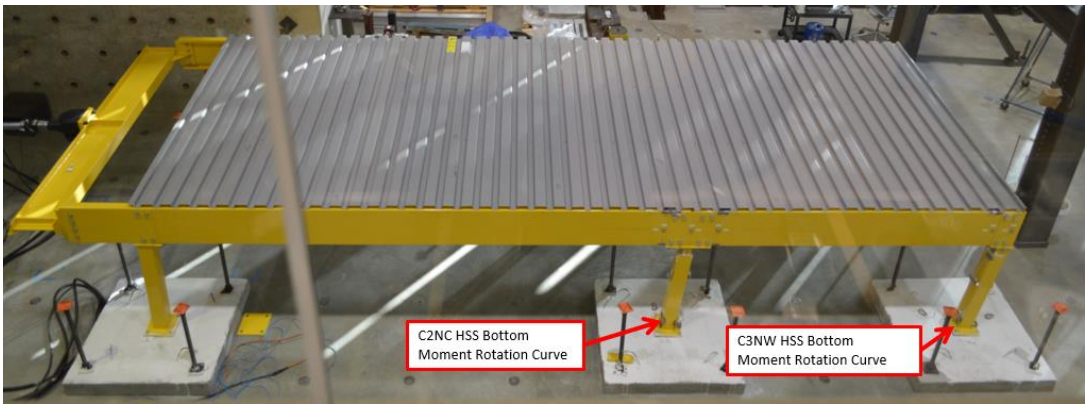

FIGURE 5.1: LOCATION OF HSS BASE CONNECTION HYSTERETIC RESPONSE

The pure bending strains measured at sensors 19SG and 24SG, and 20SG and 25SG (Figure 4.14 and Figure 4.17) are used in conjunction with the discretization of the HSS cross-section to compute the bending moments. Elementary mechanics for bending strain are assumed for the distributions of strain to the discretized sections using the distribution below the HSS shape in Figure 5.2. Y-bar is the equivalent to the distance from the neutral Y-Y axis to the centroid of the cross-section. The strain value in each section is assumed to be uniform and based on the value of strain at the center of the section. The strain values from the gauges are considered equal for the five sections on the tube wall of which the strain gauge is placed. The strain is then assumed to be linear over the HSS height based on y-bar. Equation 5.1 is used to calculate moment from the strain value in each section.

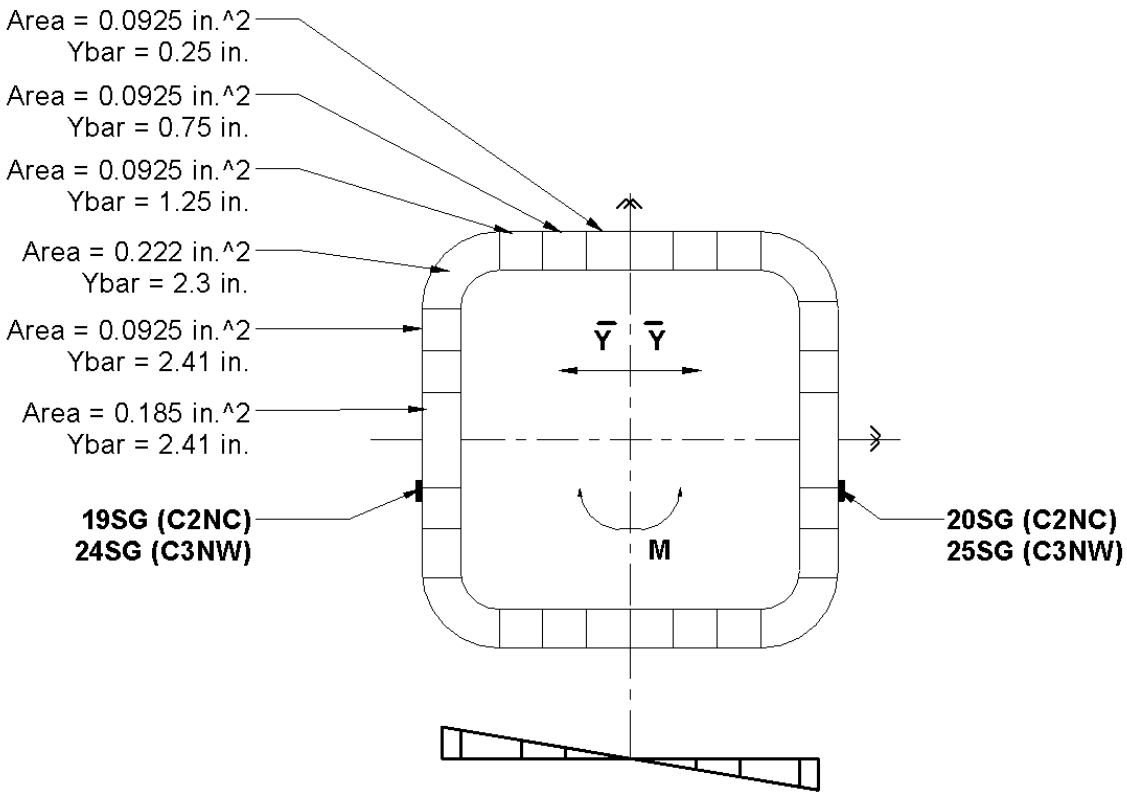

FIGURE 5.2: DISCRETIZATION OF C2NC CROSS-SECTION FOR MOMENT-ROTATION CURVE

$$M = \sum_{i=1}^{N} E\epsilon_i A_i \bar{y}_i \qquad 5.1$$

5.2 C2NC Base Plate Moment-Rotation Hysteretic Behavior

Complete moment-rotation behavior is displayed in Figure 5.3 and Figure 5.4 for C2NC. These figures show moment in kip-feet and moment normalized for the plastic moment capacity. A plot indicating the amount of positive and negative rotation for each load cycle is displayed in Figure 5.5. The rotations used to create these moment-rotation curves are given in Chapter 4. The moment-rotation curves show stable hysteretic moment-rotation response out to 0.03 radians of rotational demand at 40 percent of the

plastic moment capacity of the section. Pinched hysteretic behavior illustrates limited energy dissipation capacity.

Moments applied to the structure during load cycle number 1 (Figure 2.17) indicated in Figure 5.6 display that initial loading of the structure indicates unequal stiffness in opposite directions. It can be noticed in this plot that the displacements at the base of the structure are unequal as indicated by the LVDT in Figure 4.9. Similarly, rotations in Figure 4.11 indicate a move off the x-axis at the first cycle. The plot of strains on the bottom of column C2NC in Figure 5.7 taken from Figure 4.14 indicates a slight difference in strain at the positive and negative loading cycles contributing to the difference in positive and negative moment in Figure 5.6.

Load cycle number 6 is indicated in Figure 5.8. This figure indicates an increased level of resistance in the base plate. The hysteretic response indicates the anchor rods are pulling out of the holes. Note that the hardening stiffness appears to be similar in both directions as indicated by the slope of the lines during the increase of moment outside of the rotations contributed by base plate slip.

By the start of load cycle number 8, Figure 5.9, a backbone curve emerges which continues through the remainder of structural testing. This curve continues to indicate the difference in moment during positive and negative displacement values owing to the difference in strains indicated in Figure 4.14 but continues to indicate equal hardening stiffness in both directions.

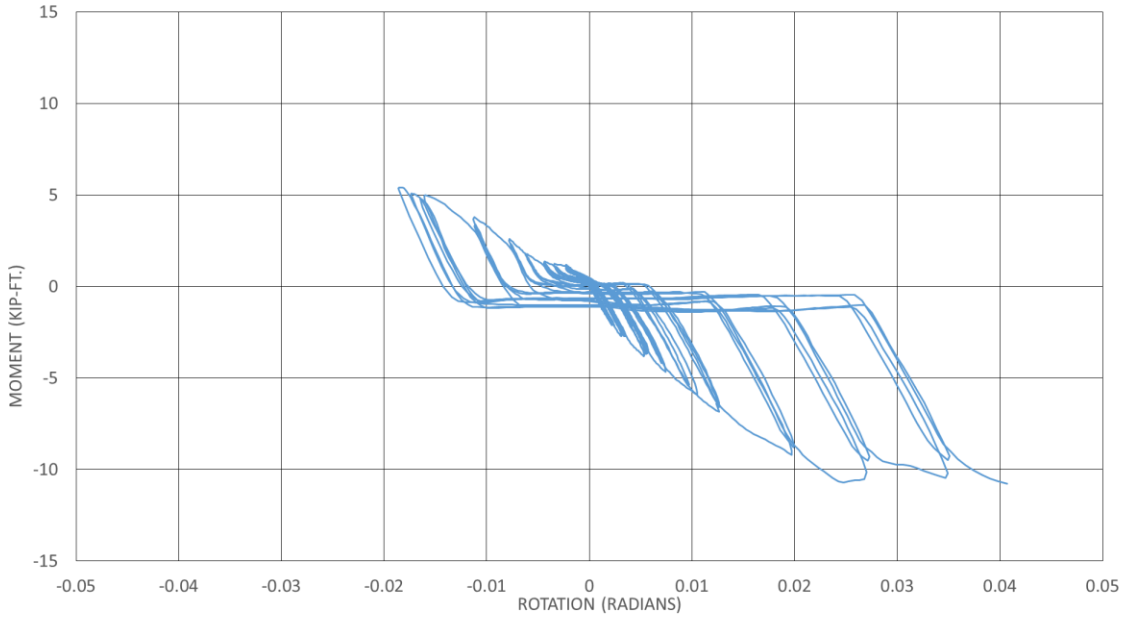

FIGURE 5.3: C2NC BASE CONNECTION HYSTERETIC MOMENT-ROTATION RESPONSE

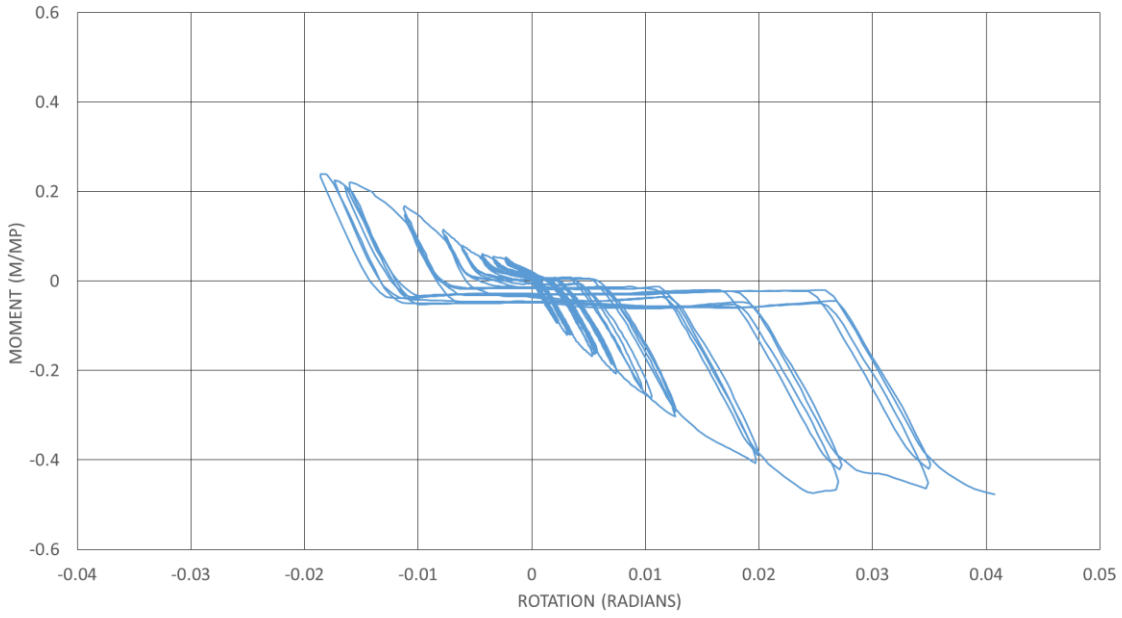

FIGURE 5.4: C2NC BASE CONNECTION HYSTERETIC MOMENT-ROTATION RESPONSE (F_Y = 46 KSI)

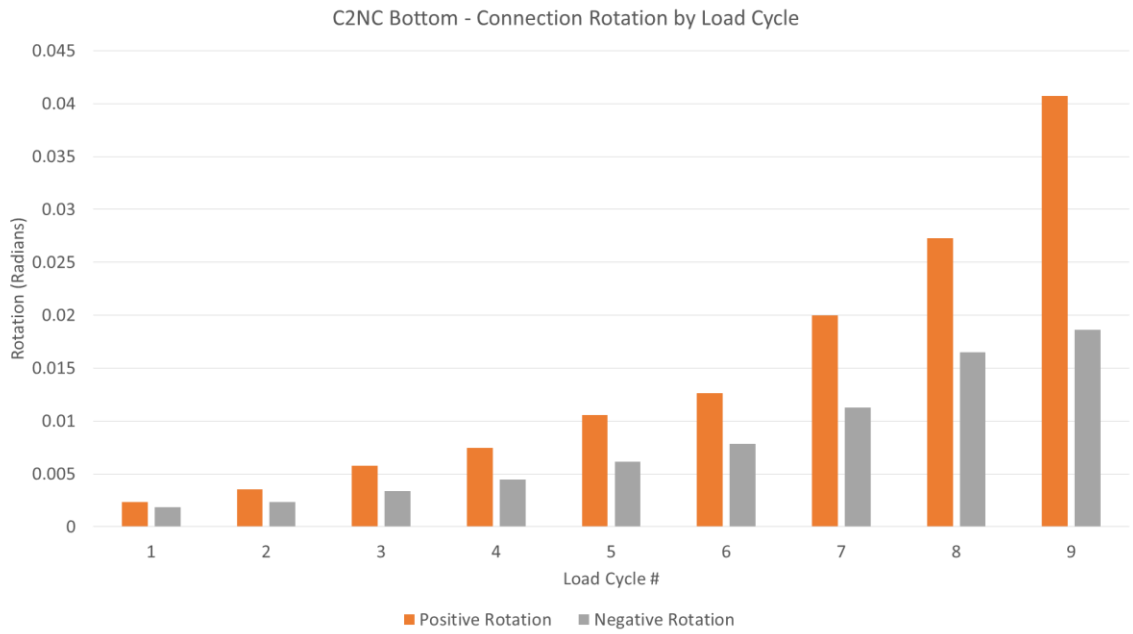

FIGURE 5.5: C2NC BASE PLATE, CONNECTION ROTATION

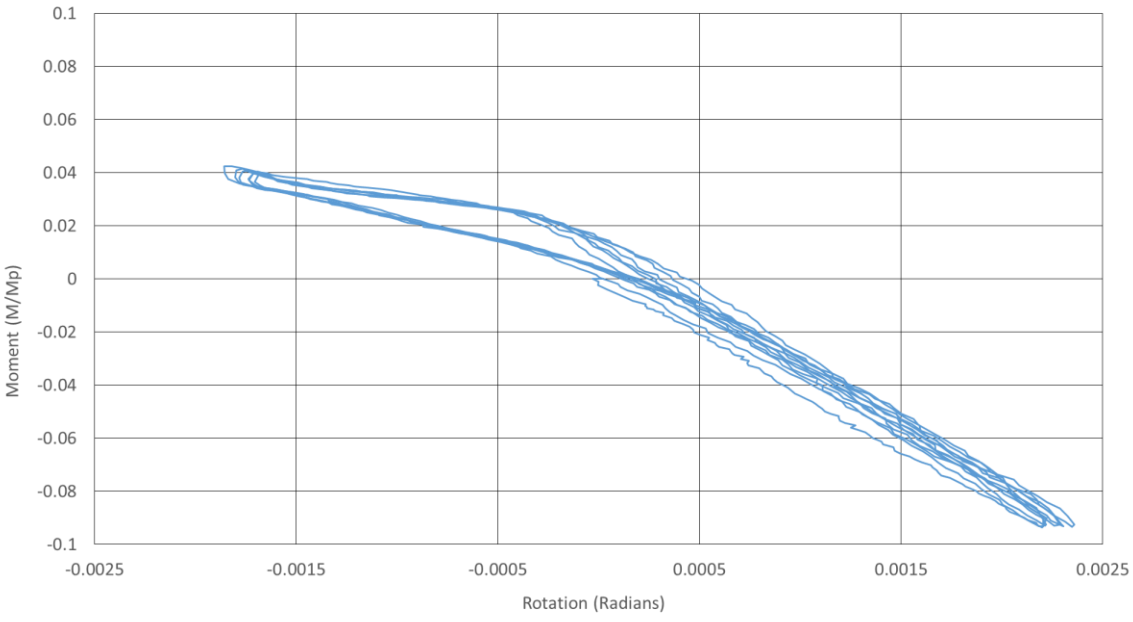

FIGURE 5.6: C2NC BASE CONNECTION HYSTERETIC MOMENT-ROTATION RESPONSE, LOAD CYCLE 1

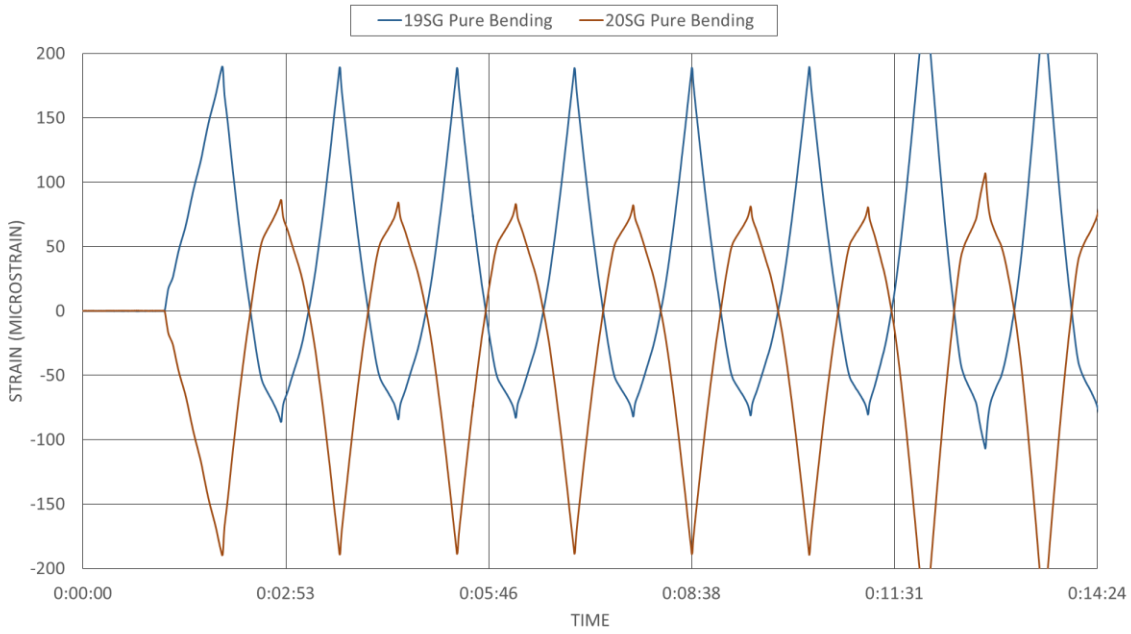

FIGURE 5.7: PURE BENDING STRAINS, COLUMN C2NC

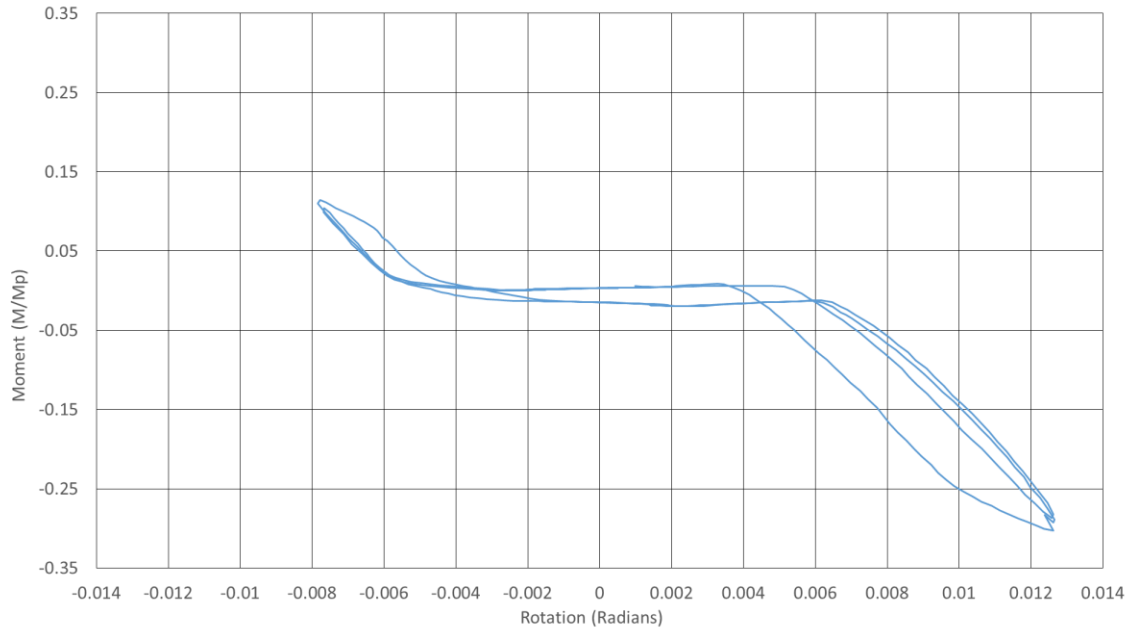

FIGURE 5.8: C2NC BASE CONNECTION HYSTERETIC MOMENT-ROTATION RESPONSE, LOAD CYCLE 6

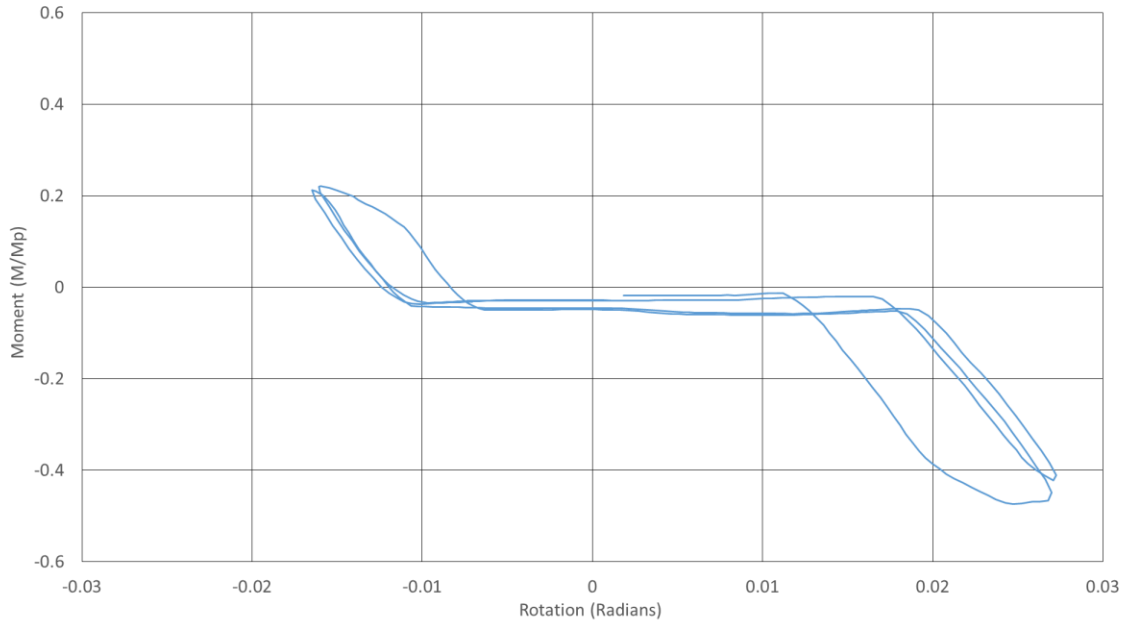

FIGURE 5.9: C2NC BASE CONNECTION HYSTERETIC MOMENT-ROTATION RESPONSE, LOAD CYCLE 8

5.3 C3NW Base Plate Moment-Rotation Hysteretic Behavior

Complete moment-rotation behavior is displayed in Figure 5.10 and Figure 5.11. These figures show moment in kip-feet and moment normalized for the plastic moment capacity. A plot indicating the amount of positive and negative rotation for each load cycle is displayed in Figure 5.12. The hysteretic response indicates anchor rod pull-out.

Moments applied to the structure during load cycle number 1 (Figure 2.17) indicated in Figure 5.13 show that initial loading of the structure occurs through free movement of the structure without components of the structure coming into bearing. Unequal stiffness is observed in load cycle number 3 indicated in Figure 5.14. This load cycle has very similar characteristics to load cycle number 1 with respect to displacement and strain with only a slight hint of increasing resistance noted from the changing slopes in the graph. Evidence of base plate bending, anchor rod stretching and anchor pull-out is evident. The plot of strains on the bottom of column C2NC in Figure 5.15, taken from

Figure 4.17, indicates a slight difference in strain at the positive and negative loading cycles contributing to the slight difference in positive and negative moment seen throughout testing.

Load cycle number 6 indicated in Figure 5.16 indicates a substantial amount of free sliding of over 0.02 radians in the connection before bearing occurs, allowing for substantial increases in moment resistance. Figure 5.16 also indicates a slip in the connection at 0.005 radians indicating some type of resistance is encountered in the base plate to free motion and a jump to a large rotation indicating a failure.

Load cycle number 7 is shown in Figure 5.17 which shows what could become a typical backbone curve. The larger openings occurring inside the hysteresis during negative rotations indicate resistance from the structure when load is removed by the actuator. Significantly more evidence of anchor rod pull-out is observed.

It is important to note that the rotations remain relatively equal but not completely equal through the conclusion of load cycle 5 indicated in Figure 5.12. The rotations in both load cycle 6 and 7 indicate large unequal displacements continuing for the remainder of testing.

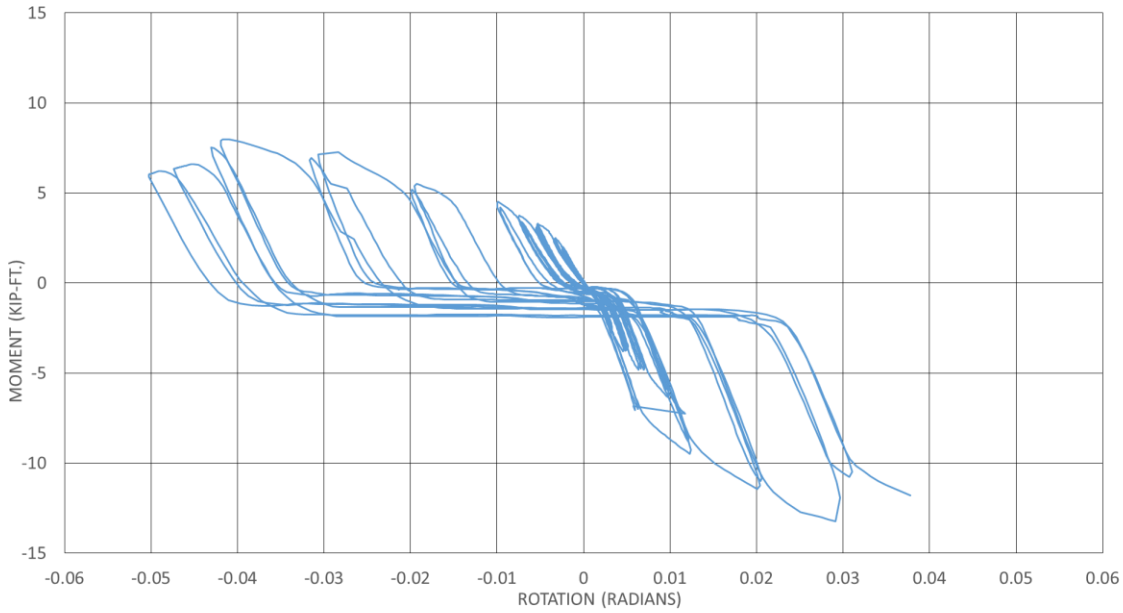

FIGURE 5.10: C3NW BASE CONNECTION HYSTERETIC MOMENT-ROTATION RESPONSE

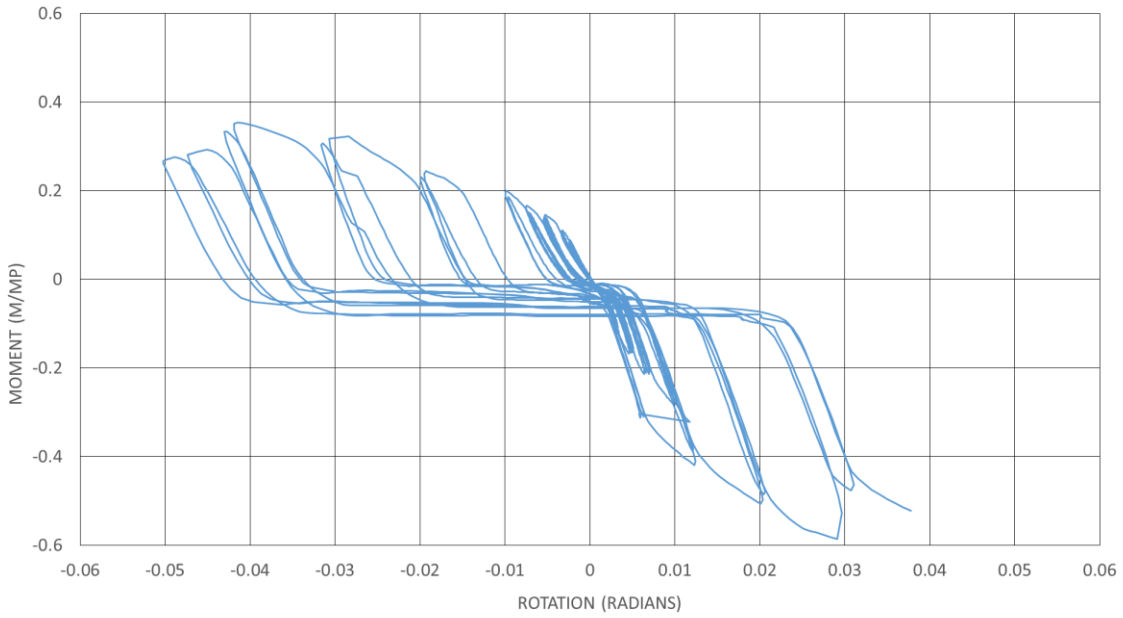

FIGURE 5.11: C3NW BASE CONNECTION HYSTERETIC MOMENT-ROTATION RESPONSE (F_Y = 46 KSI)

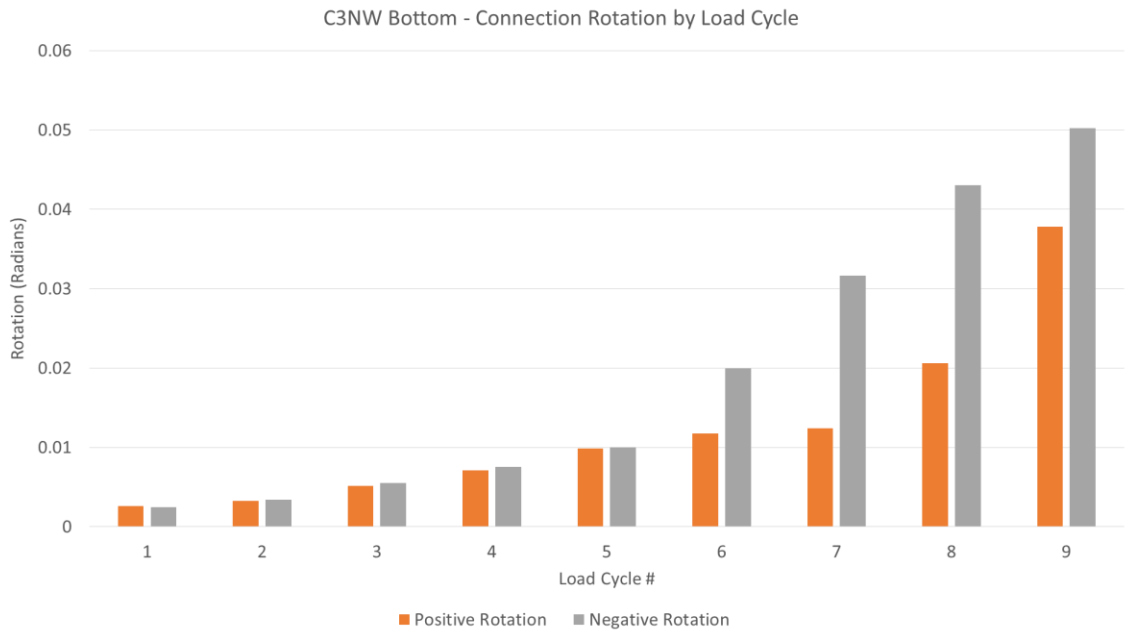

FIGURE 5.12: C3NW BASE PLATE, CONNECTION ROTATION

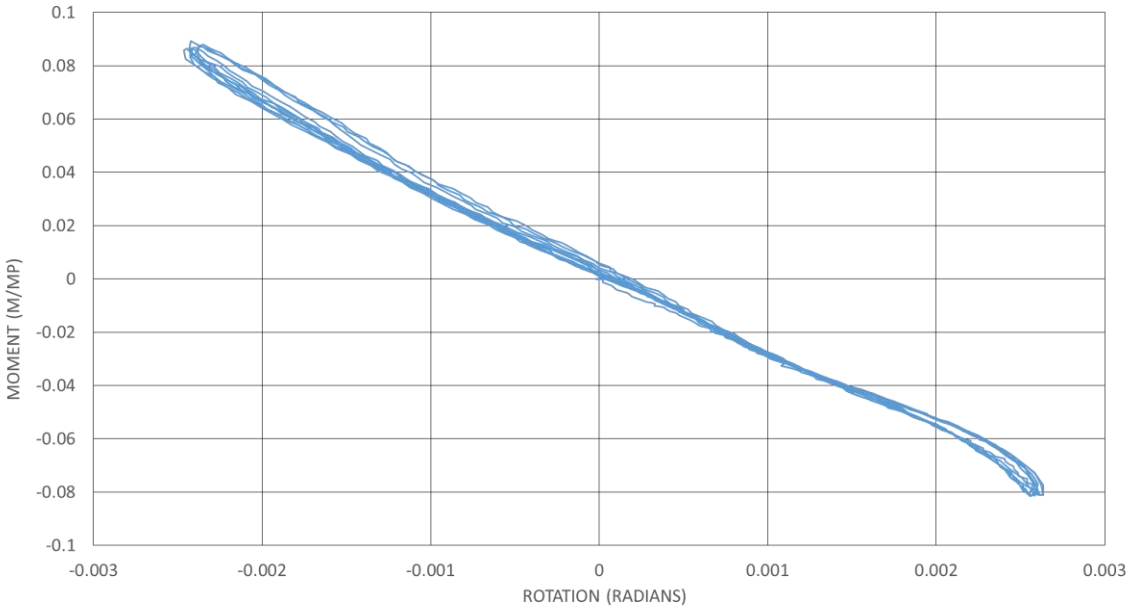

FIGURE 5.13: C3NW BASE CONNECTION HYSTERETIC MOMENT-ROTATION RESPONSE, LOAD CYCLE 1

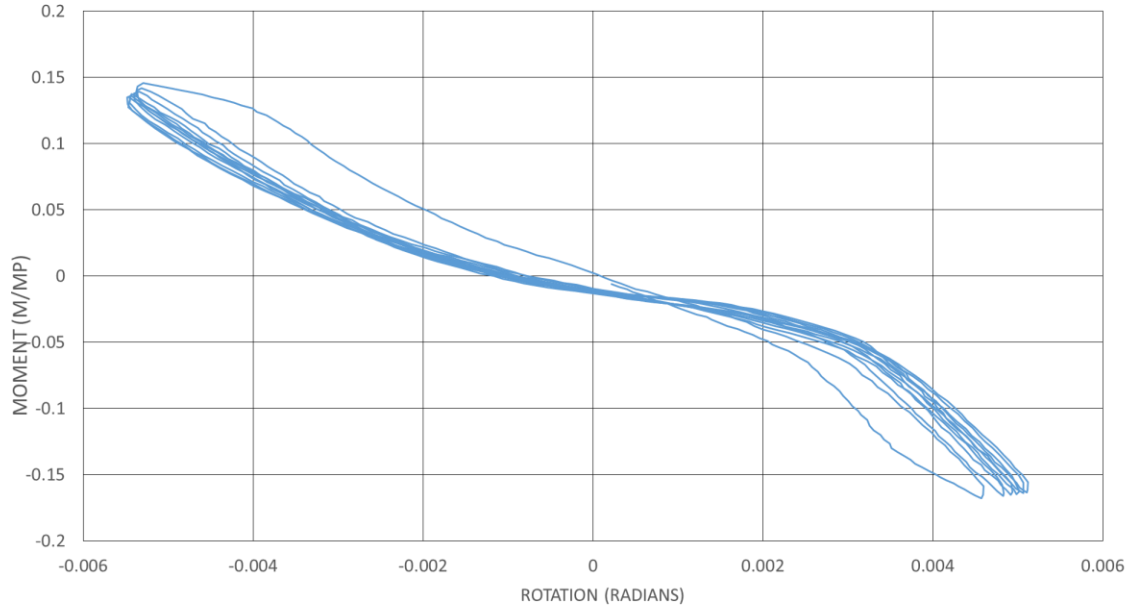

FIGURE 5.14: C3NW BASE CONNECTION HYSTERETIC MOMENT-ROTATION RESPONSE, LOAD CYCLE 3

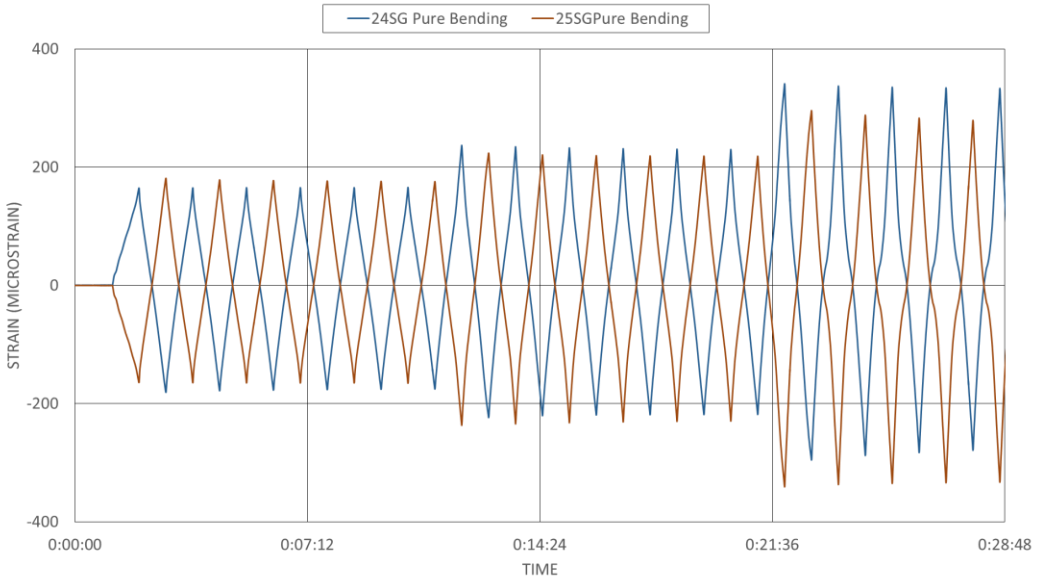

FIGURE 5.15: PURE BENDING STRAINS, COLUMN C3NW

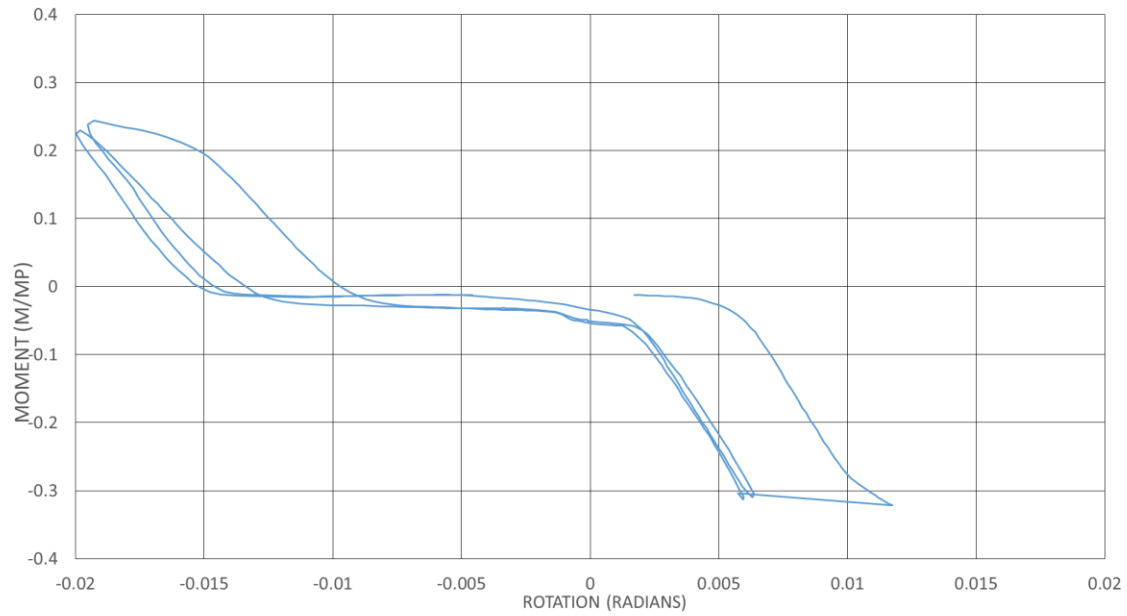

FIGURE 5.16: C3NW BASE CONNECTION HYSTERETIC MOMENT-ROTATION RESPONSE, LOAD CYCLE 6

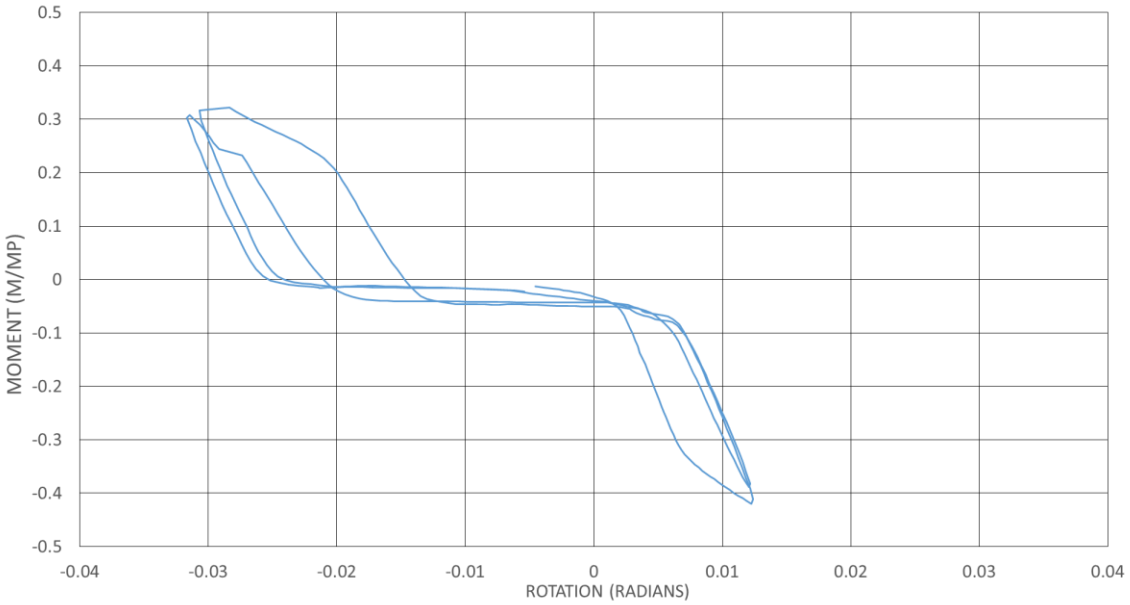

FIGURE 5.17: C3NW BASE CONNECTION HYSTERETIC MOMENT-ROTATION RESPONSE, LOAD CYCLE 7

CHAPTER 6 - HYSTERETIC ANALYSIS OF MEZZANINE

6.1 Introduction

This chapter defines a hysteretic response model of the entire structure. Modelling is presented based on the loading of the mezzanine to 0.04 radians defined by the interstory drift of the actuator presented in Equation 4.11. This includes slip of the base plate. The rotations versus time used in the development of the model are given in Figure 6.1.

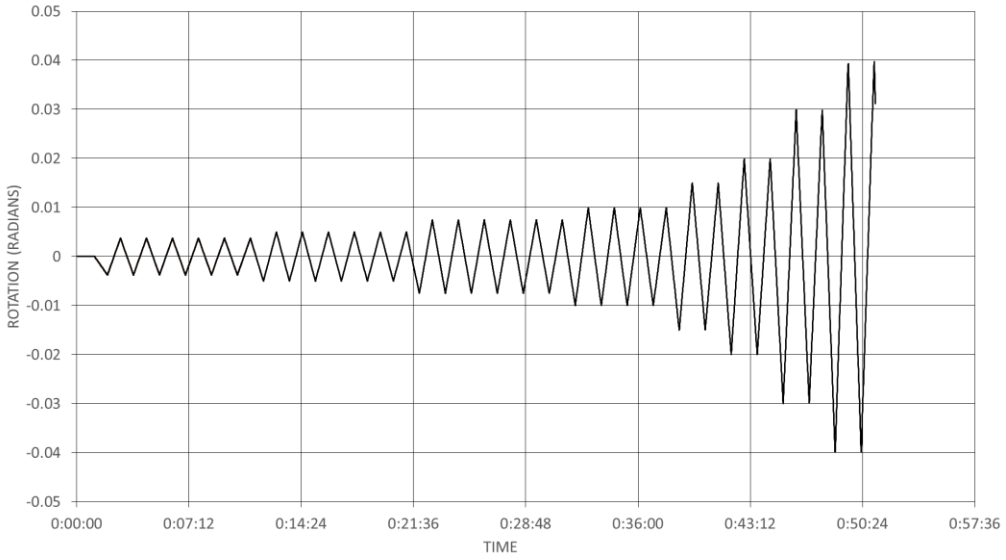

FIGURE 6.1: ROTATION VS. TIME USED FOR HYSTERETIC MODELS

6.2 Characteristics of the Developed Hysteretic Model

This section defines the hysteretic model for the parameters needed to an applied interstory drift demand of 0.04 radians. The full envelope model is displayed in Figure 6.2. Load is normalized based on an actuator load of 12 kips, defined in Equation 6.1.

$$Normalized\ Load = \frac{V_{Actuator\ Load}}{V_y = 12\ kip} \tag{6.1}$$

The hysteretic model for this structure is composed of four separate structural stiffnesses defined in Figure 6.2. An initial stiffness defined by load cycle number 1 shown in Figure 6.3 displays almost no energy dissipation occurring in the structure. A rotation of 0.006 radians is required to exceed the first stiffness. The second stiffness was determined by fitting a linear line to the average of the positive peak load values during each load cycle of the actuator to 0.04 radians of rotation. The structure unloads using the initial structural stiffness until reaching a level of zero applied load. The fourth stiffness of the structure occurs from the level of zero structural load until the structure reaches its initial stiffness determined using the same method for the second structural stiffness.

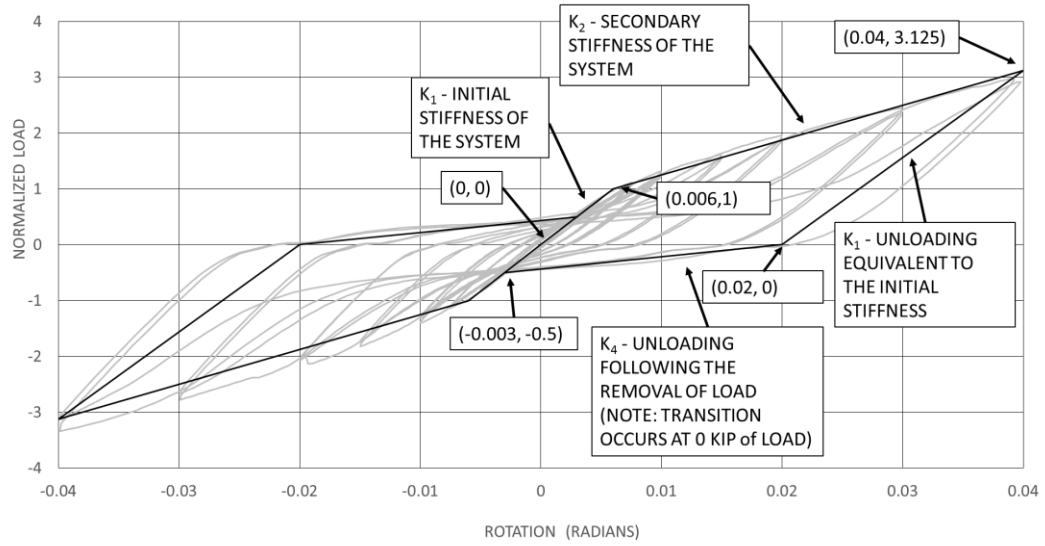

FIGURE 6.2: HYSTERETIC MODEL OF MEZZANINE STRUCTURE

6.3 Hysteretic Models by Load Cycle

The hysteretic model is overlayed onto each loading cycle shown in Figure 6.3 to Figure 6.10. A small plot of Figure 6.1 is given on each figure for reference to the corresponding load cycle given in Figure 2.17.

Load cycle number 1 and 2 (Figure 6.3 and Figure 6.4) indicate loading behavior which follows elastic branches as expected. Thus the first two load cycles are essentially elastic behavior. Load cycle number 3 (Figure 6.5) illustrates the first hint of nonlinear response. The pinched hysteresis indicates that sliding at the column bases has begun. Load cycle number 4 (Figure 6.6) indicates increasing magnitudes of nonlinear response. The area enclosed by hysteretic loops indicates energy dissipation is occurring. Load cycle number 5 to 8 (Figure 6.7 to Figure 6.10) indicates some slight variation from the hysteretic model which occurs due to the unequal positive and negative loads. Further hysteretic energy dissipation also occurs and the continued pinched response indicative of sliding, slip at connections, and concrete cracking or crushing is observed. Hysteretic loading remains stable to +/-0.04 radians.

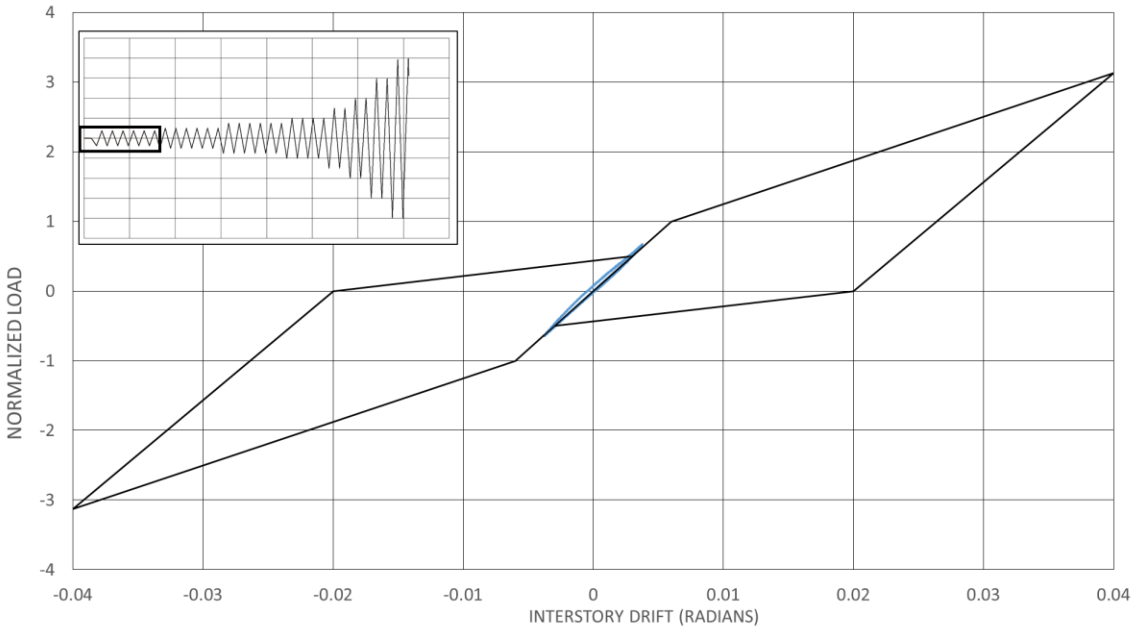

FIGURE 6.3: LOAD CYCLE 1 - HYSTERETIC BEHAVIOR

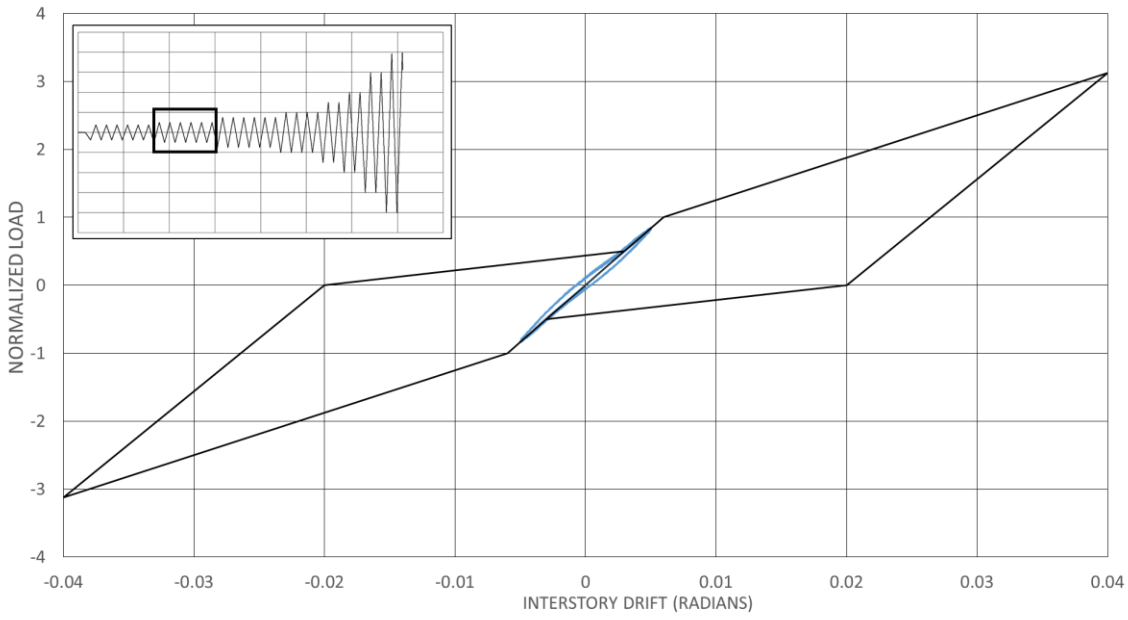

FIGURE 6.4: LOAD CYCLE 2 - HYSTERETIC BEHAVIOR

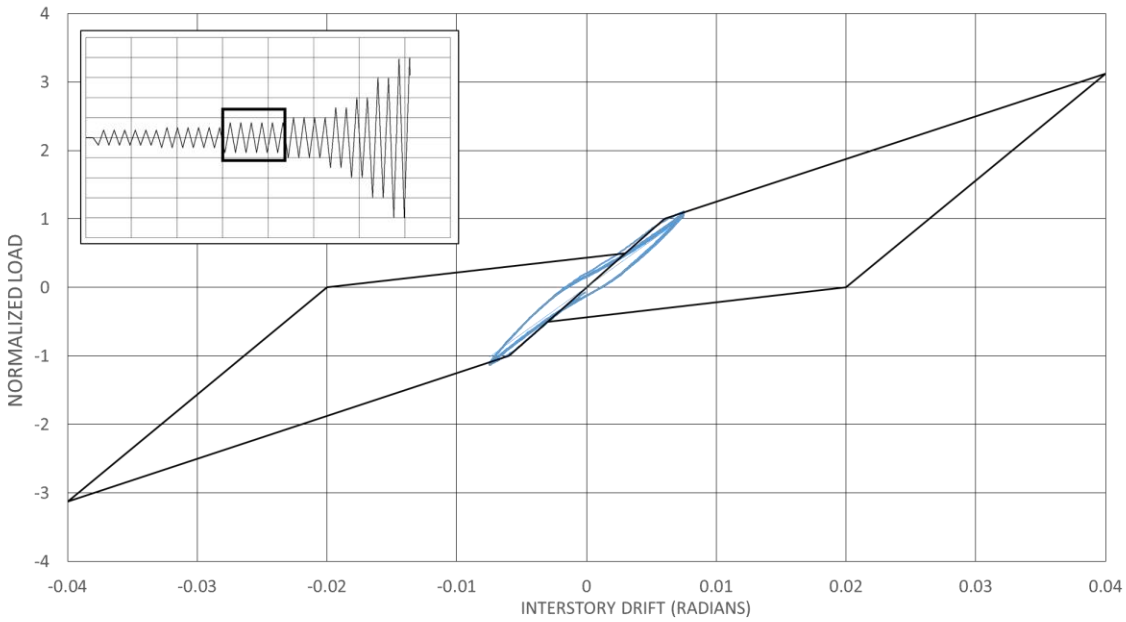

FIGURE 6.5: LOAD CYCLE 3 - HYSTERETIC BEHAVIOR

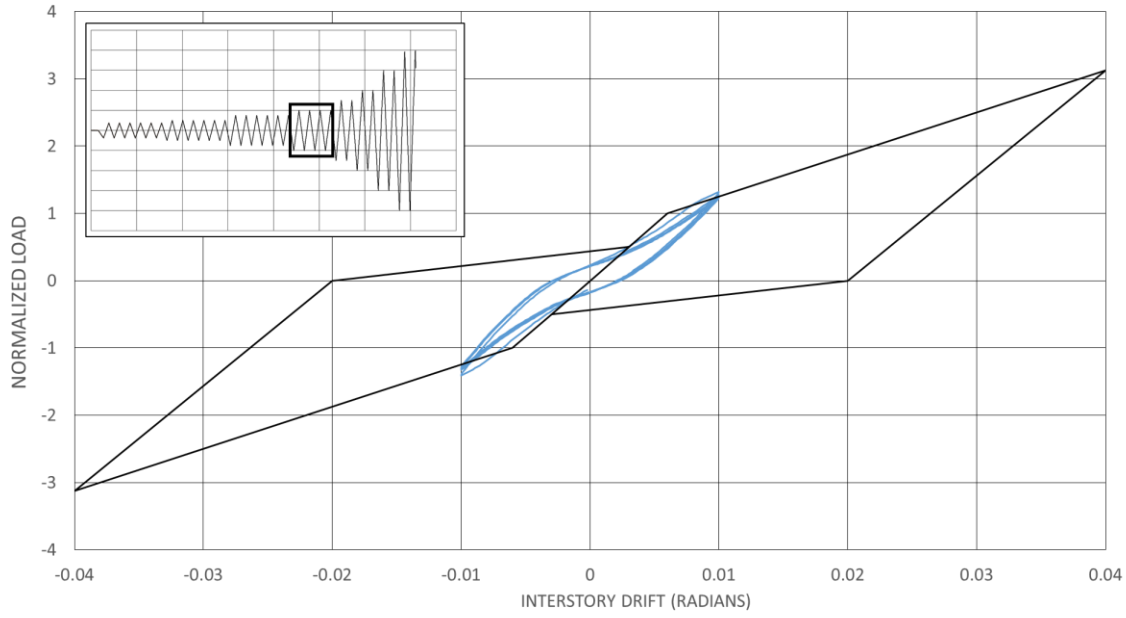

FIGURE 6.6: LOAD CYCLE 4 - HYSTERETIC BEHAVIOR

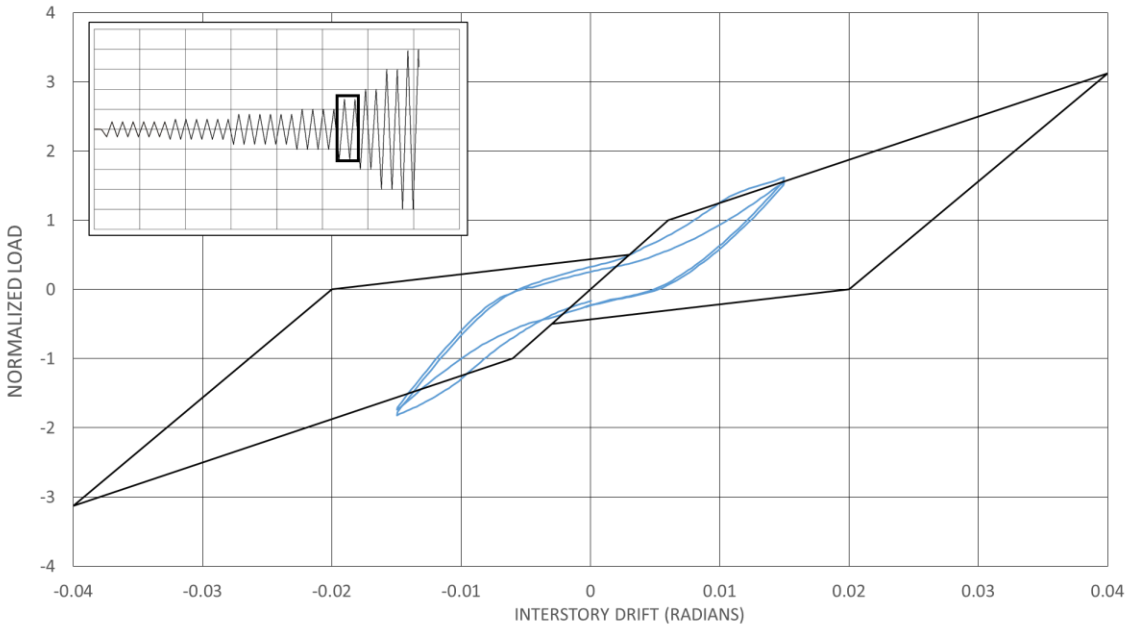

FIGURE 6.7: LOAD CYCLE 5 - HYSTERETIC BEHAVIOR

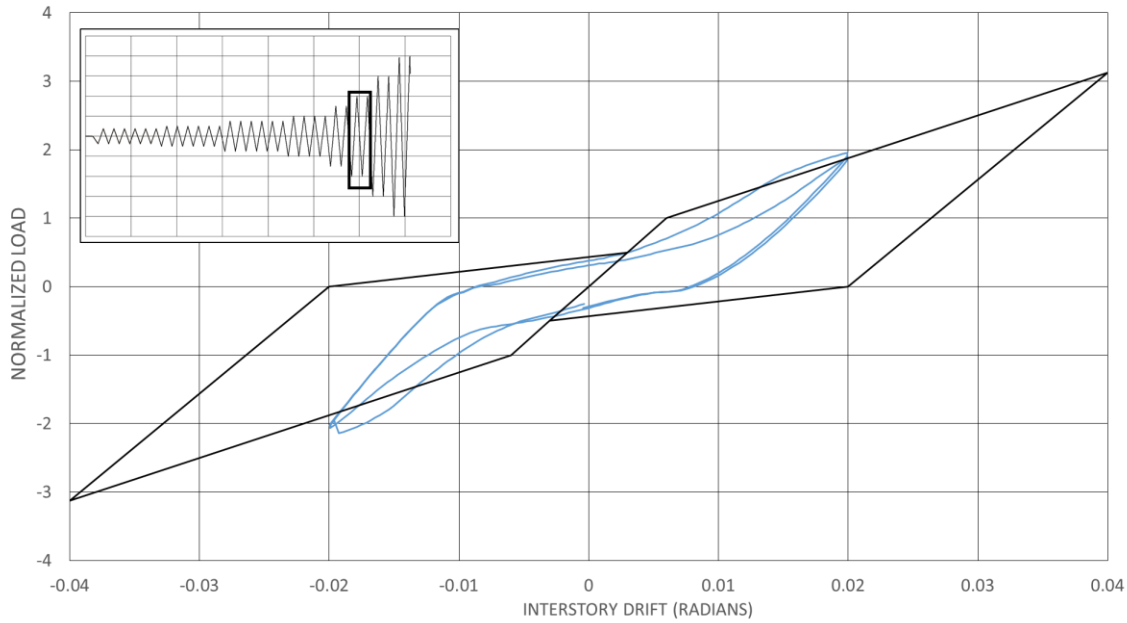

FIGURE 6.8: LOAD CYCLE 6 - HYSTERETIC BEHAVIOR

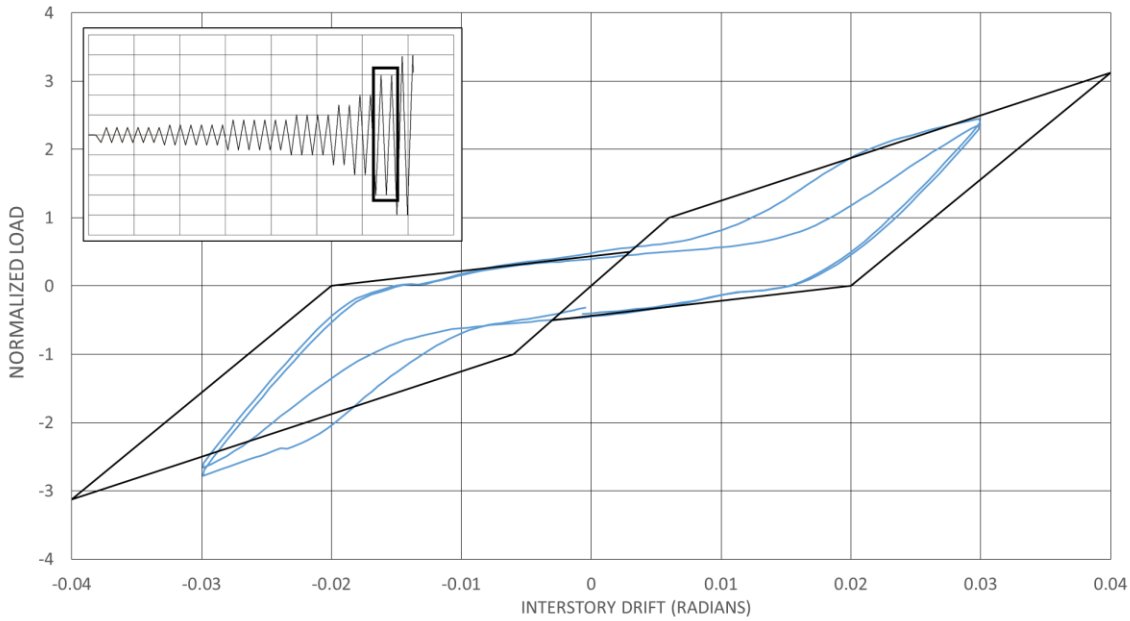

FIGURE 6.9: LOAD CYCLE 7 - HYSTERETIC BEHAVIOR

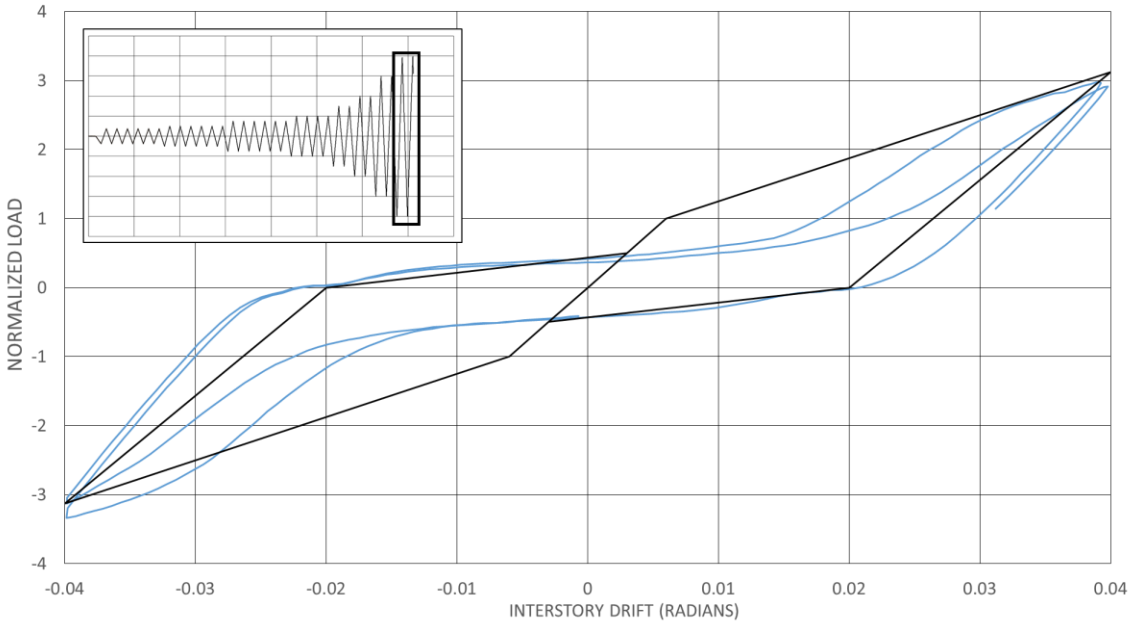

FIGURE 6.10: LOAD CYCLE 8 - HYSTERETIC BEHAVIOR

CHAPTER 7 - SUMMARY AND CONCLUSIONS

7.1 Summary

The mezzanine structure tested for this thesis utilizes moment-resisting connections to provide resistance to seismic forces. The behavior of this structure was characterized using the loading protocol from the AISC Seismic Design Manual (AISC 2010) for the prequalification of moment-resisting connections. This was accomplished through the presentation of experimental data, development of moment-rotation curves of the base connections, and using measured data to development of a hysteretic model typical of the structure's behavior when subject to lateral deformation demand.

7.2 Summary of Material Testing

The material testing performed for this thesis involved testing cold-formed and hot-rolled structural elements. The specified materials included: ASTM A572 Grade E (50 ksi, yield strength) for cold-form channels and connecting plates, ASTM A500 Grade B (46 ksi, yield strength) for HSS columns, and ASTM A36 Steel (36 ksi, yield strength) for base plates.

All the tested materials far exceeded the minimum yield strength specified by ASTM with the most materials not exhibiting the classic behavior associated with it. The cold-working process is responsible for most of the changes to the stress-strain properties of the material causing different yield and ductility characteristics along with the absence of upper and lower yield points.

1.) The HSS is specified as ASTM A500 Grade B steel with a specified yield strength of 46 ksi but contained an average tested yield strength of 80.1 ksi. No upper and lower yield points were observed in the stress-strain data.
2.) The long span channel is specified as ASTM A572 Grade E steel with a specified yield strength of 50 ksi, which is a typical high strength low-allow steel. The average tested yield strength of 66.1 ksi. Upper and lower yield points were not observed in the stress-strain data.
3.) The short span channel is specified as ASTM A572 Grade E steel with a specified yield strength of 50 ksi which is a typical high strength low-allow steel. The average tested yield strength of 87.4 ksi. Typical upper and lower yield points were observed in the stress-strain data.
4.) The connecting plate is specified as ASTM A572 Grade E steel with a specified yield strength of 50 ksi, which is a typical high strength low-allow steel. The average tested yield strength of 76.0 ksi. Typical upper and lower yield points were not observed, a slight yield plateau was observed.
5.) The base plate is specified as ASTM A36 steel which usually contains well defined yield plateau during material testing. The material contained an average tested yield strength of 87.7 ksi. No upper and lower yield points were observed which is rare in ASTM A36 material tests.

Exceeding the material strength to meet a standard is commonplace. However, as seen in this structural test the excessive material strengths of the connecting plate and the HSS exceeded the typical ultimate strength of the welding material (E70 electrodes were used). This could make the weld susceptible to premature fracture.

7.3 Summary of HSS Base Plate Moment-Rotation Curves

A variety of moment-rotation hysteresis were constructed for this thesis to evaluate the behavior of the base connections. The moment-rotation behavior of the base plates in the mezzanine structure tested give hysteretic behavior similar to that seen in previous research (Kanvinde, Grilli and Zareian 2012). A comparison of Figure 5.3, Figure 5.10, and Figure 7.1 all illustrate pinched hysteretic behavior. The moment-rotation hysteresis from this thesis involves wedge type expansion anchors and thus more sliding and pinching of the hysteresis is present. The work of (Kanvinde, Grilli and Zareian 2012) includes a base plate with cast-in anchor rods and wide flange column shapes. Wedge-expansion anchors are much easier to pull out, leading to different behavior. Additionally, the moment-rotation response from this thesis utilizes longer and thinner base plates leading to much different behavior.

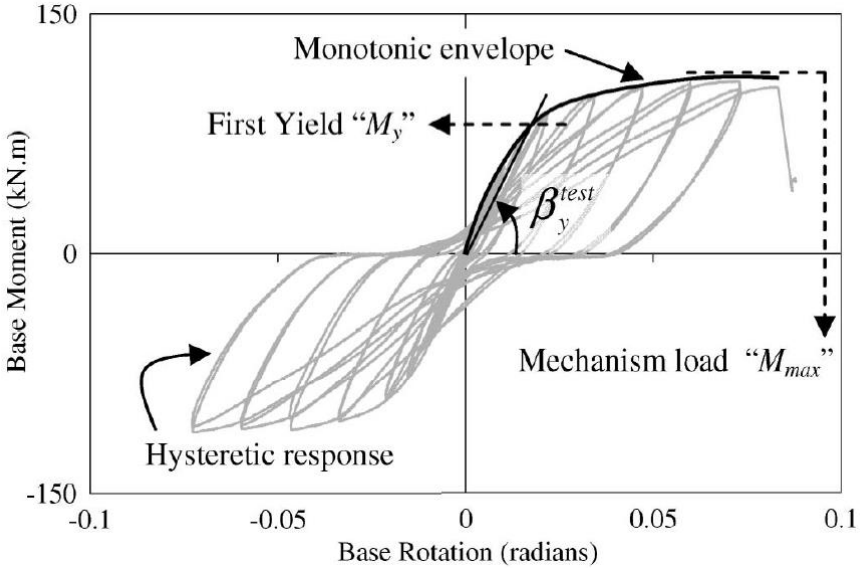

FIGURE 7.1: HYSTERETIC BEHAVIOR OF (KANVINDE, GRILLI AND ZAREIAN 2012)

7.4 Summary of Mezzanine Hysteretic Behavior

The hysteretic model for the mezzanine structure captures the overall behavior of the mezzanine structure. The load-interstory drift of (Uang, et al. 2010) displayed in Figure 7.2 gives a similar shape to the load-interstory drift for the mezzanine structure (reference Figure 6.10). The envelope curve developed from Figure 7.2 is given in Figure 7.3. The hysteretic behavior of the mezzanine tested in this thesis exhibits significantly greater pinching in the hysteretic response. However, the overall behavior is comparable to that seen in previous testing. Figure 7.2 shows an initial stiffness observed in both followed by a secondary stiffness and an unloading behavior. Unlike the model created for this thesis Uang (Figure 7.3) classified the initial stiffness as free sliding and used a monotonic response to characterize the secondary stiffness. A monotonic response was not available for this test. If additional experimental data was available, the results of this thesis could be modelled using hysteretic model shown in Figure 7.3. Unloading is then said to be rigid rather than equivalent to an initial stiffness.

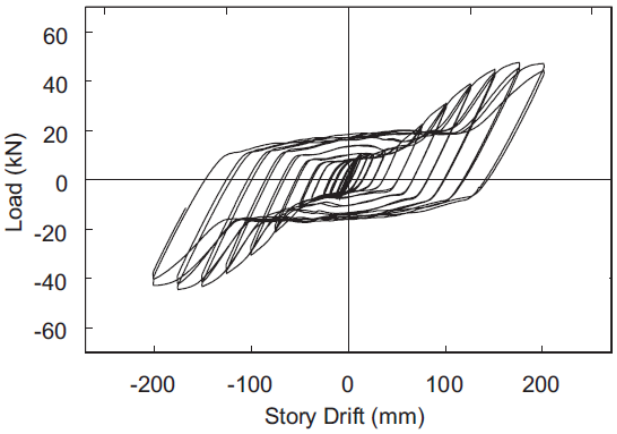

FIGURE 7.2: LOAD VS. STORY DRIFT (C.-M. UANG, A. SATO AND J.-K. HONG, ET AL. 2010)

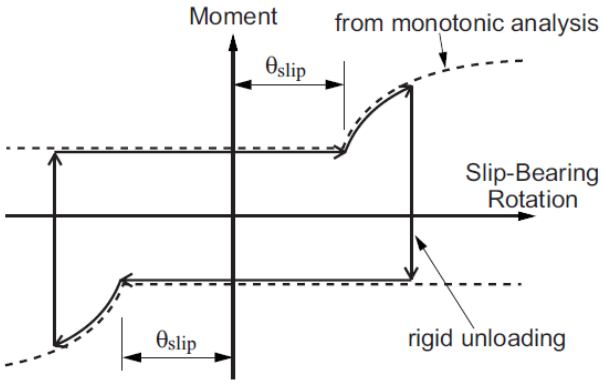

FIGURE 7.3: PROPOSED HYSTERETIC MODEL (UANG, ET AL. 2010)

7.5 Conclusions and Recommendations for Future Research

This thesis makes several contributions and suggests possible areas for new research.

1.) The different levels of interstory structural drift and slip measured in the base plates of the mezzanine structure point to a need for new research to develop better design practices for HSS column base connections with wedge expansion anchors subjected to bending forces.

2.) The results confirm that eccentrically load bolt groups have the ability to develop moment capacity in the cross-section of the connected members without restraint of member flanges.

3.) Wedge expansion anchors can facilitate dissipation the energy associated with cyclic loading but can result in large amounts of slip and anchor pull-out.

4.) The lack of yield point control in ASTM A500 Grade B Steel suggests that ASTM A1085 steel should be considered for HSS shapes used for mezzanines subject to seismic loads.

5.) Changing the column length of the structure to reflect actual mezzanine heights could transfer bending forces away from the column base connections and into the channel beams.

6.) Perform component tests of the base plate moment-resisting connection using the protocols from the AISC Seismic Specification to confirm the results seen in this thesis.

7.) Perform component tests of the beam-to-column moment-resisting connections using protocols from the AISC Seismic Specification to develop full moment-rotation behavior of the connection to better understand energy dissipation characteristics.

8.) Use the hysteretic model developed to determine a mezzanine moment capacity and rotational capacity response to ground motions using inelastic time history.

9.) Develop finite element models of the beam to column connection and test using AISC Seismic Specification loading protocols to determine the behavior in its entirety with correlation to physical tests.

10.) Develop finite element models of the base connection and test using AISC Seismic Specification loading protocols to determine the behavior in its entirety.

11.) Apply the FEMA P695 methodology to evaluate seismic design assumptions. The hysteretic models developed in this thesis can be used as the basis of this evaluation (FEMA 2009). Similar work was performed using the experimental results of (Uang, et al. 2010) to create collapse margin data in (Uang and Sato 2013).

BIBLIOGRAPHY

ACI 214. 2011. *Recommended Practice for Evaluation of Strength Test Results of Concrete.* Farmington Hills, MI: American Concrete Institute, www.concrete.org.

AISC. 2010. *Seismic Design Manual.* Chicago.

AISI. 2007. *Standard for Seismic Design of Cold-Formed Steel Structural Systems-Special Bolted Moment Frames, AISI S110-07.* Washington, D.C.: AISI.

ASTM. 2015. *ASTM A1085/A1085M-15, Standard Specification for Cold-formed Welded Carbon Steel Hollow Structural Sections (HSS).* Conchokocken, PA: ASTM Internation, www.astm.org.

ASTM. 2014. *ASTM A370-14, Standard Test Method and Definitions for Mechanical Testing of Steel Products.* West Conchokocken, PA: ASTM Internation, www.astm.org.

ASTM. 2013. *ASTM A500/A500M-13, Standard Specification for Cold-formed Welded and Seamless Carbon Steel Structural Tubing in Rounds and Shapes.* Conchokocken, PA: ASTM Internation, www.astm.org.

ASTM. 2015. *ASTM A572/A572M-15, Standard Specification for High-Strength Low-Alloy Columbium-Vanadium Structural Steel.* Conchokocken, PA: ASTM Internation, www.astm.org.

ASTM. 2015. *ASTM C39/C39M-15a, Standard Test Method for Compressive Strength of Cylindrical Concrete Specimens.* West Conshohocken, PA: ASTM Internaional, www.astm.org.

ASTM. 2015. *ASTM E488/E488-15 Standard Test Methods for Strength of Anchors in Concrete Elements.* Conshohocken, PA: ASTM Internation, www.astm.org.

Beshara, B, and R Schuster. 2000. "Web Crippling Data and Calibration of Cold Formed Steel Members." *Committee on Specifications for the Design of Cold-Formed Steel Structural Members, American Iron and Steel Institute.*

Chung, K.F., and L Lau. 1998. "Experimental Investigation of Bolted Moment Connections Among Cold-Formed Steel Members." *Engineering Structures 21, Elsevier* 898-911.

Cooke, R.J., S.J. Jordan, and A.M. Kanvinde. 2013. "Exposed Column Base Plate Connections in Moment Frames - Simulations and Behavioral Insights." *Journal of Constructional Steel Research 84* 82-93.

CSA. 2008. *N287.2-08 (R2013) - Material Requirements for Concrete Contained Structures for CANDU Nuclear Power Plants.* CSA.

Fadden, Matthew. 2013. *Cyclic Bending Behavior of Hollow Structural Sections and their Application in Seismic Moment Frame Systems.* Ann Arbor: Doctoral Dissertation, University of Michigan.

Fadden, Matthew, and Jason McCormick. 2012. "Cyclic Quasi-Static Testing of Hollow Structural Section Beam Members." *Journal of Structural Engineering* 561-570.

Fadden, Matthew, and Jason McCormick. 2013. "Finite Element Model of the Cyclic Bending Behavior of Hollow Structural Sections." *Journal of Constructional Steel Research* 64-75.

FEMA. 2009. "FEMA P695 Quantification of Building Seismic Performance Factors."

Fisher, J.M., and L.A. Kloiber. 2006. *AISC Steel Design Guide #1 - Base Plate and Anchor Rod Design.* Chicago, IL: American Institute of Steel Construction.

Ghobarah, A, and T.S. Aziz. 2004. "Seismic Qualification of Expansion Anchors to Canadian Nuclear Standards." *Nuclear Engineering and Design* 337-392.

Guerrero, Nestor, Maria Eugenia Marante, Ricardo Picon, and Julio Florez-Lopez. 2007. "Model of Local Buckling in Steel Hollow Structural Elements Subject to Biaxial Bending." *Journal of Constructional Steel Research 63* 779-790.

Kanvinde, A.M., D.A. Grilli, and F. Zareian. 2012. "Rotation Stiffness of Exposed Column Base Connections: Experiments and Analytical Models." *Journal of Structural Engineering* 549-560.

Medina, Ricardo A., and Helmut Krawinkler. 2004. "Influence of Hyteretic Behavior on the Nonlinear Response of Frame Structures." *13th World Conference on Earthquake Engineering.* Vancouver, B.C., Canada. 239.

Murray, Thomas, and Ronald Meng. 1995. "Seismic Loading of Moment-End Plate Connections: Some Preliminary Results." *Proceedings of the Third International Workshop.* Trento, Italy: Connections in Steel Structures III. 361-370.

Oh, Young-Hun, Sang Whan Han, and Li-Hyung Lee. 2000. "Effect of Hysteretic Models on the Inelastic Design Spectra." *12th World Conference on Earthquake Engineering.* Auckland. 30.

PEER, and NSF. n.d. *OpenSees.* http://opensees.berkeley.edu/.

2016. "Power-Stud Wedge Expansion Anchor." *Power Stud Product Information.* Brewster, NY: Power Fasteners, Inc.

Rasmussen, K, and B Gilbert. 2010. "Bolted Moment Connections in Drive-In and Drive-Through Steel Storage Racks." *Journal of Constructional Steel Research 66, Elsevier* 755-766.

Štrba, M., and M. Karmazínová. 2012. "Actual Behaviour of Objective Load-Carrying Capacity of Tension Steel Expansion Anchors in Concrete." *Procedia Engineering 40* 440-444.

Tremblay, R., M.H. Archambault, and A. Filiatrault. 2002. "Seismic Response of Concrentically Braced Steel Frames Made with Rectangular Hollow Bracing Membersq." *Journal of Structural Engineering 129* 1626-1636.

Uang, Atsushi Sato, Jong-Kook Hong, and Ken Wood. 2010. "Cyclic Testing and Modeling of Cold-Formed Steel Special Bolted Moment Frame Connections." *Journal of Structural Engineering, ASCE* 953-960.

Uang, Chai-Ming, and Atsushi Sato. 2008. "Establishment of Capacity Design Requirements for Cold-Formed Steel-Special Bolted Moment Frames." Edited by ASCE. *Structures Congress.*

Uang, Chai-Ming, and Atsushi Sato. 2009. "Seismic Design Procedure Development for Cold-Formed Steel-Special Bolted Moment Frames." *Journal of Constructional Steel Research 65, Elsevier* 860-868.

Uang, Chai-Ming, and Atsushi Sato. 2010. "Seismic Performance Factors for Cold-Formed Steel Special Bolted Moment Frames." *Journal of Structural Engineering, ASCE* 961-967.

Uang, Chai-Ming, Atsushi Sato, Jong-Kook Hong, and Ken Wood. 2010. "Cyclic Testing and Modeling of Cold-Formed Steel Special Bolted Moment Frame Connections." *Journal of Structural Engineering, ASCE* 953-960.

Uang, Chia-Ming, and Atsushi Sato. 2013. "A FEMA P695 Study for the Proposed Seismic Performance Factors for Cold-Formed Steel Special Bolted Moment Frames." *Earthquake Spectra* 259-282.

Vandegans, D., and J.P. Jaspart. 1998. "Application of Component Method to Column Bases." *Journal of Constructional Steel Research 48* 89-106.

Van-Long, Hoang, Jaspart Jean-Pierre, and Demonceau Jean-François. 2013. "Behavior of Bolted Flange Joints in Tubular Structures Under Monotonic Repeated and Fatigue Loadings I: Experimental Tests." *Journal of Constructional Steel Research 85* 1-11.

Wald, František, Jean-Pierre Jaspart, and Zdeněk Sokol. 2008. "Base Plate in Bending and Anchor Bolts in Tension." *HERON* Vol. 53, No. 1/2.

Wheeler, A.T., M.J. Clarke, and G.J. Hancock. 2000. "F.E. Modeling of Four-Bolt, Tubular Moment End-Plate Connections." *Journal of Structural Engineering* 816-821.

Wilkinson, Tom, and Gregory Hancock. 1998. "Tests to Examine Compact Web Slenderness of Cold-Formed RHS." *Journal of Structural Engineering 124* 116-1174.